The Development of an Active Area Neutron Dosemeter

by

James Brushwood

Submitted for the degree of Doctor of Philosophy

Department of Physics
School of Electronics and Physical Sciences
University of Surrey

September 2003

Disclaimer

Any views expressed are those of the author and do not necessarily represent those of Flagship Training Ltd, the Nuclear Department or those of HM Government.

Abstract

This thesis presents the research leading towards the development of an Active Area Neutron Dosemeter (AAND). A review of a number of current dosemeter designs is presented and examination of their responses in a selection of representative workplace neutron fields has been undertaken. In the light of this a new design was proposed, the AAND, which by the use of embedded thermal neutron detectors would allow more accurate determinations of ambient dose equivalent to be made. The design was to be optimised for use in 'soft' neutron spectra arising from the operation of a well-shielded pressurised water reactor.

Both experimental and computational work has been undertaken. Extensive use was made throughout this work of Monte Carlo calculations. Experimental work addressed the selection of suitable thermal neutron detectors. The phenomenon of soft errors in dynamic random access memories was initially extensively studied. However, advances in device architecture were found to render this impractical. Instead detection with lithium fluoride coated photodiodes was studied. This proved successful.

The response functions of the various detectors in the AAND were determined computationally. An experimental verification using both mono-energetic and isotopic neutron sources was conducted. Good agreement was observed between the predicted and measured responses.

Final demonstration of the AAND was conducted and indicated that that the ambient dose equivalent could be accurately determined. Furthermore, the novel ability to determine spectral characteristics, in this case the radiation-weighting factor, was demonstrated.

Suggested further developments of the AAND have been identified. Most significantly the potential to determine the angular distribution of the neutron field is proposed.

Contents

Acknowledgements

The author would like to thank his two supervisors Professor P.A. BEELEY (HMS SULTAN) and Professor N.M. SPYROU (University of Surrey) for all of their patience and advice throughout the long years. Additionally, the author wishes to acknowledge Dr. D. THOMAS (National Physical Laboratory) for his interest and advice during the experimental measurements at the NPL low scatter facility.

I am also indebted to the Nuclear Department, HMS SULTAN and FLAGSHIP TRAINING LIMITED for supporting and financing this research work, without their support I would have been unable to pursue my studies.

On a personal note I would like to dedicate this thesis to my parents MARION and JOHN who made all of this possible. Finally, I would like to express my deepest gratitude to my long-suffering partner KATE LEGON for providing me with ceaseless support, encouragement and love throughout the course of my studies.

Preface

Introduction

For a number of years area neutron dosimetry in support of the UK's Naval Nuclear Propulsion Programme has largely been conducted using a Leake type spherical dosemeter, known as the Mk7 NRM (see Section 2.4.1.1). A review of this instrument and a selection of other designs is provided in Chapter 2. The ambient dose equivalent response of the Mk7 NRM, in common with virtually all other designs is known to be dependent upon the incident energy spectrum. Not only does the energy response vary with but it also deviates significantly from the ideal as defined by the International Commission on Radiological Protection (ICRP) in their publication ICRP74, see Section 2.2.2, fluence to ambient dose equivalent $h^*(10)$ conversion coefficients.

In essence although a dosemeter may have been calibrated to indicate the true dose equivalent in some calibration neutron field, it will not necessarily indicate correctly in operational spectra. The Leake design achieved a reasonable fit to the conversion coefficients as defined at that time, however, the instrument does have an over-response to neutrons in the keV region. This deficiency and its consequences are fully discussed in Chapter 3.

The Active Area Neutron Dosemeter

This thesis describes the design and the experimental programme in the development of a new Active Area Neutron Dosemeter (AAND) with correction for the energy dependence of the incident neutron field. To achieve good sensitivity a central boron trifluoride (BF_3) neutron detector is used; its energy response has been shaped using a combination of concentric polyethylene moderators and a cadmium filter. To determine the energy dependence thermal neutron detectors are located within the moderator, their energy response being controlled by their depth within the moderator.

Initial work focused on the use of Dynamic Random Access (drams) memories as a suitable small thermal neutron detector for incorporation into the moderator and this study is fully described in Chapter 4. Regrettably, after considerable study it was concluded that these devices were not a practical option. Therefore, a photodiode

coated with a suitable charge particle converter was investigated instead. This study proved successful and is described in Chapter 5.

Having selected photodiodes as the thermal neutron detector. The development and testing of the proposed AAND design was investigated, this work is reported in Chapter 6. Finally, in Chapter 7 an overall statement of findings and suggestions for further work is provided.

Chapter 1 Radiation Physics

1.1 Sources of Neutrons and Alpha Particles

1.1.1 Neutron Sources

There is no convenient radioactive decay process that leads to a practical "laboratory" source of neutrons unlike gamma radiation where subsequent to β^- decay many isotopes de-excite by the emission of gamma photons. A number of highly excited states de-excite by the emission of a neutron but they are all short lived. The longest-lived, with a half-life of approximately 56 seconds results from the β^- decay of the fission product ^{87}Br, which produces an excited state of ^{87}Kr that de-excites by neutron emission.

The best known of all neutron sources are nuclear reactors. Some isotopes of uranium and plutonium have a high absorption cross-section for a nuclear reaction, fission, which causes the compound nucleus to split into two fragments and emit two or more high-energy neutrons. By appropriate arrangement of fissile, moderating and absorbing materials a self-sustaining fission chain reaction can occur, in essence as many neutrons are created by fission as either escape or are parasitically absorbed. On average each fission event releases around 200 MeV of energy, the majority of which is accounted for by the kinetic energy of the fission fragments (≈160 MeV) whereas the neutrons carry about 5 MeV.

The neutron energy spectrum that results from the thermal neutron induced fission of ^{235}U fission is frequently described by the Watt formulation, Equation 1.1, with the constants a=0.988 MeV and b=2.249 MeV^{-1} [1.1].

$$n(E) = e^{-\left(E/a\right)} \sinh\sqrt{bE} \qquad \textit{Equation 1.1}$$

where, n(E) – fraction of neutrons with energy E

a, b – constants dependent on fissioning system

More convenient laboratory neutron sources do exist; these can be divided into radionuclide and accelerator produced.

The most common radionuclide neutron sources are based on the (α,n) reaction. These sources take advantage of the (α,n) reaction in light elements such as beryllium and boron. The sources are usually fabricated from a doubly encapsulated mixture of

an alpha emitting actinide, such as americium or radium mixed with beryllium. It is a characteristic of these sources that substantial alpha activity is required even for modest neutron yields. For instance a 37 GBq ^{241}Am/Be neutron source produced by Amersham International had an initial neutron emission rate of 1.62×10^6 s^{-1} [1.2], or approximately 44 neutrons per 1×10^6 alpha particles emitted.

The energy spectrum produced by these sources depends on both the alpha particle energy and the target. For example ^{241}Am/Be produces a hard or high-energy spectrum with a mean energy of around 4.2 MeV but extending to 8-9 MeV. The neutron energy spectrum of such a source is shown in Figure 3.7.

To avoid the radiological safety considerations of such large quantities of actinides, the use of spontaneous fission sources grew. The radionuclide ^{252}Cf decays both by alpha emission and spontaneous fission. The effective half-life of 2.65 years is dominated by the alpha decay mode. A 1 μg ^{252}Cf source emits approximately 2.0×10^6 neutrons s^{-1} [1.5]. Again the energy spectrum, shown in Figure 3.7, may be represented by a Watt formulation but with a = 1.025 MeV and b = 2.249 Mev^{-1} [1.1]. The mean energy in this case is around 2.1 MeV

A rarer, and uniquely amongst the radionuclide sources mono-energetic, source of neutrons is one based on the (γ,n) reaction. Both beryllium and deuterium will absorb an energetic photon (typically > 2MeV) to supply the separation energy and consequently emit a free neutron. The major disadvantage, often to the point of impracticability, are the very large specific activities of high-energy gamma emitting isotopes that are required even for very modest neutron outputs. Furthermore, suitable high-energy gamma-ray emitting isotopes are often quite short lived (tens of days to hours e.g. $t_{½}$ ^{124}Sb = 60.2 days). For instance the potentially useful mono-energetic 23 keV neutron source produced by ^{124}Sb/Be emits only 2×10^4 n s^{-1} for 1 GBq of ^{124}Sb.

In practice the only means to generate mono-energetic neutrons is by using accelerator driven systems. There exist two distinct types of accelerator driven systems, sealed tube and laboratory accelerator. By far the most versatile system is the laboratory accelerator. In such systems the particles required to initiate the neutron producing nuclear reactions (i.e. protons, deuterons) are produced by an ion source. These ions are then accelerated electrostatically and using a velocity selector,

essentially a very well controlled magnetic field, only those ions with the required energy are extracted. Further beam conditioning and focusing is achieved using magnetic lenses. The conditioned beam is then incident upon a target; this is usually in the form of the required target element (natural or isotopically enriched) deposited in a thin layer on an inert backing.

The energy of the neutrons produced is dependent on the incident energy of the ions, therefore, to produce mono-energetic neutrons the target must be sufficiently thin so that the incident ions do not lose significant energy in the target layer. Subsequently, the ions are stopped in the inert backing; the material selected for the backing should itself not generate neutrons. Dependent on the beam current and energy increasingly complex target cooling arrangements are required. Facilities such as these are capable of producing a wide variety of neutron energies limited only by the availability of suitable targets and the maximum/minimum incident ion energies achievable. The mono-energetic neutron beam standards available at the National Physical Laboratory are generated in such a manner.

Less versatile but considerably more convenient are sealed tube systems. These operate in a similar fashion to the laboratory accelerator except that both the ion and target are fixed. Originally developed to replace radionuclide neutron sources in oil-well logging applications, sealed tube systems are now utilised in other neutron interrogation applications where an 'on/off' neutron source is required. Generally only deuteron/deuterium and deuteron/tritium as source/target combinations are used. Again the incident ions are produced in an ion source but the beam condition and focusing are considerably simpler than those in laboratory accelerators. The ion source itself is a sealed system in which the deuterium has been adsorbed into some metal. When electrically heated the gas is driven off and then ionised within the ion source. The targets all tend to be metals such as titanium that form stable hydrides with hydrogen (i.e. deuterium or tritium). These devices are very much more compact and inexpensive than laboratory accelerators but are only capable of producing a single neutron energy.

Perhaps the best-known reaction is the deuterium/tritium fusion reaction, see Equation 1.2. This reaction, provided that the target is sufficiently thin that negligible energy loss occurs in the target itself, produces monoenergetic neutrons with an energy of between 13 and 20 MeV dependent on the incident deuteron energy. There is a large

peak in the tritium cross-section in the region of 110 keV incident deuteron energy and this generates neutrons with an energy of 14.8 MeV. This energy is one of the recommended energies for the evaluation of neutron dosemeters as defined by the International Standards Organisation in ISO 8529 [1.3].

$$ {}^{3}_{1}H \; + \; {}^{2}_{1}H \rightarrow {}^{4}_{2}He \; + \; {}^{1}_{0}n \qquad \textit{Equation 1.2} $$

Similarly, mono-energetic neutrons between 2.5 and 6.0 MeV can be produced by using the deuterium/deuterium fusion reaction, see Equation 1.3. Two particularly important energies in the ISO 8529 recommended set are 2.5 and 5.0 MeV, both of which are feasible using the deuterium/deuterium reaction with deuteron energies of 100 keV and 1.77 MeV respectively.

$$ {}^{2}_{1}H + {}^{2}_{1}H \rightarrow {}^{3}_{2}He + {}^{1}_{0}n \qquad \textit{Equation 1.3} $$

Of the other recommended ISO 8529 energies generally either the ^{3}H(p,n) or ^{7}Li(p,n) reaction with a appropriate energy bombarding proton are used, (Table 1.1 and Equations 1.4 and 1.5)

$$ {}^{3}_{1}H + {}^{1}_{1}p \rightarrow {}^{3}_{2}He + {}^{1}_{0}n \qquad \textit{Equation 1.4} $$

$$ {}^{7}_{3}Li + {}^{1}_{1}p \rightarrow {}^{7}_{4}Be + {}^{1}_{0}n \qquad \textit{Equation 1.5} $$

Table 1.1 ISO 8529 recommended accelerator produced energies

ISO 8529 Energy (MeV)	Possible mechanisms	Preferred route at National Physical Laboratory [1.4]
0.144	^{7}Li(p,n) or ^{3}H(p,n)	^{7}Li(p,n)
0.250	^{7}Li(p,n) or ^{3}H(p,n)	^{7}Li(p,n)
0.565	^{7}Li(p,n) or ^{3}H(p,n)	^{7}Li(p,n)
1.2	^{3}H(p,n)	^{3}H(p,n)
2.5	^{3}H(p,n) or ^{2}H(d,n)	^{3}H(p,n)
5.0	^{2}H (d,n)	^{2}H(d,n)
14.8	^{3}H(d,n)	^{3}H(d,n)

1.1.2 Alpha sources

The choice of alpha sources is very wide, at least twenty different alpha emitting isotopes are commercially available. Generally, alpha emitting radionuclides tend to belong to the actinide group of elements. They have a wide variety of half-life varying from microseconds to 10^{10} years. They essentially emit mono-energetic alpha particles provided the source is sufficiently thin that self-absorption is negligible. Typical alpha particle energies are between 4 and 6 MeV. Half-life is strongly correlated with energy, the more energetic emitters tend to have the shortest half-lives. A number of common alpha sources along with their energies and half lives [1.5] are shown in Table 1.2.

Table 1.2 Common alpha sources and energies of major emissions

Isotope	Half-life (years)	Alpha particle energy (MeV)	Percent Branching
^{148}Gd	74.47	3.182	100
^{239}Pu	2.4×10^4	5.156	73.3
^{241}Am	432.71	5.486	85.2
^{244}Cm	18.10	5.805	77.0
^{235}U	7.03×10^8	4.396	58.0

1.2 Interactions of Radiation

It is a distinguishing characteristic of alpha, beta, gamma and neutron radiation that they all cause ionisation either directly or indirectly. The two charged particle radiations interact predominantly electrostatically with the orbital electrons in the absorbing medium. Gamma photons have three interaction mechanisms, the photoelectric effect, Compton scattering and pair production. When photons interact photoelectrically their entire energy is predominately transferred to a K shell orbital electron, which is then ejected from the atom. In Compton scattering a portion of the photon energy is transferred to the electron whilst the photon is scattered through an angle and retains a reduced residual energy. In the region close to the field of the nucleus a photon may spontaneously convert into an electron/positron pair provided its energy exceeds 1022 keV i.e. twice the rest mass energy of an electron.

Subsequent to all of these interactions the resultant electrons will interact electrostatically.

In the case of the uncharged neutron, ionisation is not caused directly. Instead a number of nuclear reactions serve to transfer the neutron energy to the medium. The three most important of which are elastic scattering, inelastic scattering and absorption. Considering first elastic scattering in which a neutron interacts with the target nuclei and is scattered with a reduced energy. The target nuclei recoils with a kinetic energy equivalent to the total amount transferred from the neutron. By considering these collisions as being between hard spheres and applying the principles of conservation of momentum and energy it is possible to show that the maximum possible transfer of energy is dependent on the target nucleus mass (A). Equation 1.6 gives the maximum possible fractional transfer.

$$\frac{E_{recoil}}{E_{neutron}} = \frac{4A}{(1+A)^2} \qquad \textit{Equation 1.6}$$

It is apparent that for a particle with atomic mass A=1 the entire incident neutron energy may be transferred in a single interaction and in this particular case the recoil will be a proton. The recoiling protons will then interact electrostically with the medium and so the neutron will indirectly cause ionisation.

Essentially the mechanism of inelastic scattering is similar to that of elastic except that not all of the energy transferred from the neutron appears as kinetic energy of the recoil. Instead some portion excites the nucleus itself, which then de-excites by the emission of gamma photons. Again the net result is ionisation.

When a neutron is absorbed many different nuclear reactions can occur, these reactions may be conveniently divided into two categories prompt disintegration i.e. (n,p), (n,α), (n,2n) and radiative capture. These reactions are shown below in Equations 1.7a-d.

Prompt disintegration

$${}^{A}_{Z}X \; + \; {}^{1}_{0}n \rightarrow {}^{A}_{Z-1}Y \; + \; {}^{1}_{1}p \;\; (n,p) \qquad \textit{Equation 1.7a}$$

$${}^{A}_{Z}X \; + \; {}^{1}_{0}n \rightarrow {}^{A-3}_{Z-2}U \; + {}^{4}_{2}He \;\; (n,\alpha) \qquad \textit{Equation 1.7b}$$

$${}^{A}_{Z}X + {}^{1}_{0}n \rightarrow {}^{A-1}_{Z}X + 2\,{}^{1}_{0}n \quad (n,2n) \qquad \textit{Equation 1.7c}$$

Radiative capture

$$ {}^{A}_{Z}X + {}^{1}_{0}n \rightarrow {}^{A+1}_{Z}X + \gamma \quad (n,\gamma) \qquad \textit{Equation 1.7d} $$

An important consideration for all of these reactions is the Q-value. Equation 1.8 defines this. The coefficient of 931.494 is introduced to convert from atomic mass units as used for the terms m_r (mass of reactants) and m_p (mass of products) to energy in MeV.

$$ Q = 931.494(m_r - m_p) \qquad \textit{Equation 1.8} $$

If the Q-value of the reaction is positive the reaction is said to be exoergic (exothermic) and any energy neutron is capable of causing that particular reaction. However, if the Q-value is negative the reaction is endoergic (endothermic) and a neutron must have an energy exceeding some threshold value (E_{th}) to initiate that particular reaction. Equation 1.9 gives the threshold energy, where m_n is the mass of a neutron and m_t is the mass of the target nuclei.

$$ E_{th} = -Q\left(1 + \frac{m_n}{m_t}\right) \qquad \textit{Equation 1.9} $$

The (n,α) reactions with ^{6}Li and ^{10}B are of particular importance in this work and are examined in some detail below.

1.2.1 Kinematics of the ^{6}Li(n,α) and ^{10}B(n,α) reactions

The Q-values for both the ^{6}Li and ^{10}B (n,α) reactions, given in Equations 1.10a-d, have been calculated and are tabulated below in Table 1.3. Two possible reactions occur with ^{10}B, one of which leads to an excited state of ^{6}Li that decays by emission of a 0.48 MeV gamma photon. If thermal neutrons initiate this reaction approximately 94% of all reactions will lead to the excited state. Also shown in Table 1.3 are the energies of the reaction products, these have been calculated assuming that the incoming neutron has zero momentum. This will introduce a small error, however, the incoming neutron energy, typically less than 1 eV, is essentially negligible when compared to the reaction Q-values typically MeV. Mass data were taken from the 73rd CRC Handbook [1.6].

^{6}Li(n,α)^{3}H $\quad {}^{6}_{3}Li + {}^{1}_{0}n \rightarrow {}^{3}_{1}H + {}^{4}_{2}He$ *Equation 1.10a*

$^{10}\mathrm{B(n,\alpha)^7Li}$ $^{10}_{5}B + {}^{1}_{0}n \rightarrow {}^{7}_{3}Li + {}^{4}_{2}He$ *Equation 1.10b*

$^{10}\mathrm{B(n,\alpha)^7Li^*}$ $^{10}_{5}B + {}^{1}_{0}n \rightarrow {}^{7}_{3}Li^* + {}^{4}_{2}He$ *Equation 1.10c*

$^{7}_{3}Li^* \rightarrow {}^{7}_{3}Li + \gamma\,(0.48\mathrm{MeV})$ *Equation 1.10d*

Table 1.3 Energetics of the $^{6}Li(n,\alpha)$ and $^{10}B(n,\alpha)$ reactions

Reaction	Q-value (MeV)	Product	Energy of product (MeV)	Alpha particle energy (MeV)
$^{6}\mathrm{Li(n,\alpha)^3H}$	4.783	$^{3}\mathrm{H}$	2.728	2.055
$^{10}\mathrm{B(n,\alpha)^7Li}$	2.790	$^{7}\mathrm{Li}$	1.013	1.777
$^{10}\mathrm{B(n,\alpha)^7Li^*}$	2.310	$^{7}\mathrm{Li^*}$	0.839	1.471

Provided the incoming neutron's energy is negligible compared to the Q-value the two reaction products will be emitted anti-parallel to each other and will have an isotropic angular distribution. As the neutron incoming energy increases the angular distribution will increasingly become forward peaked.

1.2.2 Cross-sections of the $^{6}Li(n,\alpha)$ and $^{10}B(n,\alpha)$ reactions

The probability that a neutron will undergo some nuclear reaction is conventionally expressed by the cross-section. The microscopic cross-section (σ) expresses this probability of a particular reaction per nucleus and has the dimensions of area, by convention the barn where 1 barn is equivalent to 1×10^{-28} m^2. The macroscopic cross-section (Σ) is the product of the number of nuclei (N) per unit volume and the microscopic cross-section. The macroscopic cross-section has dimensions of inverse length and can be considered as the probability of interaction per unit length, equivalent to the linear attenuation coefficient for photons.

The microscopic cross-sections of the $^{6}Li(n,\alpha)$ and $^{10}B(n,\alpha)$ reactions are shown in Figure1.1, cross-section data is from the ENDF/B-VI evaluation [1.10].

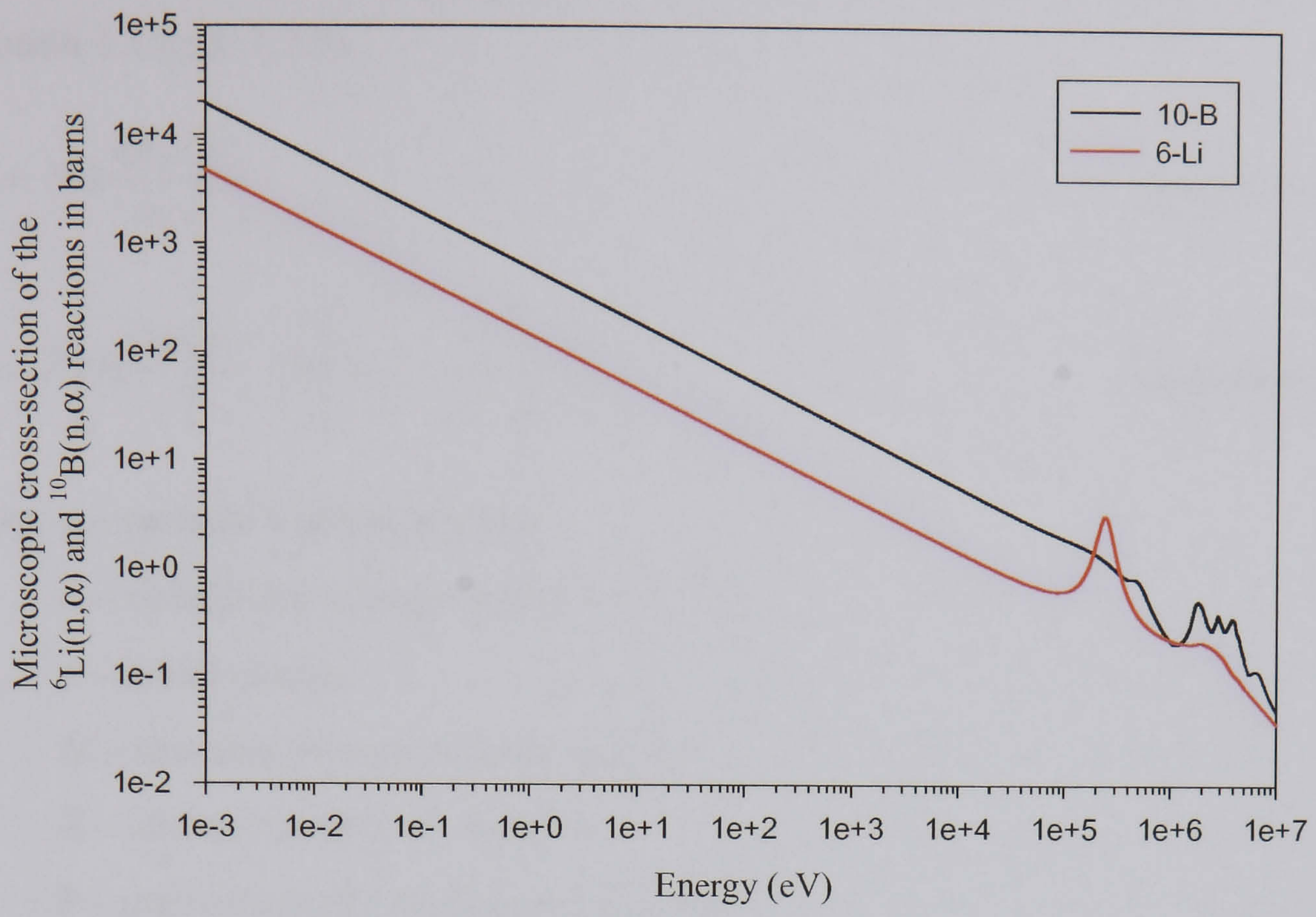

Figure 1.1 Cross-sections of ^{10}B and ^{6}Li

For thermal neutrons (E=0.0253 eV) boron-10 and lithium-6 have cross-sections of 3841 and 941 barns respectively. In both cases the cross-section falls with increasing neutron energy and is proportional to the reciprocal of neutron velocity, otherwise known as 1/v dependence.

1.2.3 Interactions of alpha particles.

The major interactions of alpha particles with matter are with the orbital electrons. Nuclear scattering or alpha particle induced reactions also occur i.e. (α,n) in beryllium, however, these are negligible compared to the electrostatic interactions. An alpha particle interacts with many orbital electrons resulting in the production of un-bound electrons and positive ions. Each of these interactions has little effect on the alpha particle's direction and it is only at the very end of its range that significant deflections do occur.

To describe these interactions an important parameter is L the Linear Energy Transfer (LET) which is defined in Equation 1.11.

$$L = \frac{dE}{dl}$$ *Equation 1.11*

where, dE is the energy loss traversing a distance dl

Classically the LET for a charged particle is described by the Bethe formula, stated in Equation 1.12a & 1.12b.

$$L = NB\frac{4\pi e^4 z^2}{m_0 v^2} \qquad \textit{Equation 1.12a}$$

$$B = Z\left[\ln\frac{2m_0v^2}{I} - \ln\left[1 - \frac{v^2}{c^2}\right] - \frac{v^2}{c^2}\right] \qquad \textit{Equation 1.12b}$$

where, v – particle's initial velocity

e – elementary charge (1.602×10^{-19} C)

z – initial charge

N – absorber atomic number density

Z – atomic number of absorber

I – experimentally determined constant

The parameter I is considered an experimentally determined factor. It can be interpreted as the 'average' of the excitations and ionisation energies. Generally, it may be concluded that LET is inversely proportional to the particle energy and proportional to its initial charge. Absorbers with higher Z will have the higher LET for all particles.

Alpha particle interactions are a statistical process and so an initially mono-energetic beam of alpha particles will not remain mono-energetic as it passes through some medium, it will acquire a distribution of energies known as energy straggling. An important consequence is that alpha particles do not have an exact range. It is not until close to the mean maximum range that attenuation of alpha particles occurs. The energy straggling inherent in the earlier interactions will lead to a distribution of maximum ranges, known as range straggling, which is typically a few percent of the mean range. Instead the range is defined as the thickness for which 50% of the incident particles are absorbed and should correctly be referred to as the mean range.

Data tables exist for LET [1.7, 1.8] for a variety of charged particle and absorber combinations. However, often there is no data available for the particular particle /absorber combination. In such instances a number of approximations are required.

These all assume that the stopping power per atom of some mixture is simply additive and given by the Bragg-Kleeman rule (Equation 1.13).

$$L_{compound} = N_c \sum_i W_i \frac{1}{N_i} L_i \qquad \textit{Equation 1.13}$$

where, N_c – atom density of compound

W_i – atom fraction of i^{th} component

N_i – atom density of i^{th} component

1.3. Monte Carlo Simulations

The development of Monte Carlo techniques as a means to investigate neutron transport began with their use to examine neutron diffusion in fissile materials as part of the atomic bomb development program [1.9]. Neutron interactions are usually described statistically (e.g. cross-sections) and therefore neutron transport can be considered as a stochastic process. This process is often described as a random walk in which neutrons move freely between random interactions.

In essence the Monte Carlo method simulates the statistical processes that govern the interactions. A particle is started from some source position and then its individual interactions are followed. At each interaction the possible outcomes are randomly sampled and then the resultant particle is transported again to its next interaction. The particle is followed until some terminating event such as absorption or escape from the system. The individual particle lives are referred to as histories. As the simulation proceeds large number of histories are accumulated. Eventually, it is possible to estimate the physical properties at some point if sufficient histories have been accumulated which adequately sample the range of interactions that could contribute. A simplified schematic is shown in Figure 1.2.

Perhaps the simplest example of a Monte Carlo technique is the estimation of the area of a circle if the numeric value of π is unknown. To achieve this inside a square with sides equal to D a circle of diameter D is circumscribed. Pins are then dropped vertically onto the square. The ratio of the total number of pins inside the square to the number only inside the circle will give the ratio of the areas of the square and circle. It is apparent that as the number of pins dropped, or histories calculated, increases the simulation will better estimate the real physical value.

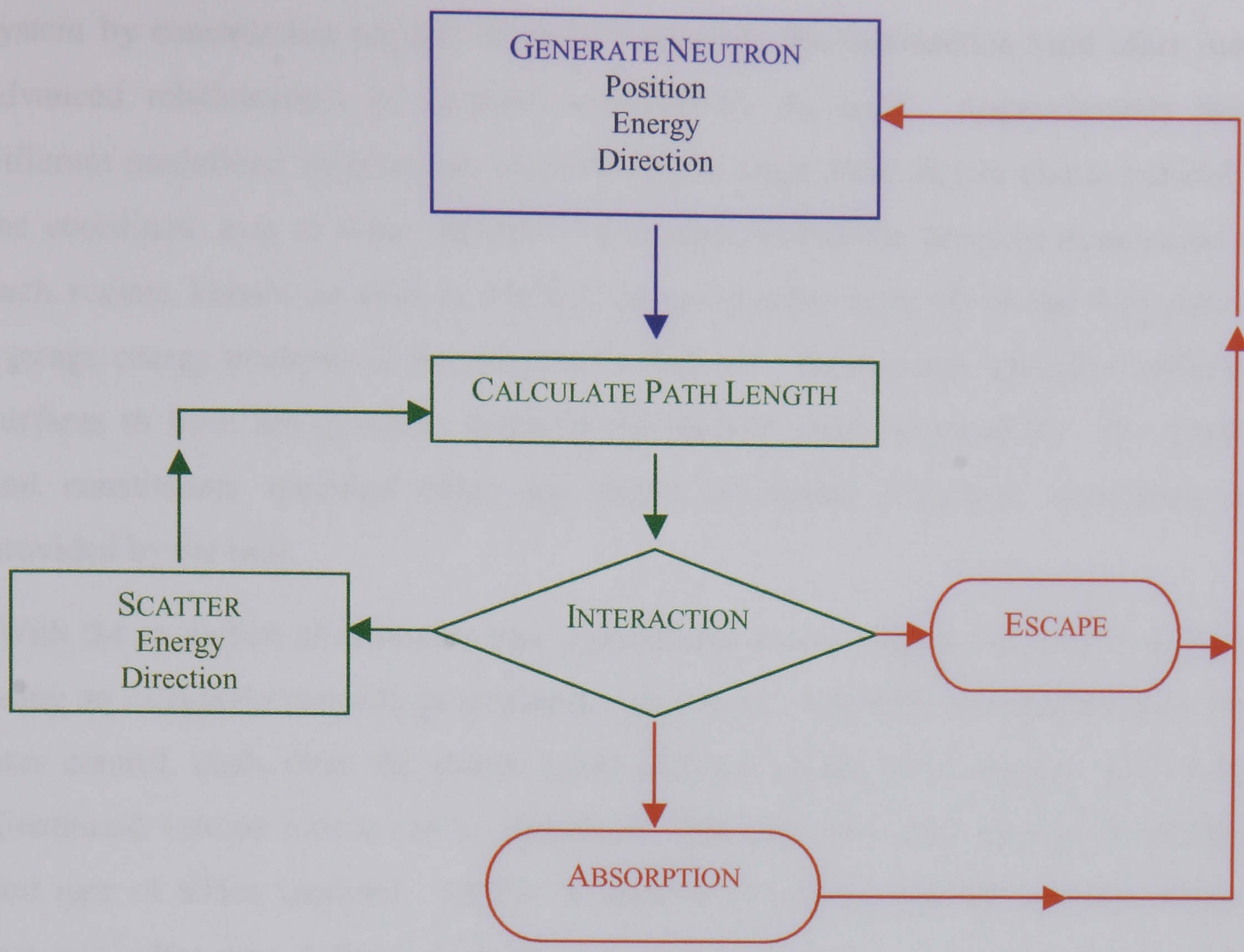

Figure 1.2 Schematic of Monte Carlo neutron transport

1.3.1 Neutron Transport Monte Carlo Codes

Perhaps the best-known Monte Carlo code for neutron transport is MCNP [1.1]. Throughout this work MCNP4b has been used and a brief description of its operation is given below. It is capable of transporting neutrons in the energy range 10^{-10} eV to typically 20 MeV (limited by availability of nuclear data), photons in the range 1 keV to 1GeV and a similar energy range for electrons.

One of the most important considerations in using Monte Carlo calculations is the availability of suitable cross-section data describing the interactions of the particles under study. Fortunately neutron cross-sections have been extensively investigated. As a result a number of widely available evaluated cross-section data files have been made available. At the time of writing the most recent evaluation available was the ENDF60 library this was prepared from the ENDF/B-VI evaluation. The library contained 124 nuclides and is extensively discussed in the Los Alamos National Laborarory (LANL) report LA-12891 [1.10].

To specify a system to be simulated under MCNP it is first necessary to specify the surfaces that bound and sub-divide the system. MCNP defines the geometry of the

system by constructing regions of space formed by the intersection (and other more advanced relationships) of surfaces specified by the user. Approximately thirty different predefined surfaces are available; these range from simple planes parallel to the coordinate axis to torus sections. It is advised that the physical dimensions of each region, known as cells in MCNP, be comparable with the mean free path of average energy neutrons in the material in that cell. Having now specified sufficient surfaces to form the geometry material information must be supplied. The density and constituents specified either by weight or atomic fractional abundance are provided by the user.

With the exception of criticality type calculations the user must also specify a source using an extremely versatile generalised source term. Virtually all variables are under user control, cases from the simple point isotropic source to an angular and energy distributed volume source can be described. The user must now specify the position and type of tallies required. MCNP is capable of tallying neutron currents, fluence rate and other user defined quantities i.e. energy deposition. Neutron fluence rates can be determined averaged across specified surfaces or within cells. Point like detectors to estimate fluence rate at a user specified point are also available. These tallies can record both energy and angular information. Since energy information is recorded the reaction rate for a particular reaction can be determined if the tally is multiplied by the energy dependent cross-section.

In principle MCNP attempts to simulate the interactions a neutron in that system would undergo. However, in some situations, generally where the tally is dependent on contribution arising from some dominating factor (i.e. strong absorption) the number of histories required to achieve adequate statistics is computationally un-feasible. In this case variance reduction techniques are required. This introduces the concept of particle weight. This can be qualitatively explained if a system consisting of a highly absorbing medium (i.e. a heavily shielded neutron source) is considered. Most neutrons will at some point in their random walk through the shield undergo absorption. This would usually terminate this particle history, referred to as the analogue case. However, if when the neutron is absorbed instead of termination the neutron survives but with its possible contribution to any tally reduced according to its probability of surviving i.e. having not been absorbed considerable improvements

in efficiency may be achieved. MCNP can treat absorption in this manner referred to as implicit capture.

Particle weight along with other variance reduction techniques are powerful tools that if applied correctly allow the user to bias a simulation towards events that contribute greatly to the tally but correct the tally to account for this biasing by adjusting the particles' weight. Variance reduction techniques in MCNP have been extensively discussed but a useful guide is the LANL Report LA-10363-MS [1.11].

A key issue when assessing the output of Monte Carlo codes is the issue of accuracy and precision. Accuracy can only be assessed from a wider evaluation of the simulation considering the uncertainties in the physical data, modelling geometry, approximations etc. In informal terms, have you actually simulated what you think?

Precision refers only to the uncertainties inherent in the Monte Carlo calculations. MCNP tallies indicate this precision by the relative error at one standard deviation of the estimated tally. For a well-behaved tally the relative error will decrease with the square root of the number of particle histories completed. It is generally recommended that tallies are considered reliable only if the relative error is less than 10% [1.1].

A further complication arises from the contribution from infrequent high weight particles. For a tally to be reliable the relative error must show the expected decrease and the range of particle weights be adequately sampled; informally, have all contributions been considered? MCNP provides extensive statistical tests and diagnostics for each tally. These examine the behaviour of the mean, the relative error, the variance of the variance and the distribution sampling. Provided all of these tests are passed the tally can be considered reliable.

1.3.2 Alpha particle modelling

The IBM code Stopping and Range of Ions in Matter (SRIM) [1.7] had been used by Darambara [1.12] to examine the behaviour of alpha particles in silicon. SRIM is a group of programs that calculate the stopping and range of ions (10 eV - 2 GeV/amu). These calculations are made very efficient by the use of statistical algorithms that allow the particle to make jumps between calculated collisions and then averaging the collision results over the intervening gap. SRIM is supplied with a large database of stopping powers for a variety of ions in many targets. Extensive use is made of the

Bragg-Kleeman rule together with empirically determined correction factors for the effect of bonding in compound targets. SRIM allows both the ion and target to be specified by atom fractions or by using a supplied database for common proprietary materials i.e. Perspex.

The ranges and LET's of the alpha, triton and lithium recoils generated by the ^{6}Li and ^{10}B (n,α) reactions calculated by SRIM in both silicon and lithium fluoride are given in Table 1.4. The selection of these two materials is discussed in Chapter 4.

Table 1.4 Ranges and LETs of reaction products from (n, α) reactions in ^{6}Li and ^{10}B

Reaction	Recoil	Recoil				Alpha			
		Range (μm)		LET (keVμm^{-1})		Range (μm)		LET (keVμm^{-1})	
		Si	LiF	Si	LiF	Si	LiF	Si	LiF
$^{6}Li(n,\alpha)$	^{3}H	41.6	32.3	43.6	58.3	7.15	5.94	242	324
$^{10}B(n,\alpha)$	^{7}Li	2.64	2.44	532	642	5.96	5.05	260	347
$^{10}B(n,\alpha)$	$^{7}Li^{*}$	2.27	2.12	529	607	4.85	4.22	281	372

SRIM also provides graphical representations of both the ion trajectories themselves and derived quantities such as LET. Shown in Figure 1.3 are two such plots for 2 MeV alpha particles in a 7 μm thick layer of lithium fluoride.

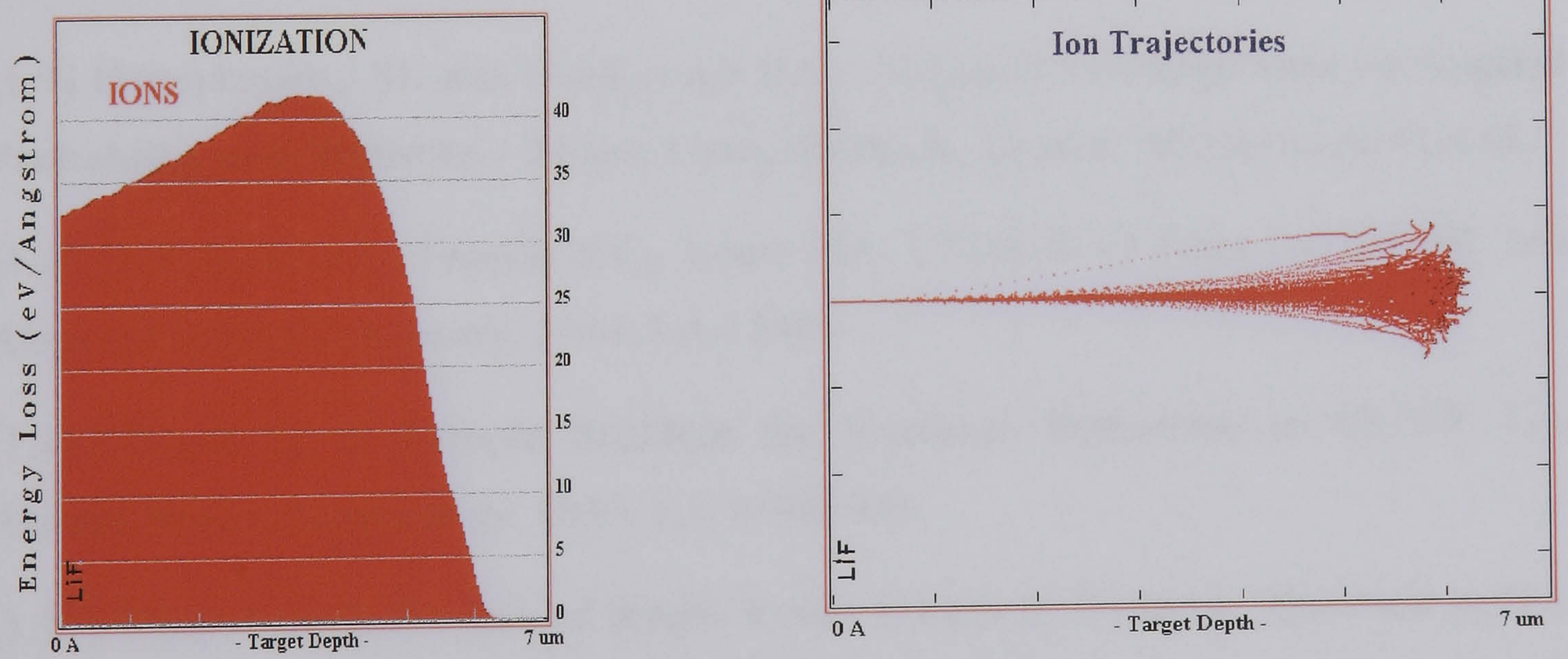

(i) (ii)

Figure 1.3 (i) Bragg curve (ii) ion trajectory

1.4 References for Chapter 1

[1.1] Briesmeister J.F. Eds. **MCNP – A General Monte Carlo N-Particle Transport Code**. Los Alamos National Laboratory, 1997. LA-12625-M.

[1.2] Amersham International, **Certificate of Measurement of Neutron Emitting Radioactive Source – Source Number AMN 1000466**. Amersham, 21st October 1975.

[1.3] British Standards Institution, **ISO 8529**. London: BSI Publications, 1998.

[1.4] Thomas D.J., Accelerator-Based Neutron Fluence Standards at NPL, Workshop on Neutron Metrology 20/4/1994, National Physical Laboratory, Teddington.

[1.5] Knoll G.F., **Radiation Detection and Measurement**, 2nd ed., Chichester: John Wiley & Sons, 1989.

[1.6] Lide D.R. Editor-in-Chief. **CRC Handbook of Chemistry and Physics 73rd Edition**, Boca Raton Florida: CRC Press, 1992.

[1.7] Ziegler J.F., Biersack J.P. and Littmark U., **The Stopping and Range of Ions in Solids"**, New York: Pergamon Press, 1985.

[1.8] ICRU Report 49, **Stopping Powers and Ranges for Protons and Alpha Particles**. Bethesda, Maryland: International Commission on Radiation Units and Measurements, 1993.

[1.9] Hammersley J.M. and Handscomb D.C., **Methuen's Monographs on Applied Probability and Statistics – Monte Carlo Methods**, London :Methuen and Co Ltd,

[1.10] Hendricks J.S., Frankle S.C., Court J.D., **ENDF/B-VI Data for MCNP**. Los Alamos National Laboratory, 1994. LA-12891

[1.11] Booth T., **A Sample Problem for Variance Reduction in MCNP**. Los Alamos National Laboratory, 1985. LA-10363-MS.

[1.12] Darambara D.G., **Use of Single Event Upsets in Dynamic Random Access Memories as the Basis for a Position Sensitive Radiation Detector**, Ph.D. thesis, University of Surrey, 1994.

Chapter 2 Neutron Dosimetry

2.1 Regulatory Framework

As early as 1900 the need to control exposure to ionising radiations had been identified. Eventually international agreement was reached and at the 1928 Second International Congress of Radiology (ICR) the International Commission on Radiological Protection (ICRP) was established. Most national legislation is based on the recommended values of dose limits as specified by the ICRP. Early ICRP publications concerned the exposure of workers to X-rays and radium sources. These were formulated in terms of time limits of exposure e.g. not more than seven hours a day, no consideration was given to the quantification of the extent of exposure. Attempts to quantify the exposure began with the use of the roentgen and evolved through a variety of quantities to the eventual SI units of the Gray and Sievert.

In the 1940's and 50's the ICRP began to consider the radiological implications of the operation of nuclear reactors. In 1977 ICRP 26 [2.1] was published which set a limit on the maximum effective dose equivalent to which a worker could be exposed. These recommendations remained in force until 1990 when ICRP 60 [2.2] was published. Before further discussing neutron dosimetry a number of units and concepts are required.

2.2. Radiation Units

2.2.1 Protection and Operational Quantities

In the ICRP publication 26 [2.1], it is recommend that the quantity to be used for internal dosimetry was the effective dose equivalent H_E. Originally conceived as a means to express non-uniform internal exposure i.e. inhalation in terms of the equivalent whole-body exposure. It was also extended to quantify exposure from external sources of radiation.

In 1979 the International Commission on Radiation Units and Measurement (ICRU) addressed the issue of measuring external exposure and recommended the introduction of two quantities for area monitoring the ambient dose equivalent H^* and the directional dose equivalent H'. The concept of protection and operational quantities was established. A protection quantity such as effective dose equivalent H_E, is specified by the ICRP in terms of the human body. An operational quantity, such as ambient dose equivalent H^*, is a quantity which may be practically measured

and can then be used to demonstrate compliance with the limits expressed in terms of protection quantities.

The most recent ICRP recommendations are those contained in the publication ICRP 60 [2.2] these introduced a number of significant changes from ICRP 26, which are discussed later. The following discussion introduces the quantities as recommended in ICRP 60.

2.2.2 ICRP 60 recommended units for external dosimetry

The most basic quantity defined is the absorbed dose D. It is defined as the mean energy imparted by ionising radiation to a medium per unit mass. If the energy is expressed in the SI unit of joules and mass is in kilogrammes then the unit is known as the Gray (1 Gy $\equiv$ 1 joule kg^{-1}).

The protection quantities are considered first, defined in Equations 2.1a-c. The fundamental quantity is the organ absorbed dose D_T, where the subscript T identifies the organ e.g. lungs, heart, etc. The organ equivalent dose H_T in units of Sieverts (Sv) is then calculated using D_T and the radiation weighting factors w_R. Radiation weighting factors are a new concept in ICRP 60 and are considered separately later. They effectively express the different biological significance of the absorption of equal amounts of energy (Grays) due to the differing interaction mechanisms of radiation. Finally, the limiting protection quantity of effective dose E, again in units of Sieverts, is defined using the tissue weighting factors w_T. Tissue weighting factors account for the different significance or detriment that exposure of different organs constitutes. They consider both radio-sensitivity and likely consequence.

$$D_T = \frac{1}{m_t}\int_{m_t} D \ \ dm \qquad \textit{Equation 2.1a}$$

$$H_T = \sum_{all\ radiations} w_R \cdot D_T \qquad \textit{Equation 2.1b}$$

$$E = \sum_{all\ tissues} w_T \cdot H_T \qquad \textit{Equation 2.1c}$$

The ICRP recommend that a workers exposure should not exceed 20 mSv per year effective dose averaged over a 5 year period and that the limit in any one year should not exceed 50 mSv. These recommendations are incorporated into UK legislation in the Ionising Radiation Regulations 1999 [2.3].

Compliance with this requirement is demonstrated using the new operational quantities. For area or survey dosimetry, i.e. measurements with hand-held instruments these quantities are the ambient dose equivalent $H^*(d)$ and the directional dose equivalent $H'(d,\Omega)$ as defined in Table 2.1. Whilst for personal dosimetry the quantity to measure is the personal dose equivalent $H_p(d)$, defined in Table 2.1.

Dose equivalent as referred to in Table 2.1 is defined as the product of the absorbed dose D and the quality factor Q. Q is a function of the radiation's linear energy transfer L in water and is defined in ICRP 60 by the following relationship, shown in Equation 2.2.

$$\begin{aligned} Q(L) &= 1 && L < 10\,keV\,\mu m^{-1} \\ Q(L) &= 0.32L - 2.2 && 10\,keV\mu m^{-1} \le L \le 100\,keV\,\mu m^{-1} \\ Q(L) &= {}^{300}\!/_{\sqrt{L}} && L > 100\,keV\,\mu m^{-1} \end{aligned} \qquad \textit{Equation 2.2}$$

An expanded field is defined as a hypothetical radiation field in which the fluence rate, angular and energy distribution has the same value throughout. An expanded and aligned field is one in which the fluence rate and energy distribution are constant but the field is uni-directional, informally a broad parallel beam.

Table 2.1 Definition of ICRP 60 Operational Quantities

Quantity	Symbol	Definition
Ambient dose equivalent	$H^*(d)$	Is the dose equivalent that would be produced by the corresponding expanded and aligned field in the ICRU sphere at a depth d, on the radius opposing the direction of the aligned field.
Directional dose equivalent	$H'(d,\Omega)$	Is the dose equivalent that would be produced by the corresponding expanded field in ICRU sphere at a depth d, on a radius in a specified direction Ω.
Personal dose equivalent	$H_p(d)$	Is the dose equivalent in soft tissue at a depth d. Practically this quantity is defined using the ICRU Slab phantom.

As may be noted from Table 2.1 the operational quantities are defined using so-called phantoms (i.e. sphere or slab). These phantoms are defined by the ICRU [2.4]. A phantom may be considered as an approximation to the human body. It is assumed that the effective dose E delivered by a radiation field is conservatively estimated by examining the same field when it is incident upon one of the representatative phantoms. For both $H^*(d)$ and $H'(d,\Omega)$ an approximation to the whole human body is required and the sphere phantom is specified. This is a sphere of 30 cm diameter made from ICRU defined tissue equivalent material. For $H_p(d)$ an approximation to the human trunk is required and a slab phantom 30 cm × 30 cm × 15 cm is specified. It was further recommended that for strongly penetrating radiation i.e. gamma and neutron that d, the depth in the phantom, be taken as 10 mm thus $H^*(10)$, $H'(10, \Omega)$ and $H_p(10)$ are the appropriate operational quantity By using well-defined and relatively simple phantoms in the definition of operational quantities both experimental and computational studies can be undertaken.

Advances in Monte Carlo techniques and computational power now allow both protection and operational quantities to be examined. The essential problem of the protection quantities is that they are defined in terms of the human body, it is only recently that computational methods have been able to cope with such a complex geometry and materials. A number of anthropomorphic phantoms suitable for use with Monte Carlo type calculations have been defined that represent the human body as a number of elliptical cylinders with different density layers. Perhaps the best known of these are ADAM and EVA [2.5]; these are based on a modified Medical Internal Radiation Dose Committee phantom (MIRD-5) [2.6].

The ICRP has published a number of compilations [2.1], [2.7], [2.8] which relate both the protection and operational quantities to basic physical quantities. In the particular case of neutron exposure these relate the ambient dose equivalent per unit fluence of neutrons at some particular energy. These are referred to as conversion coefficients, denoted by $h^*(10)$, and are conventionally quoted in pSv cm^2.

In the most recent compilation ICRP 74 [2.8] a new set of data was recommended which incorporated the recommendations of ICRP 60. These data were an evaluation of several groups' results, the details may be found in [2.8]. In the case of E the

previously described anthropomorphic phantoms ADAM, EVA and MIRD-5 were modelled whilst for *H*(10)* the ICRU sphere [2.4] was used.

A plot of the conversion coefficients for both *E(ROT)* and *H*(10)* versus neutron energy is shown in Figure 2.1. It is important to note that *E* depends on the irradiation geometry chosen, as there is significant self-absorption through the human body. In total five irradiation geometries were considered in ICRP 74. These were Anterior-Posterior (AP), Posterior-Anterior (PA), Lateral (LAT), Rotational (ROT) and Isotropic (ISO). Although idealised geometries, generally AP, PA and LAT are applicable where an individual is exposed to a single source in some fixed orientation e.g. working using a glove box (AP). A ROT geometry is suitable for a worker who moves randomly in a radiation field resulting from a widely dispersed source. Whilst the ISO geometry is suited to representing a worker immersed in a cloud of radioactive gas. The five-irradiation geometries are shown in Figure 2.2.

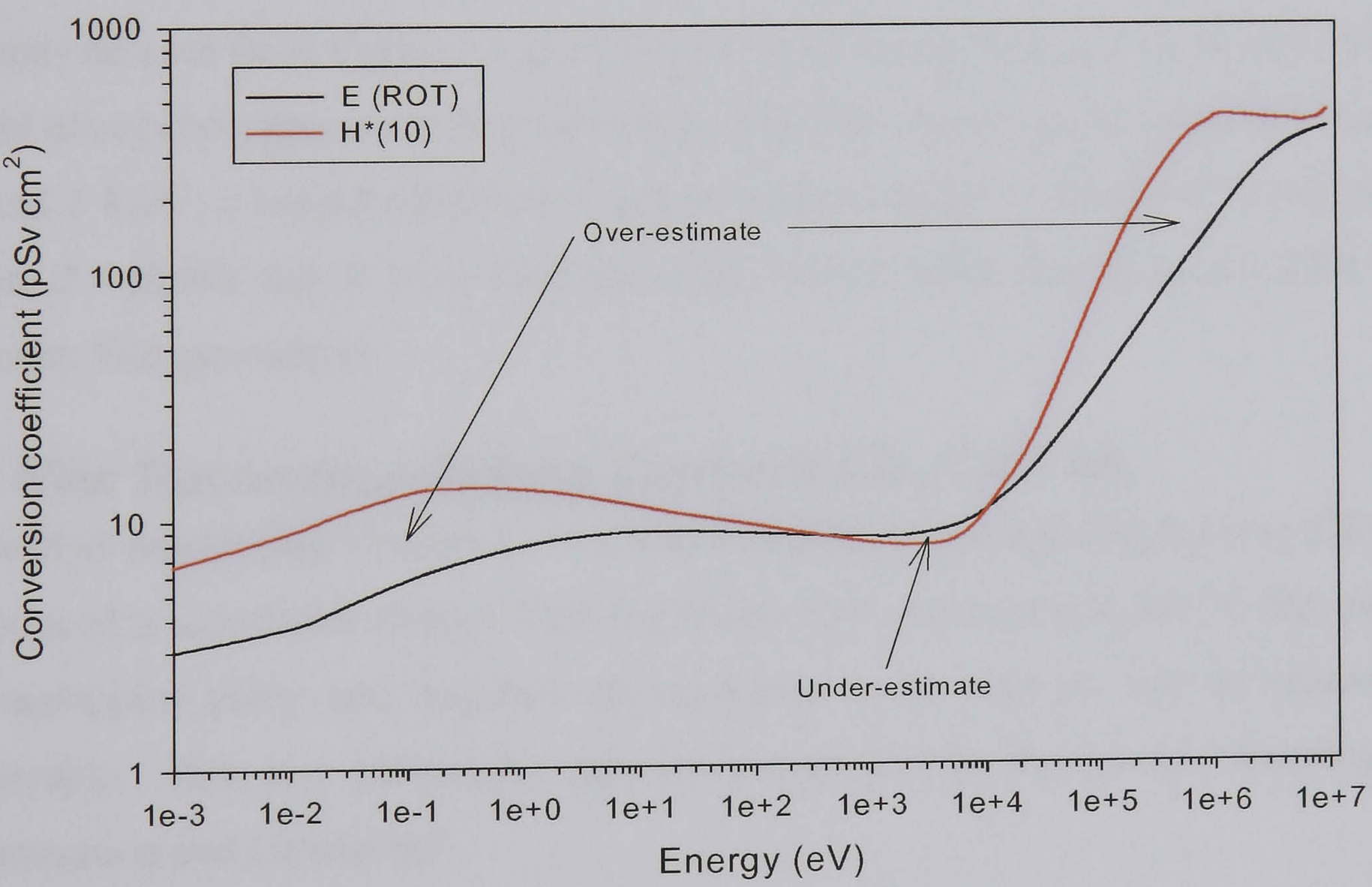

Figure 2.1 ICRP 74 Conversion Coefficients

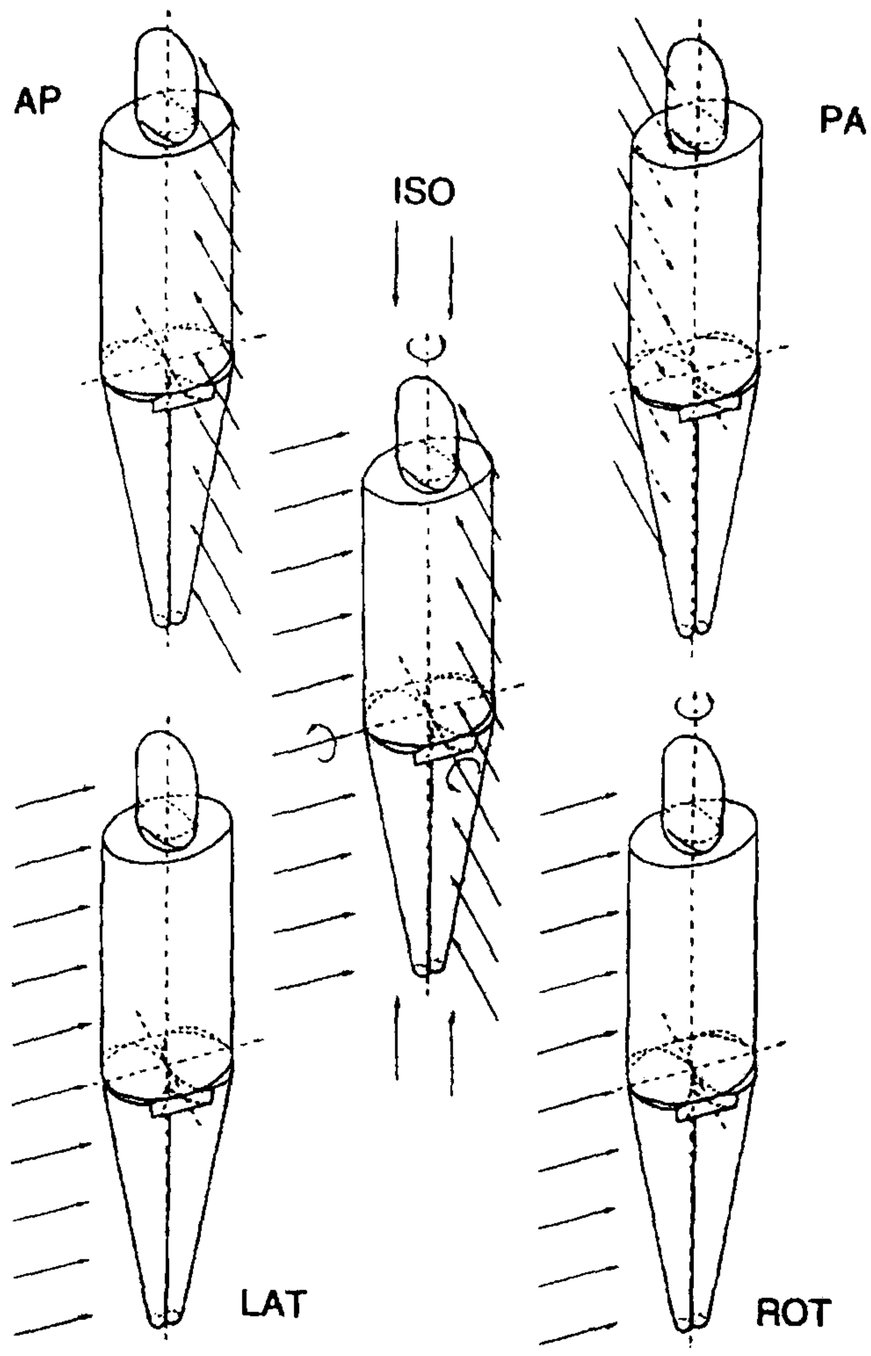

Figure 2.2 Irradiation geometries redrawn from [2.8]

As may be seen from Figure 2.1 apart from a small region between 1 keV and 10 keV E will always be conservatively estimated by *H*(10)*. However, in the worse case, at around 1 MeV, a considerable over-estimate (approximately a factor of 3) can occur. Figure 2.1 shows only *E* for a rotational field, similar behaviour is observed for *E* in the other four geometries.

2.3 New Recommendations Contained in ICRP 60

As well as introducing a number of technical changes (i.e. weighting factors) ICRP 60 introduced a significant change from the philosophy underlying ICRP 26 that simply set maximum limits and required all exposures to be kept as low as reasonably achievable. This new philosophy may be summarised by the phrase "Justification, Optimisation and Limitation".

- *Justification* - No practice which results in radiation exposure should be undertaken unless there is a clear benefit to the workers/society that outweighs the detriment caused.

- *Optimisation* – All exposures shall be as low as reasonably achievable subject to constraints such as economic or social factors.

- *Limitation* – An exposed individual's dose shall not exceed the limits recommended by the ICRP.

Whilst limitation can, in principle, easily be achieved it is the justification and optimisation stages that have proved more problematic. A discussion of these issues is beyond the scope of this thesis but essentially the question are "How do we quantify detriment?" and "How low is reasonable?".

The major technical changes that impacted upon neutron dosimetry were [2.9]; a reduction in the annual effective dose limit to 20 mSv, the introduction of radiation weighting factors and the revised Q(L) relationship for operational quantities.

The reduction in the dose limit from 50 mSv [2.1] to 20 mSv and the consequent reduction in the required minimum detectable dose imply that an increase in sensitivity will be required of dosimetry services. Additionally a radiation worker is now considered to be any individual whose annual effective dose exceeds 1 mSv; previously the public limit had been set at 5 mSv; requiring a reduction in the minimum detectable dose.

Under the previous recommendations [2.1] the quality factor *Q(L)* had been used to define both the operational and protection quantities. However, ICRP 60 introduced radiation weighting factors w_R in the definition of protection quantities and also revised the previous *Q(L)* relationship.

Considering first the new radiation weighting factors w_R. For neutrons, with an energy E in MeV, w_R was defined using the following expression, Equation 2.3

$$w_R(E) = 5 + 17e^{\left[\frac{-(\ln(2E))^2}{6}\right]} \qquad \textit{Equation 2.3}$$

The newly revised *Q(L)* relationship used for operational quantities effectively increased the *H*(10)* per unit fluence rate. Shown in Figure 2.3 are the old *Q(L)* of ICRP 26 and the new *Q(L)* of ICRP 60.

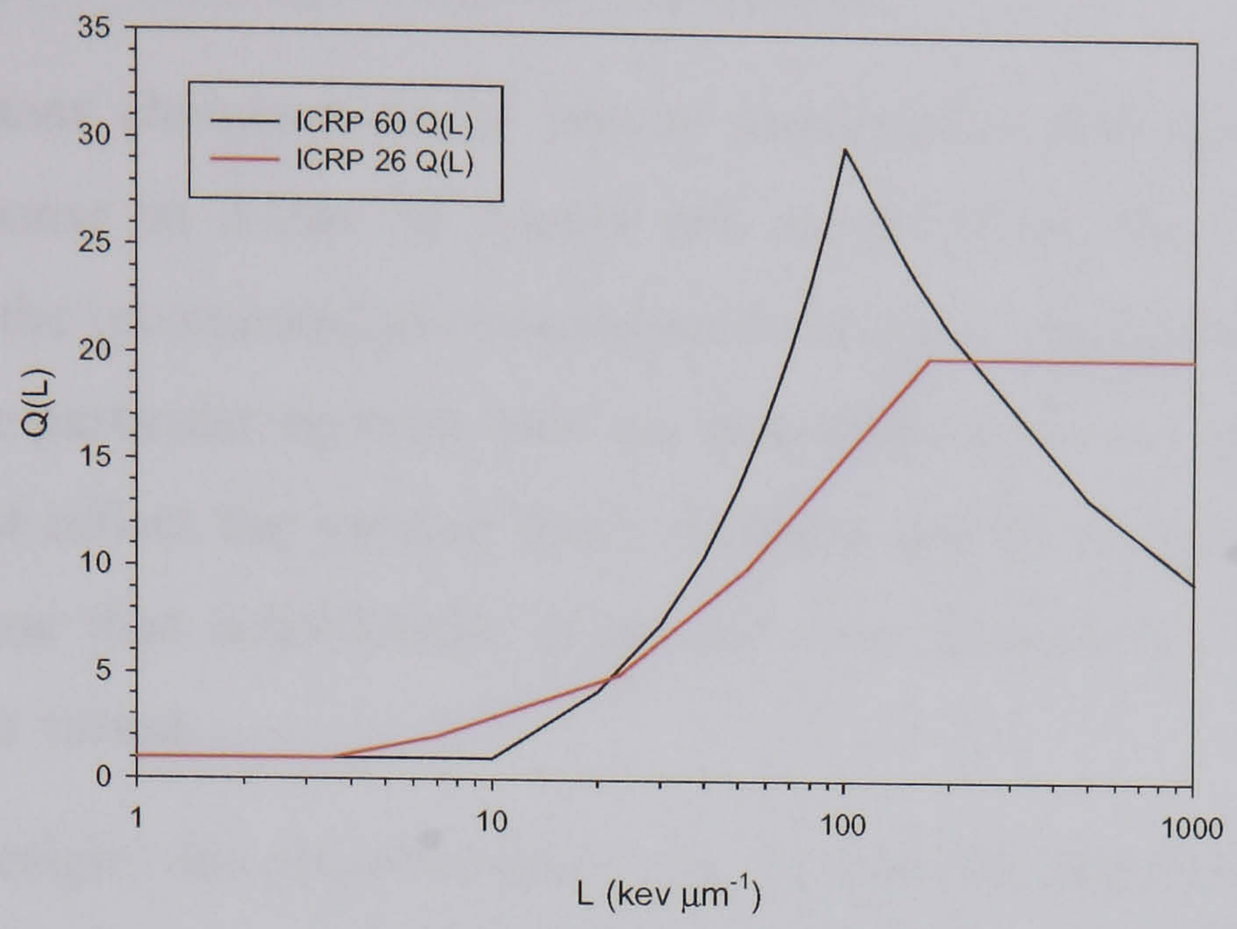

Figure 2.3 Q(L) relationship

As may be seen, the values for Q(L) tend to be larger under the ICRP 60 recommendations in the region of most interest i.e. LET's corresponding to typical fission generated neutron radiation fields between 10 and 200 keV μm^{-1}.

2.4 Review of Some Existing Area Survey Instruments

It is convenient to separate these instruments in two groups; the "classic" designs (1950's and 60's) such as Leake and the modern designs. Later, in Chapter 3, the responses of some of these instruments are examined with particular reference to the energy spectra in and around pressurised water reactors (PWR).

2.4.1 "Classic" Neutron area survey instruments

These instruments all tend to share a number of common features. They usually consist of a central gas filled thermal neutron detector located within a large moderating assembly. The thermal neutron detector is either a boron trifluoride (BF_3) or a helium filled proportional counter. These detectors take advantage of the high cross-section (n,α) reaction of ^{10}B or the (n,p) reaction of ^{3}He. An incident thermal neutron will be captured and cause the emission of energetic highly ionising particles. The ionisation these alpha particles produce in the fill gas can then simply be detected. Inherently, these detectors have good gamma rejection capabilities. The Q-value of the (n,α) reaction is typically MeV and so it is possible using a simple pulse height criterion to reject weakly ionising events resulting from gamma ray

interactions. Without exception the preferred moderating material is polyethylene, this material is both stable and is highly hydrogenous.

It is an important characteristic of survey instruments that their neutron energy dependent response in terms of counts per second from the central detector is proportional to the recommended conversion coefficients. Since details of the energy spectrum of the particular neutron field are frequently unknown the response of the instrument must reflect the varying doses different energy neutrons deliver. If this were not the case then considerable under and over response would be seen as the energy spectrum varied.

In the classic designs this proportionality was achieved by selection of the moderator geometry and the inclusion of a shield of thermal neutron absorbing materials, often cadmium or boron, around the central detector. Qualitatively, their operation can be explained by considering neutrons incident on the moderator. A low energy neutron, delivering a relative small dose, will quickly be moderated in the polyethylene and either absorbed by hydrogen or in the thermal shield. The instrument will show a small response to these neutrons. However, higher energy neutrons, delivering a large dose, will penetrate deeper and are consequently less likely to be absorbed before reaching the central detector. The instrument will show a large response. By careful selection of the moderator size and position of the thermal shield it is possible to achieve a response that is reasonably proportional to the conversion coefficients. A cross-sectional diagram of a typical instrument, a Leake type, is shown in Figure 2.4.

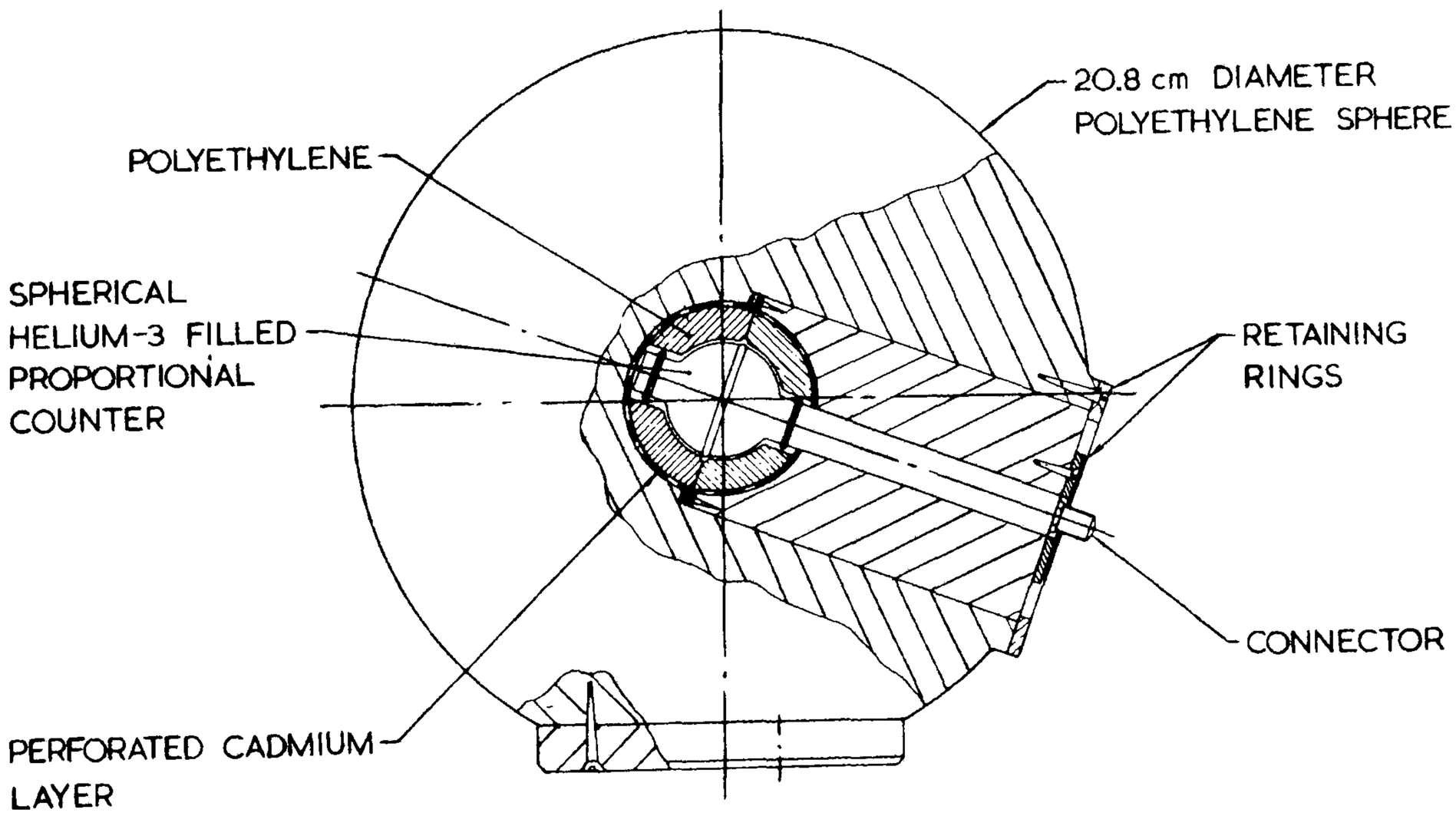

Figure 2.4 Cross-section of Leake type survey instrument redrawn from [2.10]

2.4.1.1 The Leake type spherical instrument

Leake [2.10,2.11] in 1968 described a device that consisted of a 20.8 cm diameter polyethylene sphere within which was located a 3.0 cm diameter (Centronics type SP9) ^{3}He counter. Surrounding this detector was a perforated cadmium shell with a diameter of 5.4 cm. The perforation in the cadmium shell ensures that the instrument has an adequate low energy response by permitting a fraction of neutrons already thermalised in the outer layers to reach the central detector. This design has also been referred to as the "Harwell type 95/0075" and later as the "Harwell type 0949" and was commercially produced by Nuclear Enterprises Ltd as the Mark 7 NRM. It is worth noting that the UK Ministry of Defence selected the Mark 7 NRM for area neutron dosimetry.

This instrument achieved a reasonable fit to the conversion coefficients as defined at that time, however, the instrument does have an over-response to neutrons in the keV region. In 1979 Harrison [2.12] reviewed a number of measurements of the instrument's response and concluded that for a bare fission spectrum the Mark 7 NRM would under estimate the true dose by 27% whilst for concrete shielded 14 MeV neutron source would under estimate the true dose by 59%. Harrison also noted that in spectra with considerable fluence rate in the keV region over estimation of true dose by 287% was possible.

A similar but more extensive study by Naismith in 1997 [2.13] using measured energy spectra from a number of nuclear facilities also indicated that the over response to keV neutrons was significant. In the case of typical fields in an around a PWR the over response could be as large as 283%.

2.4.1.2 The Andersson-Braun type cylindrical instrument

In 1964 Andersson and Braun [2.14] described a cylindrical shaped device. This device made use of a central cylindrical BF_3 detector that was surrounded by a perforated shield fabricated from a borated plastic. Two commercial versions, each differing slightly from the original design, are available. The Nuclear Enterprises NM2 [2.15] has a moderator that is slightly wider and shorter (21.6 cm diameter, 25 cm length) and uses a Centronics type 6EB60/30 BF_3 detector with a diameter of 3 cm and active length 6 cm. To address the angular response of the original design the

Studsvik 2202D [2.16, 2.17] has a rounded end to the cylinder (21.5 cm diameter, 23 cm length) and uses a proprietary BF_3 detector.

Naismith [2.13] also examined the response of the 2202D in realistic fields. She concluded that in typical PWR fields the 2202D estimated dose well. However, in particular fields a small under estimate, by approximately 20% was possible.

2.4.2 Recent developments in neutron survey instruments

Recent innovations in neutron survey instruments can be separated into two distinct groups. Some new designs have retained the essential principles of earlier "classic" designs i.e. large polyethylene moderator and central detector but have concentrated on using modern neutron transport codes to optimise and refine the instruments energy dependent response function. The second group consists of instruments that incorporate additional detectors or multiple moderating bodies.

2.4.2.1 The EG&G Berthold LB6411 REM Counter

This device is a recent commercial development and it demonstrates well the first approach to an improved survey instrument. First described in 1997 by Burgkhardt [2.18] it consisted of a 25 cm diameter polyethylene sphere with a central ^3He proportional counter. A perforated cadmium shell surrounds the central detector, the dimensions of which are not described.

Burgkhardt describes the extensive optimisation using MCNP that was undertaken, parameters such as the diameter, absorber position and perforations were varied. The energy dependent response function of the resulting configuration was determined at 47 points and validated by calibration measurements at the Physikalisch-Technische Bundesanstalt (PTB) using accelerator produced monoenergetic neutrons between thermal and 19 MeV.

It was reported that this new design was approximately four times more sensitive than a Leake type instrument with a reduction of approximately three fold in the over-response to keV neutrons. Using a catalogue of neutron spectra [2.19] they examined the response of this instrument in a number of fields representative of nuclear facilities. They concluded that the LB 6411 indicated $H^*(10)$ to within +10% and –30% for this group of spectra.

2.4.2.2 The CEA Dineutron

This instrument first described in 1985 by Mourgues et al [2.20] consists of two ^{3}He proportional counters located at the centre of two polyethylene spheres with diameters of 6.35 cm and 10.67 cm. The instrument's response is determined both from the count rates from the central detectors and by using a spectral correction factor derived from the ratio of the two count rates. This was the first commercial device that attempted to correct for deficiencies in the energy dependent response by using a parameter that was dependent on the spectrum e.g. the relative response of two different diameter and hence energy response spheres.

According to the manufacturer's information *H*(10)* is indicated to with ±30% for all energy neutrons. However, later Hankins et al [2.21] reported that the Dineutron significantly over responded relative to the desired ICRP 74 *H*(10)* response to keV neutrons. In a later study by Hunt [2.22] an over estimation of *H*(10)* by 40% was reported for bare ^{252}Cf and by 200% for D_2O moderated ^{252}Cf. Using measured spectra in an around PWRs and BWRs Aroua et al [2.23] reported that the Dineutron could over estimate *H*(10)* by as much as 400% in very soft neutron fields if calibrated using ^{252}Cf. Whilst if calibrated with the low mean energy D_2O moderated ^{252}Cf spectrum significant under estimation could occur. Rimpler [2.24] reported even larger over estimations in the vicinity of used fuel transport casks.

2.4.2.3 The National Radiological Protection Board (NRPB) Spherical Dose Equivalent Survey Instrument

This device described by Bartlett et al [2.25] attempted to correct for the energy deficiencies of its central detector by combining its response with an outer detector. It consisted of a 3.0 cm ^{3}He proportional counter located at the centre of a polyethylene sphere with a diameter of 21.3 cm. Surrounding the central detector was a 2.4 cm layer of polyethylene then 1.5 cm layer of a proprietary boron loaded plastic. Located orthogonally 2 cm below the surface of the sphere were six photodiodes onto which had been deposited a layer of ^{6}Li rich material.

The count rates from both the inner ^{3}He and outer photodiodes were summed with a normalisation factor so that their combined response fitted the ICRP 74 conversion coefficients. Fits to both *H*(10)* and *E(AP)* were made. It was suggested that the ratio of the inner to outer count rates could be used to calculate a 'spectrum hardness'

factor and additionally that the ratio of opposing detector pairs could derive crude angular information.

MCNP calculations validated by mono-energetic exposures at the National Physical Laboratory were used to determine the instrument's response function. The combined response under estimated *H*(10)* at worst by 60%. Whilst this fit is not ideal a much better result was achieved when the actual protection rather than operational quantity was considered. *E(AP)* over the range thermal to 10 MeV was at most under estimated by 10% and over estimated by 80%. Whilst *H*(10)* is defined as the quantity to be measured for area dosimetry it is extremely useful to be able to confirm that *H*(10)* is correctly estimating *E*.

2.4.2.4 The LANL Wide Energy Neutron Detection Instrument (WENDI)

Development of this device began in 1992 with the aim of producing a new universal rem meter, with good high-energy response and improved accuracy at intermediate energies (50 – 250 keV) [2.26]. Rather than modify existing designs an entirely new design was developed.

In its original form WENDI used a three layer spherical moderator (24.6 cm diameter) and a central cylindrical BF_3 detector. A number of novel features were incorporated in this design that resulted from extensive Monte Carlo optimisation studies [2.27]. Most significantly the outer layer (6.48 cm) of the moderator was fabricated from a tungsten loaded polyethylene (30% by weight). The tungsten loading served two purposes; to extend the high-energy response ($E > 8MeV$) and to reduce the over-response to intermediate energies.

First investigated by Birattari [2.28] the inclusion of a heavy metal shell was proposed as a means to extend the high-energy response of conventional neutron dosemeters. Lead, gold and tungsten all exhibit a relatively high cross-section (about 2 barns) for the threshold (n,2n) reaction. For neutrons with an energy above this threshold (approximately 8 MeV) the instrument's response will be greatly enhanced by the generation of lower energy neutrons in the heavy metal shell. At even higher incident neutron energies, around 14 MeV, the (n,3n) reaction is also feasible and further enhances the high-energy response. An additional advantage of tungsten over the other possible heavy metal converters was that it displayed high absorption

resonances in the region of 0.1 to 1.5 keV. Strong absorption in this energy region allowed the over-response to intermediate energies to be reduced.

In the original WENDI design a layer (approximately 3mm) of boron loaded plastic, 5% by weight, was included, this served a similar purposes (i.e. to reduce the over-response to thermal neutrons) to the cadmium shell in the Leake design but avoided the toxicity of cadmium. Located within this shell was a pure polyethylene shell (diameter 11 cm) with a central void into which fitted the BF_3 detector. To prevent neutron streaming down the cable pathway to the detector a heavily borated plastic, 25% by weight, patch was applied over and around the cable pathway.

Development then proceeded to the WENDI-II intended for commercial production. To simplify manufacturing a cylindrical moderator (22.86 cm diameter, 21 cm long) replaced the previously spherical design and pure polyethylene rather than tungsten loaded was used. Instead of using a borated plastic shielded around the central detector a 1.5 cm thick layer of tungsten powder was used. This layer acted both to enhance the high-energy response through (n,2n) reactions and also to reduce the intermediate energy over-response. To increase the sensitivity of the new design a ^3He counter replaced the BF_3 counter.

Primarily intended for use as an extended range high energy dosemeter the WENDI-II estimates H*(10) well (- 48%, +82%) in the range 0.1 MeV to 5 GeV. At intermediate energies its response is comparable to earlier classic designs although the use of a high-pressure ^3He detector greatly enhances its sensitivity. The greatest reservation regarding WENDI-II is the considerable weight penalty, around 5 kg, due to the tungsten loading. With a total mass of nearly 15 kg it is transportable rather than portable.

2.4.2.5 Extended Range Instruments

A number of groups have published designs for neutron survey instruments that extend their useful range beyond the typical 10 MeV range to the 100's of MeV. These designs are intended to monitor the exposure to very energetic neutrons arising from cosmic ray interaction or from the operation of high-energy accelerators. It would not be practicable to simply increase the diameter of the moderating sphere to accommodate these higher energies. Instead heavy metals such as lead and tungsten are positioned as shells around or inside a conventional moderating design. These

designs are beyond the scope of this thesis but [2.29, 2.30] describes two such designs and their experimental verification.

2.5 Review of Current Personal Dosimetry

As well as demonstrating compliance with the dose limits by means of area surveys combined with exposure times traditionally personnel dosimetry has also been employed. Devices designed for personal neutron dosimetry can be divided into two distinct groups, active and passive. Passive dosimetry is the more mature field and a number of distinct technologies have been favoured. Perhaps the two best known are track etch systems and nuclear track emulsions. Active personal neutron dosimetry has proved difficult to achieve; the required energy response and sufficient sensitivity to high-energy neutrons are considerable challenges.

2.5.1 Passive Personal Dosemeters

Descriptions of a great number of detectors for personal neutron dosemeters have been published; various designs of holder and filter arrangements have been proposed which modify the overall badges response. A full discussion of these many systems is beyond the scope of this thesis, however, the two most commonly encountered systems including that favoured for use in and around naval PWR plant is given below.

2.5.1.1 Nuclear Track Emulsion

Neutron dosimetry undertaken with nuclear emulsions relies on the production of a charged particle within the emulsion itself. In essence nuclear emulsions are similar to conventional photographic emulsions except that the loading of the photosensitive chemical, typically silver nitrate, is higher and the emulsions are much thicker. One of the most widely used emulsions is the Eastman-Kodak NTA film. This has sensitivity to both thermal and fast neutrons. Fast neutron detection is achieved directly through the generation of recoil protons from elastic scattering interactions with hydrogen nuclei in the emulsion itself. These recoil protons then cause ionisation along the length of their track that is sufficient to cause silver nitrate to reduce to metallic silver. These latent tracks are then developed and fixed using conventional photographic techniques. The necessity of maintaining the physical dimensions of the emulsion during a number of 'wet' processes requires careful

control. Whilst for thermal neutrons the (n,p) capture reaction in ^{14}N generates 0.6 MeV protons that are then detected in a similar fashion to the recoil events.

The NTA films are held in a badge that serves a number of purposes. Firstly, they incorporated a lead shield to reduce the film's response to gamma rays and remove unwanted recoil protons generated in the plastic of the holder itself. When worn on the body the back face of the film must be shielded, usually with cadmium, to prevent the large number of low energy neutrons generated by back scattering in the body, often called albedo neutrons, from overwhelming the response to fast neutrons.

In the UK the NRPB operate a neutron dosimetry service using NTA film [2.31]. The response falls with decreasing neutron energy with a cut-off at around 0.5 MeV and again rises at thermal (< 10 eV). Typical sensitivities for this system are in the range 1×10^4 tracks mm^{-2} Sv^{-1}.

The effect of the poor low energy sensitivity of NTA based personal dosimetry system was illustrated by Naismith [2.13]. Naismith examined two NTA services, one with thermal sensitivity and one without. Using a catalogue of measured spectra she calculates the ratio of the "measured" $H_p(10)$ to the true $H_p(10)$ of these systems in a variety of radiation fields. No location correction factors were applied to either system but the effect of using either ^{252}Cf or $^{241}Am/Be$ as the calibration source was examined. These results are summarised below in Table 2.2.

Table 2.2 Responses of two NTA dosemeters in various fields from [2.13]

Spectrum Group	Mean Energy (keV)	NTA (with thermal)		NTA (no thermal)	
		^{252}Cf	$^{241}Am/Be$	^{252}Cf	$^{241}Am/Be$
GCR	21	5.45	3.76	0.07	0.05
PWR 1	26	8.6	5.93	0.08	0.05
BWR 1	27	10.7	7.38	0.12	0.08
BWR 2	76	2.17	1.50	0.22	0.16
PWR 2	110	1.32	0.91	0.28	0.20
PWR 3	350	0.75	0.52	0.39	0.27
BWR 3	360	0.40	0.28	0.39	0.27
Transport Cask	290	0.62	0.43	0.31	0.21
Reprocessing	1000	0.93	0.64	0.74	0.51

2.5.1.2 Track Etch

All track etch systems rely on the damage caused to some material when a neutron interacts. In the case of fast neutrons this is predominately through the generation of MeV recoil protons in scattering interactions in some hydrogenous material although capture reactions yielding highly ionising particles such as alpha particles can also contribute to a sensitivity to thermal neutrons. Many materials have been considered for use in track etch systems depending on the radiation and total dose to measure.

By far the most frequent choice for neutron dosimetry is poly allyl diglycol carbonate (PADC) also known by the trade names CR-39. Both the National Radiological Protection Board (NRPB) [2.32] and Defence Radiological Protection Board (DRPS) [2.33] operate such a service. The NRPB operated service quotes 200 μSv [2.34] as it minimum detectable dose, similarly for the DRPS operated service. Both these minimum detectable doses were quoted using the previous Q(L) relationship of ICRP 26 and, therefore, with the introduction of the new Q(L) relationship in ICRP 60 it is expected that these values will increase if no remedial action is taken. [2.34]. However, there is an important distinction between the two systems, the NRPB system is sensitive to thermal neutrons through the $^{14}N(n,p)$ reaction in the Nylon badge holder. Without such a radiator CR-39 is insensitive to low energy ($E_n < 200$ keV) [2.35, 2.36]. DRPS correct for this insensitivity by applying a location correction factor (LCF) [2.37].

The LCF is simply a multiplying constant determined with knowledge of the calibration and operational neutron energy spectra. Typical values are in the range 1 to 4, an LCF of 1 indicates that the calibration and operational energy spectrum are the same. A further correction can also be made for the non-isotropic angular response of the planar CR-39 element if the angular distribution of the neutron field is either measured or assumed.

The effect of the poor low energy sensitivity of a non-radiator CR-39 based personal dosimetry system was illustrated by Naimsith [2.13]. She examined two un-named CR-39 one with a radiator and one without. Using a catalogue of measured spectra she calculated the ratio of the "measured" $H_p(10)$ to the true $H_p(10)$ of these systems in a variety of radiation fields. No LCF factors were applied to either system but the

effect of using either ^{252}Cf or ^{241}Am/Be as the calibration source was examined. These results are summarised below in Table 2.3.

Table 2.3 Responses of two track etch dosemeters in various fields from [2.13]

Spectrum Group	Mean Energy (keV)	PADC (with radiator)		PADC (no radiator)	
		^{252}Cf	^{241}Am/Be	^{252}Cf	^{241}Am/Be
GCR	21	0.55	0.65	0.27	0.32
PWR 1	26	0.53	0.62	0.25	0.30
BWR 1	27	0.59	0.70	0.34	0.41
BWR 2	76	0.67	0.79	0.53	0.65
PWR 2	110	0.74	0.87	0.61	0.74
PWR 3	350	0.83	0.98	0.74	0.89
BWR 3	360	0.89	1.05	0.80	0.97
Transport Cask	290	0.81	0.95	0.73	0.88
Reprocessing	1000	0.99	1.17	0.95	1.15

2.5.1.3 Other Passive systems

These systems are generally restricted to specialised areas where workers are exposed to a fixed source of neutrons and work in a highly repeatable environment e.g. neutron source fabrication or fissile material handling in glove boxes. The most important of these systems are the albedo thermoluminescent detector (TLD) and the fission dosemeter.

Fission Dosemeter

These systems make use of the high cross-section shown by ^{235}U (thermal neutrons), ^{237}Np (fast neutrons) and ^{232}Th (fast neutrons) for the fission reaction. The fission reaction generates two highly ionising fission fragments, which may easily be detected by etching an organic polymer that was in intimate contact with the fissile material to reveal the fission fragments track. Two such systems are the Harwell ^{237}Np dosemeter that is essentially sensitive only to fast neutrons (> 0.5 MeV) and the combined ^{235}U and ^{232}Th dosemeter produced by the Paul Scherrer Institute that has both thermal (< 10 eV) and fast sensitivity (> 1 MeV). The limited energy response of this system dictates that a correction factor, determined with knowledge of the

operational energy spectrum, has to be applied. Unfortunately all of the fissile materials discussed are themselves radioactive. The additional surface doses received by wearers and the handling constraints has meant these Dosemeters have not been widely used.

Thermoluminescent Detectors (TLD)

Neutrons, as uncharged particles, cannot be directly detected by TLD systems. Fortuitously a common TLD material lithium fluoride (LiF) can be sensitised to neutrons. Conventional, i.e. intended for photon dosimetry, TLD systems use ^{7}LiF, however, if instead ^{6}LiF is used then through the high cross-section (n,α) reaction thermal neutrons can be detected.

The range of TLD dosemeters is very wide and they are extensively discussed by Gibson [2.38] and Piesch [2.39]. In the simplest form a TLD based neutron dosemeters consisted of a pair of ^{7}LiF and ^{6}LiF TLDs mounted in a badge such that when worn on the body they are well shielded from incident thermal neutrons. This shielding usually consists of borated plastic although cadmium has also been used. The dosemeter is therefore only sensitive to the thermal neutrons leaving the body, often called albedo neutrons, which have originated from fast neutrons undergoing scattering within the body itself.

Commercial albedo dosemeters are produced by Alnor, Harshaw, Panasonic and Vinten [3.39]. Whilst these differ slightly from each other, mainly related to the size and packaging of the individual TLD elements, they all make use of the so-called universal albedo neutron dosemeter capsule [2.40].

TLD dosemeters exhibit a high sensitivity and by using paired detectors a good immunity to gamma rays. Due to their reliance on back scattering within the human body they have a strong energy and angular dependence [2.41,2.42]. If accurate spectral information is available then the dosemeter readings can be corrected [2.43]. It is for this reason that TLD neutron dosemeters are favoured where workers are exposed to highly repeatable neutron fields.

2.5.2 Active Personal Dosemeters

A wide variety of detectors have been proposed for use in an active neutron dosemeter and are well reviewed by Bartlett [2.44] and Barthe [2.45]. In broad terms four types

of active dosemeter were identified; the tissue equivalent proportional counter, diodes, memory devices and superheated drop or bubble detectors.

2.5.2.1 Tissue Equivalent Proportional Counter (TEPC)

A TEPC, for use as a personal dosemeter, consisting of a small cylindrical or spherical proportional counter whose walls and fill gas closely resemble the elemental composition of tissue. Traditionally this gas has been a mixture consisting of 64.4% methane, 32.4% carbon dioxide and 3.2% nitrogen. In effect they simulate a small volume ($\approx \mu m^3$) of tissue. When such a counter is irradiated with neutrons recoil protons are generated in the walls of the counter that can then be detected by the ionisation they produce in the fill gas. Provided that the fill gas pressure is such that the energy loss as the recoils traverse the counter is negligible and the path length distribution can be analytically determined, a pulse height spectrum of the energy deposition can be unfolded to determine the dose equivalent to the simulated tissue volume.

Although a number of TEPC based systems have been developed [2.46, 2.47] which showed good sensitivity, approximately 10 counts μSv^{-1} these systems have been beset by problems of microphony, power consumption and high fabrication costs. TEPC's are likely to remain a 'research' tool capable of providing detailed spectrometric information but unsuited to the rigours of routine operational use.

2.5.2.2 Diode detectors

These designs all share a number of common features. A p-n junction formed in silicon is arranged such that ionising particles generated in some external converter can deposit their energy into the depletion region. The electron-hole pairs so generated can then be collected and either a simple count rate or pulse height distribution collected. Thermal neutrons may easily be detected by using a converter of either ^{6}Li or ^{10}B and detecting the resulting alpha particles generated by the (n,α) reaction. Fast neutrons can be detected if a hydrogenous converter is applied; in this case it is recoil protons resulting from scattering interactions that are detected.

Aloka in Japan has produced a commercial device. It consisted of two silicon diodes, a hydrogenous layer was deposited on the surface on one diode whilst the second had a boron converter layer. Deficiencies in its energy response were identified [2.48] particularly in the region 0.1 to 100 keV where a significant over-response (by factors

of 10) was reported. Although predominately neutron sensitive achieving good gamma rejection has proved difficult. A simple pulse height criterion compromises the response to keV neutrons, as the discrimination between photons and keV recoil protons is not easily achieved. Schemes have been proposed [2.49] where paired diodes are used with and without converters and a simple subtraction used to remove the gamma-induced signals. However, difficulties in matching the detector pairs have lead to apparently negative doses [2.45].

2.5.2.3 Memory Devices

A full discussion of these detectors is provided in Chapter 4. Briefly, semiconductor memory devices in which data is stored in a binary fashion by the charge state of small cells (μm^3) are susceptible to errors induced by charged particles depositing energy in the region of the storage cells. Similar converter schemes to those discussed for diode systems have been proposed.

2.5.2.4 Superheated drop or bubble detectors

This device was first proposed by Apfel in 1979 [2.50] and Ing [2.51] in 1984. These detectors consist of an inert gel like material in which a large number of microscopic droplets of a superheated liquid are suspended. A superheated liquid is in a phase state in which the liquid is at a temperature above its boiling point but boiling has not been initiated. In the case of fast neutrons sufficient ionisation will be produced by the recoil protons generated in the gel to initiate the boiling of the superheated liquid. Intermediate energy and thermal neutrons do not generate sufficiently energetic protons and instead a chlorine loaded gel is used. The $^{35}Cl(n,p)^{35}S$ reaction generates a proton recoil that is sufficiently ionising to initiate boiling.

Once boiling has been initiated the droplets of superheated liquid expand rapidly. In the simplest systems the number of bubbles can be visually counted, optical scanners can also be used to increase throughput. In more sophisticated system acoustic sensors are coupled to the fluid and the characteristic 'noise' of boiling is detected. As these detectors are strongly affected by temperature active systems often incorporate a temperature controller and heater element to stabilise the gels temperature. It is this temperature dependence that has been used to develop a spectrometer based on bubble detectors whose energy threshold can be varied by varying the gels temperature [2.52]. Typical sensitivities are 2 bubbles μSv^{-1}.

2.5 References for Chapter 2

[2.1] International Commission on Radiological Protection Publication 26, **Recommendations of the International Commission on Radiological Protection**. Oxford: Pergamon Press, 1977.

[2.2] International Commission on Radiological Protection Publication 60, **1990 Recommendations of the International Commission on Radiological Protection**. Oxford: Pergamon Press, 1991.

[2.3] Statutory Instrument No. 3232, **The Ionising Radiation Regulations 1999**. London, UK: Her Majesty's Stationery Office, 1999.

[2.4] ICRU Report 48, **Phantoms and Computational Models in Therapy, Diagnosis and Protection**. Bethesda, Maryland: International Commission on Radiation Units and Measurement, 1992.

[2.5] Kramer R., Zankl M., Williams G., Drexler G., **GSF-Bericht S-885 - The calculation of dose from external photon exposures using the reference human phantoms and Monte Carlo methods. Part I the male (ADAM) and female (EVA) adult mathematical phantoms**. Munich: Gesellschaft für Strahlen – und Umweltforschung mbH., 1982.

[2.6] Snyder W.S., Ford M.R., Warner G.G., Fisher H.L., **MIRD Pamphlet No.5 - Estimates of Absorbed Dose Fractions for Mono-energetic Photon Sources Uniformly Distributed in Various Organs of a Heterogeneous Phantom**. New York: Society of Nuclear Medicine, 1969.

[2.7] International Commission on Radiological Protection Publication 51, **Data for Use in Protection Against External Radiation**. Oxford: Pergamon Press, 1987.

[2.8] International Commission on Radiological Protection Publication 74, **Conversion Coefficients for use in Radiological Protection against External Radiation**. Oxford: Pergamon Press, 1996.

[2.9] Tanner R.J., Bartlett D.T., Steele J.D, NRPB PADC neutron personal dosimetry after ICRP 60, **Nucl. Tracks Radiat. Meas.**, 22(1-4), 703, 1993.

[2.10] Leake J.W., An improved Spherical Dose Equivalent Neutron Detector, **Nucl. Inst. & Meths.**, 63, 329, 1968.

[2.11] Leake J.W., Spherical Neutron Dose Equivalent Neutron Detector Type 0075, **Nucl. Instrm. & Meths.**, 178, 287, 1980.

[2.12] Harrison K.G., The Response of a Spherical Neutron Survey Meter, **Nucl. Instrm. & Meths.**, 166, 197, 1979.

[2.13] Naismith O.F., Siebert B.R.L., Thomas D.J., Response of Neutron Dosemeters in Radiation Protection Environments: An Investigation of Techniques to Improve Estimates of Dose Equivalent, **Rad. Prot. Dosim**., 70(1-4), 255, 1997.

[2.14] Andersson I.Ö. and Braun J., A Neutron Rem Counter, **Nukleonik**, 6, 237, 1964.

[2.15] Nuclear Enterprises data sheet on NM2

[2.16] Widell C.O. and Svansson L., Neutron Monitor for Radiation Protection, **Neutron Monitoring for Radiation Protection Purposes**, Proceedings of a Symposium, Vienna, December 1972. Vienna: International Atomic Energy Agency, 1973.

[2.17] Studsvik Instrument AB, S-611 82 Nykoping, Sweden. **2202D Datasheet**.

[2.18] Burgkhardt B., Fieg G., Klett A., Plewenia A. and Siebert B.R.L., The Neutron Fluence and H*(10) Response of the New LB 6411 REM Counter, **Rad. Prot. Dosim**., 70(1-4), 361, 1997.

[2.19] Naismith O.F. and Siebert B.R.L, A Database of Neutron Spectra, Instrument Response Functions, and Dosimetric Conversion Factors for Radiation Protection Applications, **Rad. Prot. Dosim.,** 70, 241-245, 1997.

[2.20] Mourgues M., Carossi J.C., Portal G., A Light Rem-counter of Advanced Technology, **Proc. 5th Symp. on Neutron Dosimetry**, Munich/Neuherberg, September 1984, EUR 9762 (Luxembourg:CEC) 1, 387, 1985.

[2.21] Hankins D.E., Problems of Practical Neutron Health Physics Monitoring, **Rad. Prot. Dosim**., 23(1-4), 488, 1988.

[2.22] Hunt J.B., Champlong P., Chemtob M., Kluge H. and Schwartz R.B., International Intercomparison of Neutron Survey Instrument Calibrations, **Rad. Prot. Dosim**., 27(2), 103, 1989.

[2.23] Aroua A., Boschung M., Cartier F., Gmür K., Grecescu M., Prêtre S., Valley J.F. and Wernli Ch., Study of the Response of Two Neutron Monitors in Different Neutron Fields, **Rad. Prot. Dosim**., 44, 183, 1992.

[2.24] Rimpler A., Dose Equivalent Response of Neutron Survey Meters for Several Neutron Fields, **Rad. Prot. Dosim**., 44, 189, 1992.

[2.25] Bartlett D.T., Tanner R.J. and Jones D.G., A New Design of Neutron Dose Equivalent Survey Instrument, **Rad. Prot. Dosim.,** 74(4), 267, 1997.

[2.26] Olsher R.H., Hsu H., Beverding A., Kleck J.H., Casson W.H., Vasilik D.G., Devine R.T., WENDI: An Improved Neutron Rem Meter, **Health Physics** 79(2), 170, 2000.

[2.27] Hsu H., Sun R.K., Monte Carlo Calculations of High-Energy Neutron Response for Improved Andersson Braun Remmeters, **Rad. Prot. Dosim**., 61, 167, 1995.

[2.28] Birattari C., Esposito A., Ferrari A., Pelliccioni M., Silari M., An Extended Range Neutron Rem Counter, **Nucl. Instrm. & Meths**., A297, 250, 1990.

[2.29] Birattari C., Esposito A., Ferrari A., Pelliccioni M., Rancati T., Silari M., The Extended Range Neutron Rem Counter LINUS: Overview and Latest Developments, **Rad. Prot. Dosim**., 76, 135, 1998.

[2.30] Jianping L., Yueli T., Shudong L., Ban L., Suzuki S., Iijima T., Nakamura H., Neutron Energy Response of a Modified Andersson-Braun Rem Counter, **Rad. Prot. Dosim**., 67, 179, 1996.

[2.31] Bartlett D.T., Bird T.V. and Miles J.C.H., **NRPB-R99 - The NRPB Nuclear Emulsion Dosemeter**, Didcot: National Radiological Protection Board, 1980.

[2.32] Bartlett D.T., Steele J.D., Tanner R.J., Gilvin P.J., Shaw P.V., Lavelle J., Ten years on: the NRPB PADC neutron personal monitoring service. **Rad. Prot. Dosim**., 70, 161, 1997.

[2.33] Jackson M. and French A.P., Analysis of Acceptance Testing Data for more than 800 sheets of CR-39 Plastic Assessed for the DRPS Approved Dosimetry Service, **Rad. Prot. Dosim**., 70, 139, 1997.

[2.34] Tanner R.J., Bartlett D.T., Steele J.D.. NRPB PADC neutron personal dosimetry after ICRP 60. **Nucl. Tracks Radiat. Meas**., 22, 703, 1993.

[2.35] Azmi-Garakani D., Energy response and linearity of electrochemically etched PADC. **Nucl. Tracks Radiat**. Meas., 22, 639, 1993.

[2.36] Harvey J.R., French A.P., Jackson M., Renouf M.C., Weeks A.R., An Automated Neutron Dosimetry System Based on the Chemical Etch of CR-39, **Rad. Prot. Dosim**., 70, 149, 1997.

[2.37] Barlow K., Jackson M., French A. and Harvey J.R., Application of Neutron Spectrometry in the DRPS Neutron Dosimetry Service, **Rad. Prot. Doism**., 70, 265, 1997.

[2.38] Gibson J.A.B. and Piesch E., **Neutron Monitoring for Radiological Protection, Technical Report Series Nos. 252**. Vienna: International Atomic Energy Authority, 1985.

[2.39] Piesch E. and Burgkhardt B., Albedo Dosimetry System for Routine Personnel Monitoring, **Rad. Prot. Dosim**., 23, 117, 1988.

[2.40] Burgkhardt B. and Piesch E., A Universal Beta/Gamma/Neutron Albedo Dosemeter for Personnel Monitoring, **Rad. Prot. Dosim**., 6, 281, 1983.

[2.41] Liu J.C. and Sims C.S., Characterisation of the Harshaw Albedo TLD and the Bubble Detector BD-100R and BDS-1500, **Rad. Prot. Dosim**., 32, 21, 1990.

[2.42] Liu J.C. and Sims C.S., Angular Response Performance Study of a New Harshaw Neutron Albedo TLD, **Rad. Prot. Dosim**., 30, 161, 1990

[2.43] Burgkhardt B. and Piesch E., Field Calibration Technique for Albedo Neutron Dosemeters, **Rad. Prot. Dosim**., 23, 121, 1988.

[2.44] Bartlett D.T., Tanner R.J. and Thomas D.J., Active Neutron Personal Dosemeters – A Review of Current Status, **Rad. Prot. Dosim**., 86, 107, 1999.

[2.45] Barthe J., Bordy J.M. and Lahaye T., Electronic Neutron Dosemeters : History and State of the Art, **Rad. Prot. Dosim**., 70, 59, 1997.

[2.46] Brody J.M., Barthe J., Boutruche B.and Segur, A New Proportional Counter for Individual Neutron Dosimetry, **Rad. Prot. Dosim**., 54, 369, 1994.

[2.47] Boutruche B., Bordy J.M., Barthe J., Segur P. and Portal G., A New Concept of a High Sensitivity Tissue Equivalent Proportional Counter for Individual Neutron Dosimetry. **Rad. Prot. Dosim**., 51, 335, 1994.

[2.48] Alberts W.G., Dietz E., Guldbakke S. and Kluge H., Response of an Electronic Personal Neutron Dosemeter, **Rad. Prot. Dosim**. 51, 207, 1994.

[2.49] Barelaud B., Paul D., Dubarry B., Mackovicka L., Decossas J.L. and Vareille J.C., Principles of an Electronic Dosemeter Using a PIPS Detector, **Rad. Prot. Dosim**. 44, 363, 1992.

[2.50] Apfel R.E., The Superheated Drop Detector, **Nucl. Instrm. Meths**., 162, 603, 1979.

[2.51] Ing H. and Birnboim H.C., A Bubble-damage Polymer Detector for Neutrons, **Nucl. Tracks Radiat. Meas**., 8, 285, 1984.

[2.52] d'Errico F., Alberts W.G. and Matzke M., Advances in Superheated Drop (Bubble) Detector Techniques, **Rad. Prot. Dosim**., 70, 103, 1997.

Chapter 3 Operational Neutron Energy Spectra

3.1 Operational Environment

During the development of the Active Area Neutron dosemeter (AAND) it was necessary to examine the typical operational environments encountered in the Naval Nuclear Propulsion Programme (NNPP). Security classification prohibits the use, in the open literature, of real neutron energy spectra that have been measured by various organisations within the submarine environment. Instead previously published spectra measured around pressurised water reactors (PWR) and boiling water reactors (BWR) were identified which may be considered as representative of the NNPP spectra.

3.1.1 Typical energy spectra

Four spectra measured by BAE Systems [3.1] collected in operational submarines were examined. Whilst no details may be provided these spectra were collected in locations where personnel could reasonably be expected to visit and work in. To allow selection of representative published spectra the following dosimetric parameters of each spectrum were determined; the mean energy, the effective radiation-weighting factor and the mean ambient dose equivalent. These parameters are defined in Equations 3.1,3.2 and 3.3 and the values given in Table 3.1.

$$\overline{E} = \frac{\int_{E_{min}}^{E_{max}} E\dot{\Phi}_E \, dE}{\int_{E_{min}}^{E_{max}} \dot{\Phi}_E \, dE}$$

Equation 3.1

$$\overline{wR} = \frac{\int_{E_{min}}^{E_{max}} wR(E)\dot{\Phi}_E \, dE}{\int_{E_{min}}^{E_{max}} \dot{\Phi}_E \, dE}$$

Equation 3.2

$$\overline{h^*(10)} = \frac{\int_{E_{min}}^{E_{max}} h^*(10)\dot{\Phi}_E \, dE}{\int_{E_{min}}^{E_{max}} \dot{\Phi}_E \, dE}$$

Equation 3.3

where,

$\overline{E}$ = mean energy

$\dot{\Phi}_E$ = neutron fluence rate at energy E

$\overline{wR}$ = mean radiation weighting factor

wR(E) = radiation weighting functions from ICRP60

$\overline{h^*(10)}$ = mean neutron fluence to ambient dose equivalent conversion coefficient

$h^*(10)$ = neutron fluence to ambient dose equivalent conversion coefficients

Table 3.1 Summary of dosimetric parameters of operational spectra

Spectra	Mean E (keV)	Mean w_R	Mean *h*(10)* pSv cm^2
Spectrum 1	53.7	7.25	38.8
Spectrum 2	29.8	6.45	27.8
Spectrum 3	275	11.7	117
Spectrum 4	141	8.15	58.7

As may be seen from Table 3.1 the four spectra are quite distinct. The mean energy varies by almost one order of magnitude amongst the four spectra, a similar range is also seen for the *h*(10)*. Although a smaller variation in the mean radiation-weighting factor w_R is seen it must be remembered that the possible range is only five to twenty. Therefore, it is not possible to represent the operational spectra by a single published spectrum. Instead it was proposed that published spectra be selected which approximate each of the four individual spectra.

In the last twenty-five years a considerable number of neutron spectra have been measured in and around nuclear facilities. The IAEA published a compilation [3.2] that contained most of the measurements made prior to 1982. In 1996 a new compilation incorporating both the IAEA compendium and more recent measurements was jointly prepared by the National Physical Laboratory and PTB [3.3, 3.4]. A PC based computer program SPKTBIB allows this catalogue to be interrogated to determine dosimetric and instrument response quantities.

There are approximately five hundred neutron spectra in this catalogue measured in many different environments. A sub-set of these were prepared using SPKTBIB's search function that included only measurements in and around PWR's and BWR's. This sub-set was inspected and any measurements of either bare fuel or transport containers were discarded. This yielded a set of around seventy potentially suitable spectra. The same three dosimetric parameters, as described above, were then calculated for these seventy spectra.

Spectra where then selected using the criterion such that each of the three dosimetric parameters should lie within ±10% of the operational spectra value. This led to a final set of eight spectra summarised in Table 3.2 and shown in Figures 3.1, 3.2, 3.3 and

3.4. These spectra are plotted as $E.\phi(E)$ versus the logarithm of energy i.e. the product of the energy E and the fluence rate per unit energy $\phi(E)$ versus the logarithm of the energy. Therefore, these figures effectively show the fluence rate per unit logarithmic energy interval.

Table 3.2 Summary of dosimetric quantities of representative spectra

Spectrum Description	SPKT BIB Index	Mean Energy (keV)	Mean wR	Mean h*(10) (pSv cm^2)
Czech PWR circulation pump room [3.7]	382	52.5	7.45	40.2
Swiss BWR 16m level [3.8]	472	53.6	7.53	36.7
Traws GCR BCD filter gallery [3.5]	303	32.3	6.77	29.8
Swiss BWR reactor level stairwell [3.8]	470	30.7	6.78	27.4
Caorso BWR inside reactor cavity [3.6]	339	282	13.9	141
Czech PWR reactor hall [3.7]	389	305	13.4	141
IAEA 318 PWR Loc. 81 [3.2]	80	142	8.34	61.6
Swiss BWR airlock into containment [3.8]	474	139	10.8	80.7

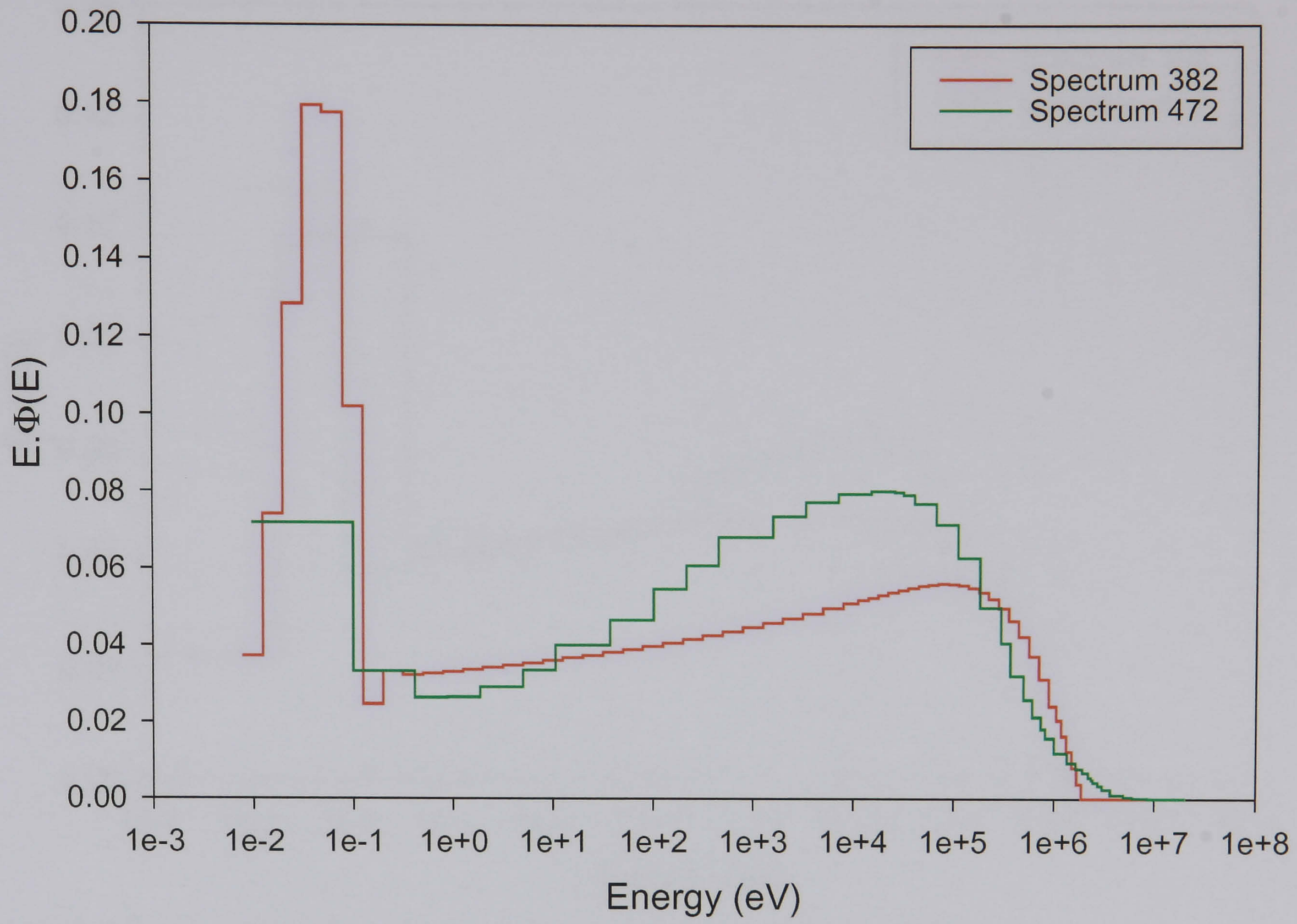

Figure 3.1 : Representative spectra for Spectrum 1

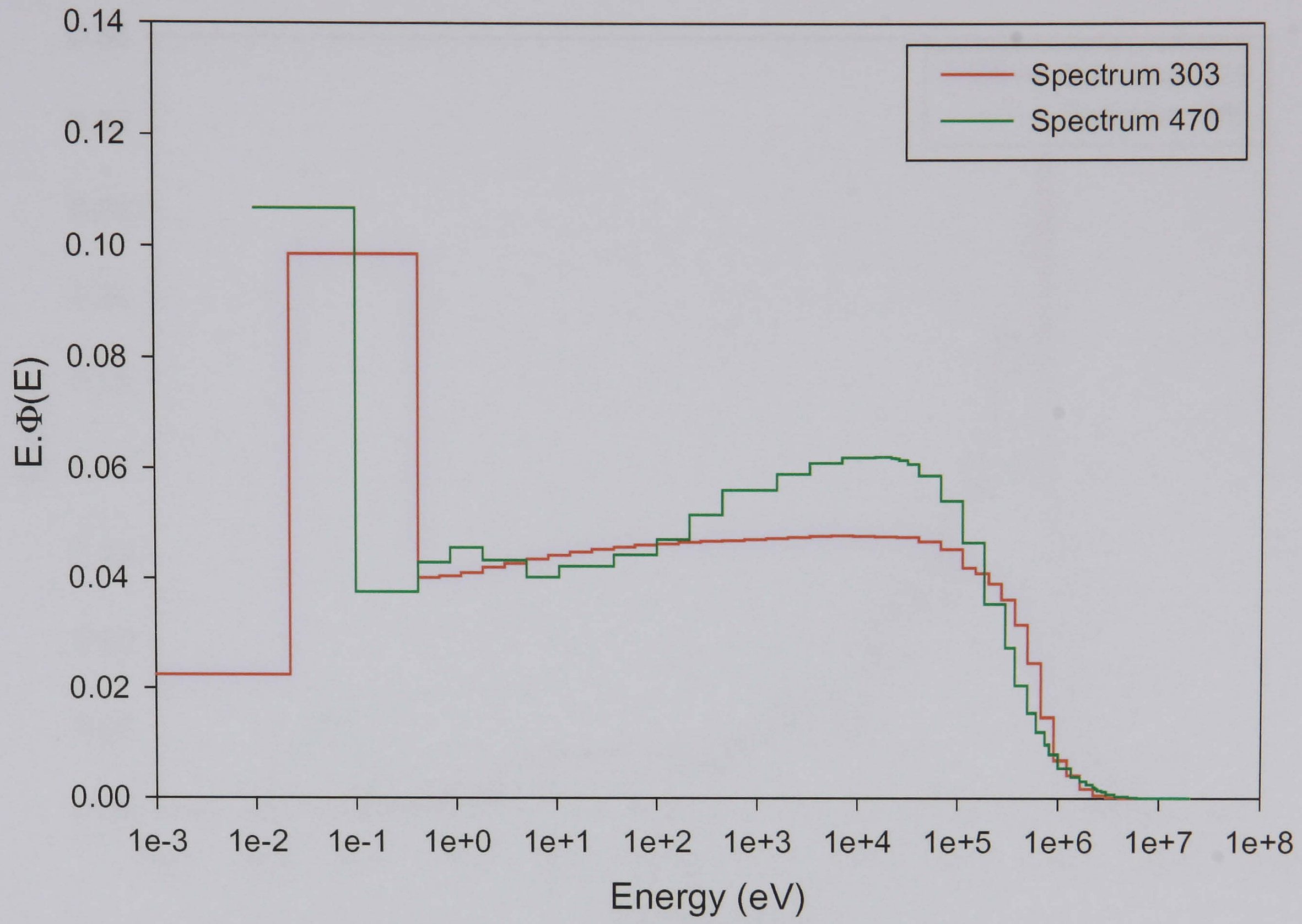

Figure 3.2 : Representative spectra for Spectrum 2

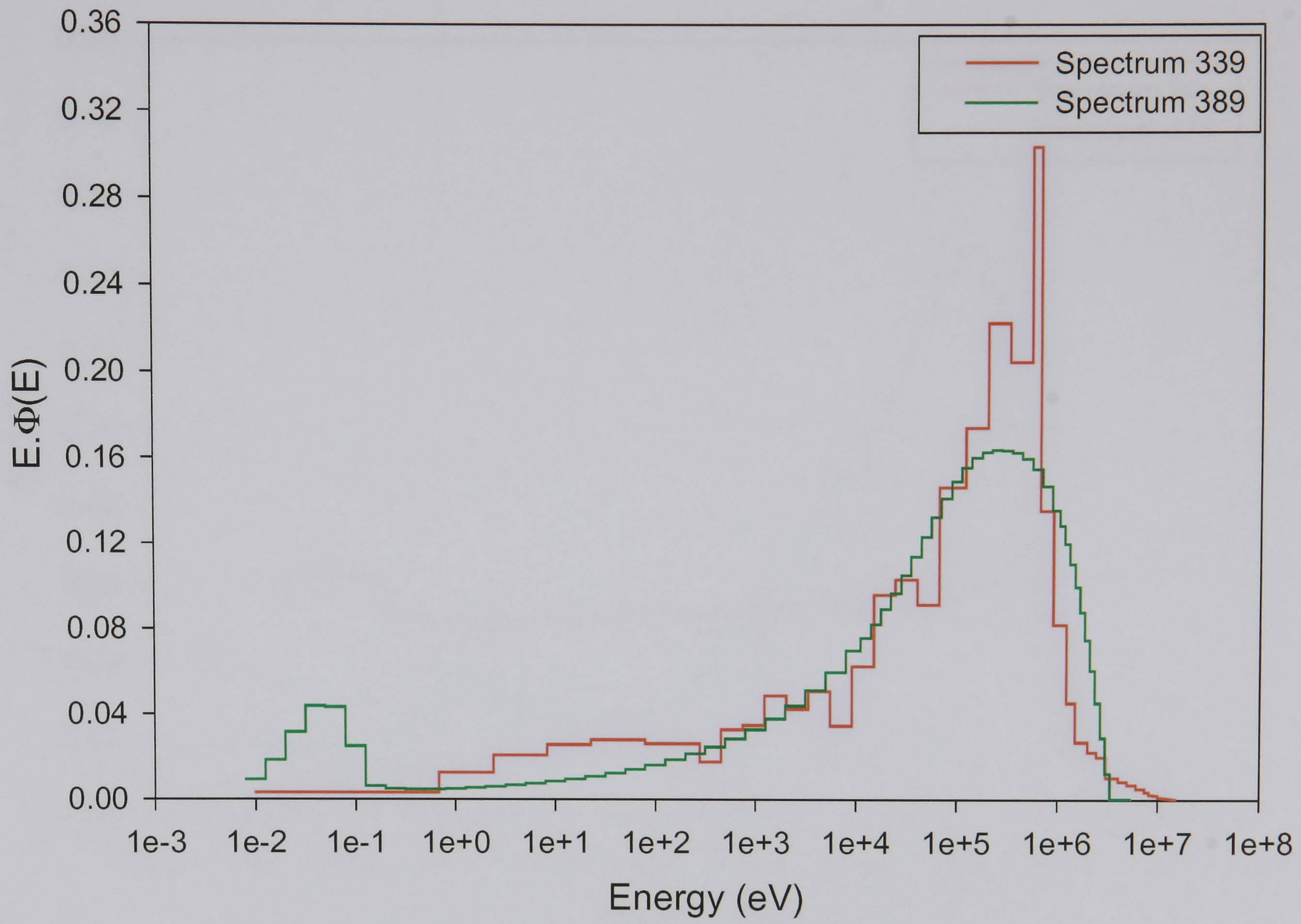

Figure 3.3 : Representative spectra for Spectrum 3

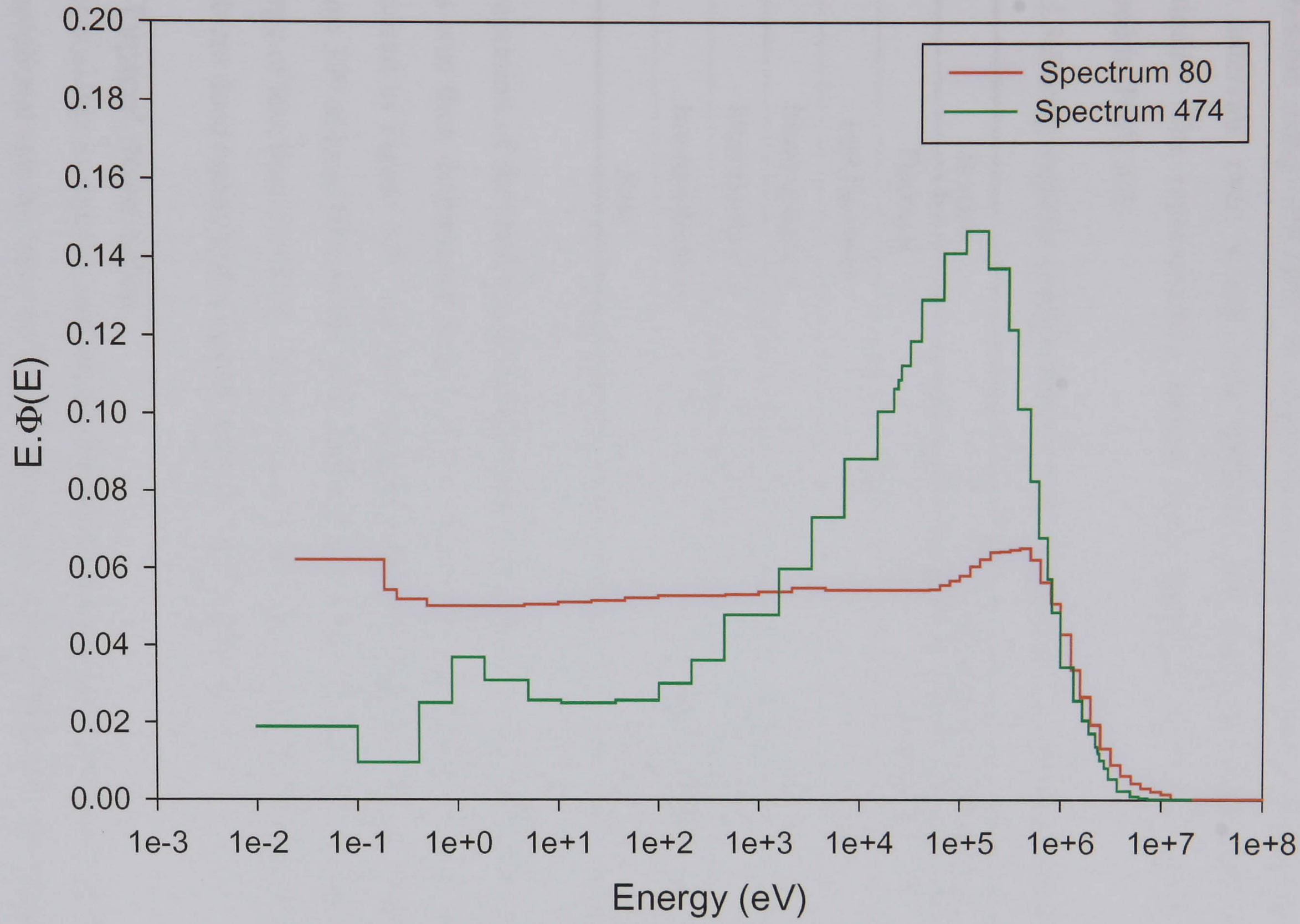

Figure 3.4 : Representative spectra for Spectrum 4

Having now identified a set of representative unclassified spectra the dosimetric characteristics of these spectra were investigated. It is well known that in operational spectra a considerable proportion of the total dose is due to relatively low energy neutrons [3.1]. In order to examine this for the representative spectra use was again made of SPKTBIB.

It is possible using SPKTBIB to subdivide the spectrum into a number of discrete energy intervals over which both detector and dosimetric quantities may be determined. The representative spectra were partioned into six energy regions, described in Table 3.3.

Table 3.3 Energy regions contributing to total mean ambient dose equivalent

Region	Energy interval (keV)
Thermal	$<5\times10^{-4}$
Epi-thermal	5×10^{-4} – 10
Intermediate 1	10 – 100
Intermediate 2	100 – 500
Intermediate 3	500 – 1000
Fast	> 1000

The proportion of the total mean ambient dose equivalent in each of these six energy regions was then determined for all of the representative spectra. These results are summarised in Figure 3.5. As may be seen from this figure with the exceptions of spectrum 339 at least 50% of the total ambient dose equivalent is due to neutrons with an energy of less than 500 keV. In the most extreme case, spectrum 470, over 45% of the ambient dose equivalent is due to neutrons below 100 keV

3.1.2 Typical dose rates

It is not possible to report exact values for the dose rates at the positions at which the four operational spectra were collected. However, it may reasonably be assumed that in all accessible areas dose rates in excess of 100 $\mu Sv\ h^{-1}$ are not normally encountered. Using the previously calculated mean ambient dose equivalent for each of the operational spectra the typical fluence rates will be in the range of 200 to 1000 $cm^{-2}\ s^{-1}$.

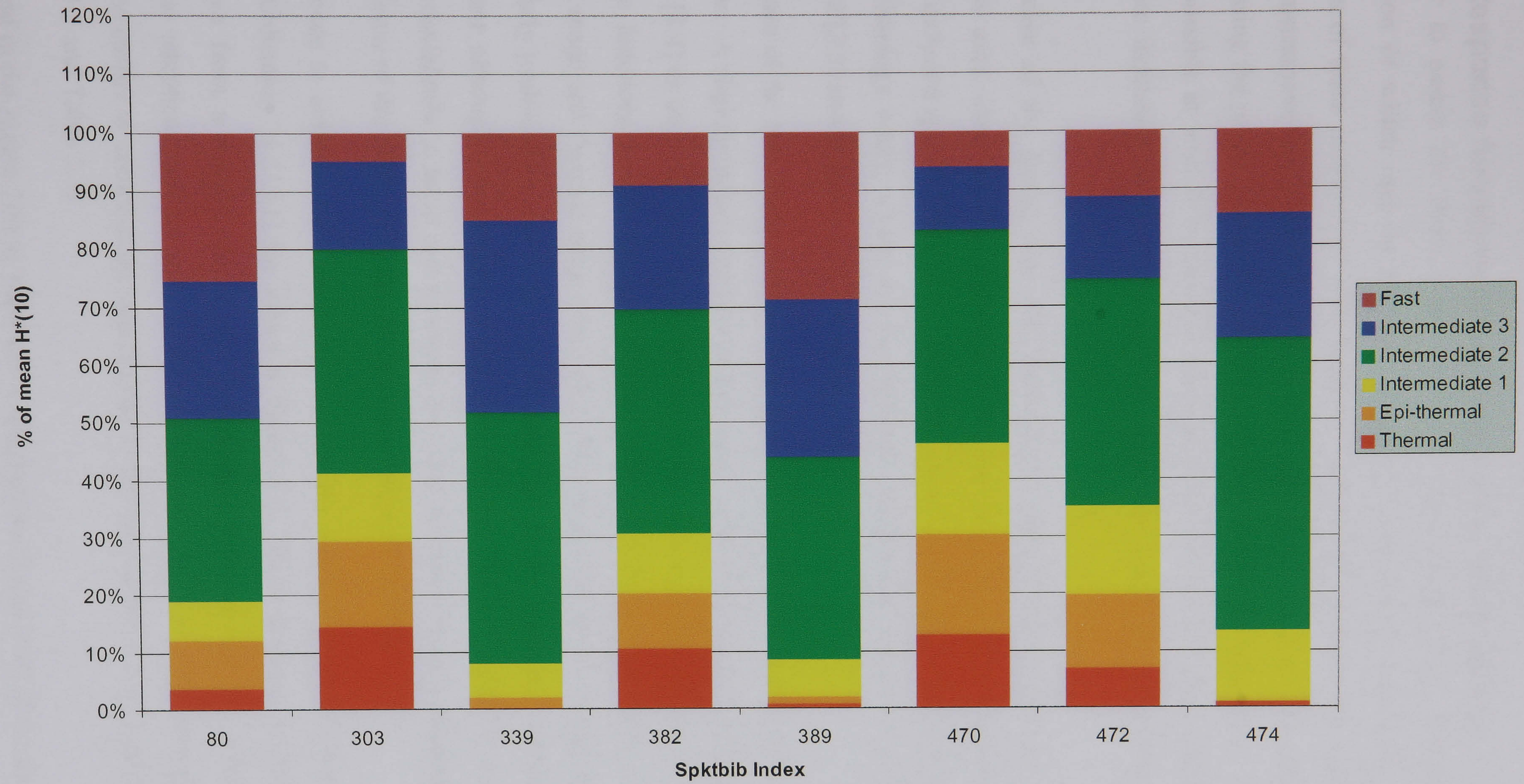

Figure 3.5 Contributions to mean ambient dose equivalent

3.2 Responses of Present Survey Instruments

3.2.1 Response functions of existing survey instruments

In order to assess the three most frequently encountered survey instruments, a description of which may be found in Chapter 2, the energy dependent response functions of these instruments were required. Response functions for a number of survey instruments are available from within SPKTBIB, however, no attempt was made during the production of the catalogue to evaluate the contributions. Therefore where possible at least two-response function were selected for each instrument so that some indication of the uncertaintities could be gained by comparing the two results.

In the case of the Leake type NE Technology Mark 7 NRM the two response functions used were those of Harrison [3.9] and the more recent measurement by Bartlett included in SPKTBIB [3.4]. Only one response function was available for the NE Technology NM2, whilst for the Studsvik 2202D two response functions by Delafield [3.5] and Nakamura [3.10] were used.

In the case of the two Mark 7 NRM responses good agreement is seen between both functions. A slightly higher response is indicated by the more recent measurements of Bartlett [3.4] in the 1 to 10 eV range but otherwise they are near equivalent. The two response functions for the Studsvik 2202D both suffer from poor detail in the epi-thermal range and thermal range (<0.5 eV). Measurements in this energy region are particularly problematic and large uncertainties are to be expected. Otherwise the agreement although substantially worse than for the Mark 7 NRM is reasonable. Further confidence in these two functions may also be drawn from a comparison with the response of the NM2, a similar design to the Studsvik 2202D.

The fluence to ambient dose equivalent conversion coefficients as recommended in ICRP Publication 74 [3.11] are shown in Figure 3.6. Some general conclusions may be drawn from a comparison of the instruments response and the ICRP74 data. Particular attention must be paid to the instruments response in the energy regions identified earlier as contributing significantly to the total ambient dose equivalent (see Figure 3.5 and Table 3.3)

In general in the region 100 to 1000 keV (intermediate 2 and 3) all of the instruments tend to slightly under-respond, whilst in the region 10 – 100 keV (intermediate 1) a

substantial over-response is seen, in the worse case of the Mark7 NRM by approximately nine fold. The NM2 and Studsvik 2202D show a smaller over-response in this region, typically three to four fold

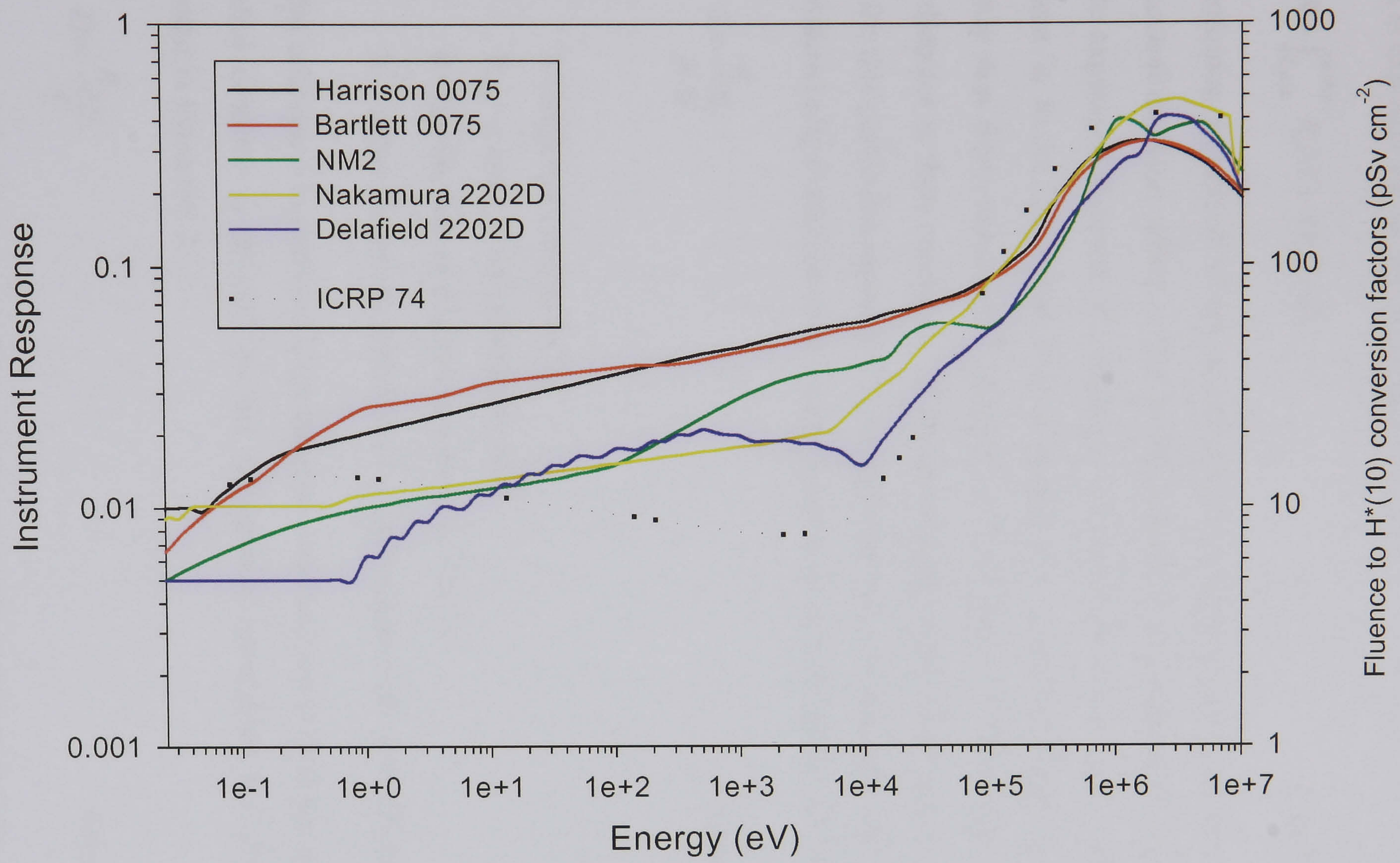

Figure 3.6 Area survey instrument responses and ICRP 74 data

3.2.2 Response of survey instruments in representative spectra

The response R of an area survey instrument depends on both its energy dependent response function $R_{\phi}(E)$, as shown in Figure 3.6, and also the neutron energy spectrum $\Phi(E)$, representative examples of which are shown in Figures 3.1 to 3.4, to which it is exposed and is shown in Equation 3.4.

$$R = \int_{E\min}^{E\max} R_{\phi}(E) \cdot \Phi(E)\, dE \qquad \textit{Equation 3.4}$$

It is a common feature of all the described survey instruments that they incorporate a single central detector, either a ^{3}He or BF_3 counter. The output of the instrument is therefore expressed in terms of counts per second from this counter. When a survey instrument is to be calibrated it is exposed to a known neutron spectrum, most commonly that from either an $^{241}Am/Be$ or ^{252}Cf source. The count rate from the central detector is then recorded. With knowledge of the fluence rate and the mean *h*(10)* for this particular neutron energy spectrum the response per unit dose rate may be determined often referred to as the response S, as represented in Equation 3.5.

$$S = \frac{R_{cal}}{\phi \cdot \overline{h^{*}}} \qquad \textit{Equation 3.5}$$

where,

S - response (counts Sv^{-1})

R_{cal} – counts s^{-1} in calibration field

ϕ - fluence rate at detector position (s^{-1} cm^{-2})

$\overline{h^{*}}$ - mean fluence to ambient dose equivalent coefficient (Sv cm^{2})

When the calibrated instrument is operated in some unknown field the count rate from the central detector is divided by the response to determine the dose rate *D*, as represented in Equation 3.6.

$$D = \frac{R_{field}}{S} \qquad \textit{Equation 3.6}$$

If it is assumed that the energy dependent instrument response *R(E)* is a perfect fit to the recommend fluence to ambient dose equivalent conversion coefficients then the instrument will correctly display ambient dose equivalent. However, as has previously been described real area survey instruments do not precisely match these factors, in fact they both over and under-respond. Therefore, if there is any difference

between the energy spectrum of the calibration field and the operational spectrum the instrument will not provide an accurate measurement of ambient dose equivalent.

Prior to considering the response of existing survey instruments to representative fields the typical energy spectra in which they are calibrated must be examined. the spectrum of ^{241}Am/Be and ^{252}Cf taken from the ISO standard [3.12] are shown in Figure 3.7 also tabulated in Table 3.4 are the dosimetric parameters for each spectrum.

Table 3.4 Summary of dosimetric parameters of calibration spectra

Source	Mean E (keV)	Mean wR	Mean h*(10) pSv cm^2
^{241}Am/Be	4154	13.99	391
^{252}Cf	2129	17.54	384
Mean value of all spectra in Table 3.2	130	9.37	69.8

If these values are compared with those in Table 3.2 for representative spectra it is clear that both of these calibration spectra are considerably different from the typical operational spectrum. In fact operational spectra have a much lower mean energy and therefore it is likely that as the existing survey instruments over-respond in this region that they will tend to over-estimate the ambient dose equivalent.

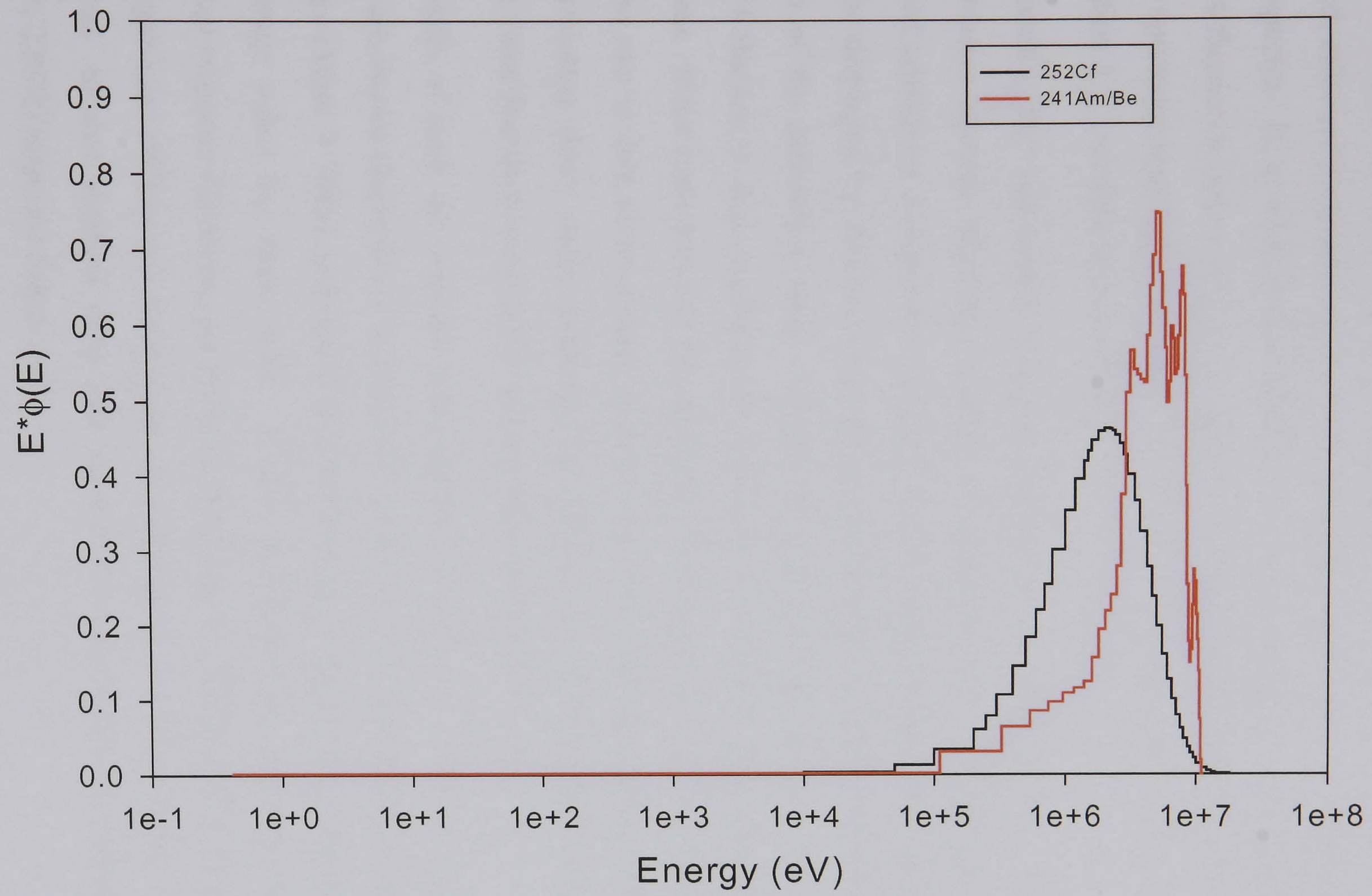

Figure 3.7 : Calibration spectra

To investigate the likely over-response of the existing survey instruments in representative fields use was again made of SPKTBIB. By using this program it is possible to prepare a response function block that contains the six previously described energy dependent response functions. These response functions may then be folded, effectively calculating R_{cal} in Equation 3.4, with the two calibration neutron energy spectra. If, as well as this folding, the energy spectra are also folded with the ICRP 74 fluence to dose conversion coefficients then the true ambient dose equivalent for that spectrum may be calculated. The survey instrument sensitivity S, as defined in Equation 3.5, can then be determined.

Subsequently, the instrument response functions are then folded with the nine representative spectra described earlier to calculate R_{field}. Using the previously calculated sensitivity S, Equation 3.6 may then be used to calculate the dose rate that would be displayed by that particular survey instrument had it been calibrated in one or other of the calibration fields. Again the representative spectra are folded with ICRP 74 fluence to dose conversion coefficients to determine the true ambient dose equivalent. If the ratio between the calculated 'displayed' dose rate and the calculated true dose rate is then taken a value greater than unity indicates that the instrument is over-estimating dose, unity indicates that instrument is correctly estimating dose whilst a value less than unity indicates an under-estimation of dose.

The results of such an exercise using either ^{241}Am/Be or ^{252}Cf as the calibration spectra are shown respectively in Figures 3.8 and 3.9. For clarity where two response functions (Mark 7 NRM and Studsvik 2202D) were available for a given instrument the average value has been used. It was interesting to note that although the individual response functions, particularly in the case of the Studsvik 2202D, showed some significant differences these were not reflected in the final results. The ratio of 'displayed' to true ambient dose rate agreed to better than 7% between the two Studsvik 2202D response functions.

As may be seen from both figures, the Mark 7 NRM will tend to over-estimate dose when either calibrated with ^{241}Am/Be or ^{252}Cf. Using a ^{252}Cf source as opposed to ^{241}Am/Be reduces the over-estimation; this is to be expected as the mean energy of ^{252}Cf is considerably lower than that of ^{241}Am/Be. However, as both of the calibration

spectra are considerably harder than any of the representative spectra the effect of changing the calibration source is quite small. In the case of very soft spectral groups, e.g. those equivalent to spectrum 1 and spectrum 2 this over-estimation may be as large as 200% for both a ^{252}Cf and ^{241}Am/Be calibration. Even in the case of the two harder spectral groups dose rate is still over-estimated by approximately a 50%.

Both the NM2 and the Studsvik 2202D show similar responses. Again the effect of the two different calibration spectra is quite small. For the two very soft spectral groups, the NM2 will again tend to over-estimate the dose rate, typically by 20%, whilst for these groups the Studsvik 2202D will tend to slightly under-estimate dose rate. When operated in the two harder spectral groups dose-rate is either correctly displayed or slightly under-estimated, typically by 20% or better

In the light of these results it was concluded that the cylindrical design of the Studsvik 2202D or the NM2 was better suited to the typical operational energy spectra encountered. However, the under-estimates of ambient dose equivalent in some of the spectra are a cause for concern. Whilst it may be argued that from a radiation protection principle that over-estimation of dose, even by a significant amount, is acceptable the under-estimation cannot be justified. Therefore, it was concluded that although a cylindrical design would be a suitable basis for the development of a new area survey instrument particular attention must be paid to ensure that dose rates are not under-estimated.

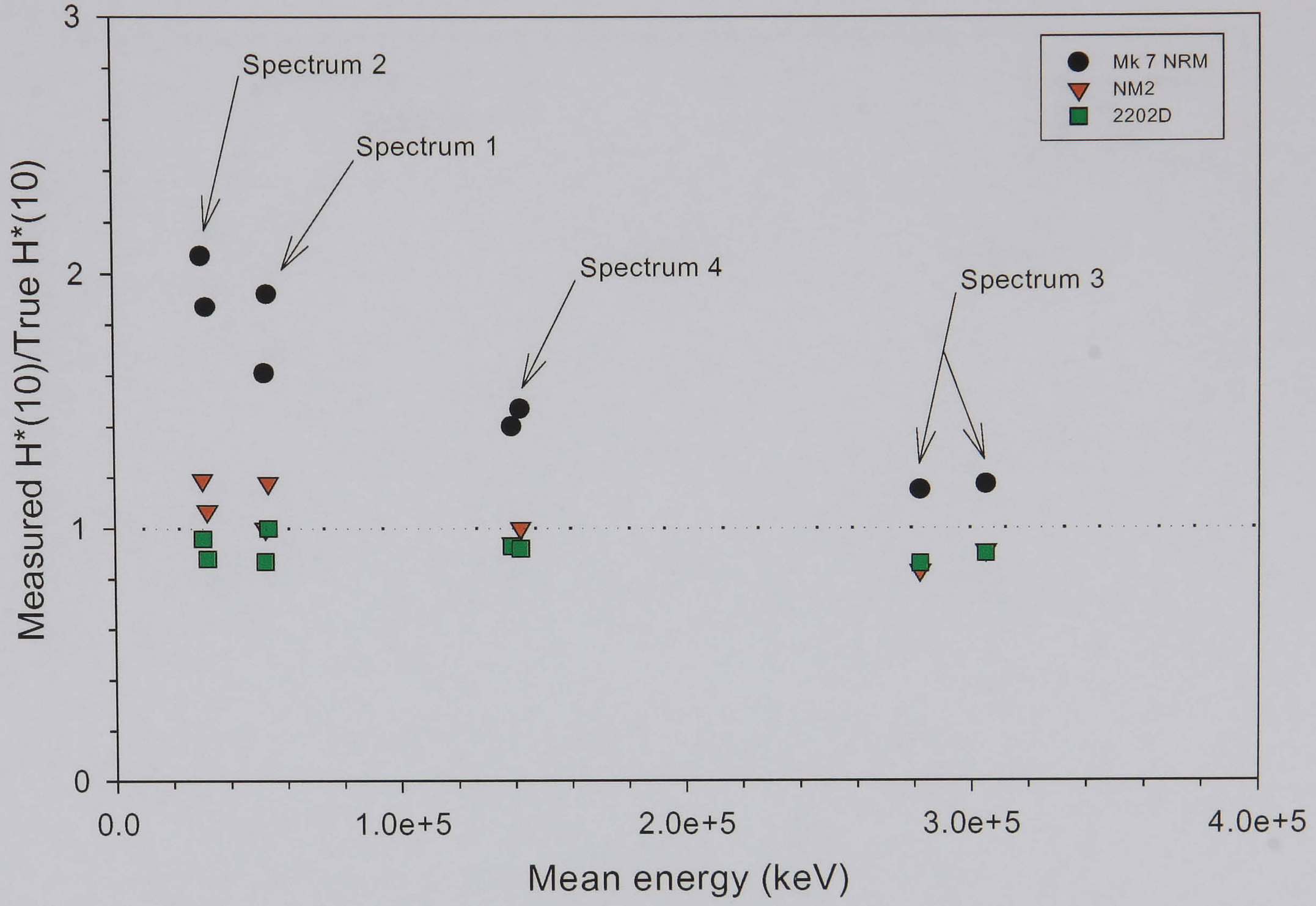

Figure 3.8 : Survey instrument response to representative spectra

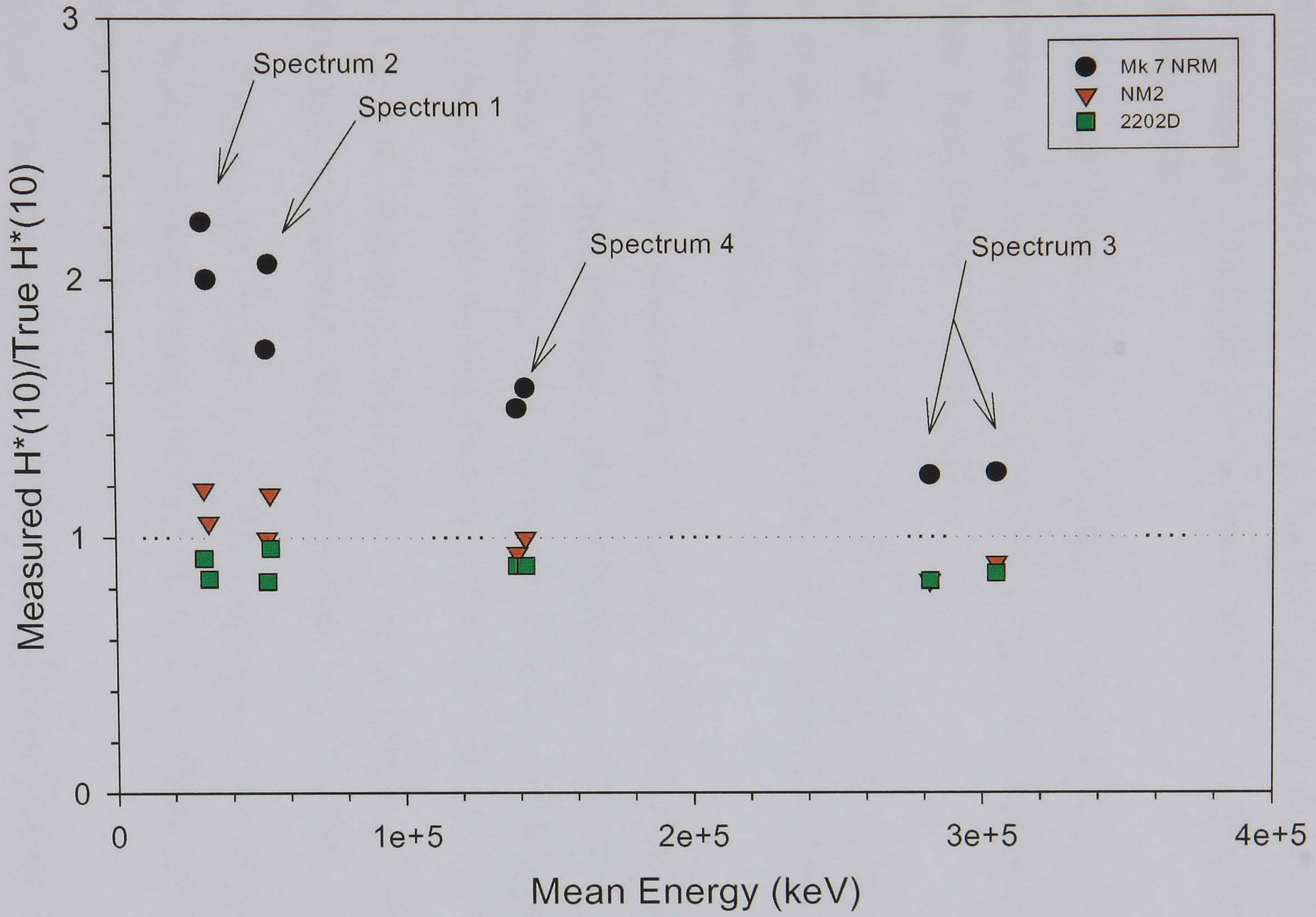

Figure 3.9 : Survey instrument response to representative spectra

3.4 References for Chapter 3

[3.1] Roskell J. (BAE Systems Barrow) Private communication

[3.2] Griffith R.V., Palfalvi J. and Madhvanath U., Compendium of Neutron Spectra and Detector Responses for Radiation Protection Purposes, **IAEA Technical Report Series Nos. 318**. Vienna: International Atomic Energy Agency, 1990.

[3.3] Naismith O.F. and Siebert B.R.L., **NPL Report CIRA(EXT)005 - Manual for SPKTBIB: a PC-based Catalogue of Neutron Spectra**,. Teddington: National Physical Laboratory, 1996.

[3.4] Naismith O.F. and Siebert B.R.L., A Database of Neutron Spectra, Instrument Response Functions, and Dosimetric Conversion Factors for Radiation Protection Applications, **Rad. Prot. Dosim**. 70, 241, 1997.

[3.5] Delafield H.J. and Perks C.A., Neutron spectrometry and dosimetry measurements made at nuclear power stations with derived dosemeter responses, **Rad. Prot. Dosim**. 44, 227, 1992.

[3.6] Barbucci P., Mariotti G., **Neutron spectral analysis of the Caorso BWR cavity and sacrificial shield penetrations and comparison with the irradiation experiment results, Advances in Reactor Physics, Mathematics and Computation. Volume 1**. Paris: Societe Francaise d'Energie Nucleaire, 1987.

[3.7] Sujak P., Carny P., Prouza Z., Hermanska J., Energy Spectra of Stray Neutron Fields at PWR Nuclear Power Plants, **Rad. Prot. Dosim**., 19, 179, 1987.

[3.8] Aroua A., Grecescu M., Valley J.F., Characterisation of the Mixed Neutron-Gamma Fields Inside the Swiss Nulcear Power Plants by Different Active Systems, **Rad. Prot. Dosim**., 51, 17, 1994.

[3.9] Harrison K.G., The Response of A Spherical neutron Survey Meter, **Nucl. Instr. & Meths**. 166, 197, 1979.

[3.10] Nakamura T., Hayashi K., Takahashi A., Torii A., Uwamino Y., Veda M., Neutron skyshine from intense 14-MeV neutron source facility, **Nucl. Sci. & Eng**. 90, 281, 1985.

[3.11] International Commission on Radiological Protection Publication 74, **Conversion Coefficients for use in Radiological Protection against External Radiation**. Oxford: Pergamon Press, 1996.

[3.12] British Standards Institution, **ISO 8529**. London: BSi Publications, 1998.

Chapter 4 Semiconductor Memory Devices

4.1 Semiconductor Devices

Previous studies have focused on the use of semiconductor devices such as Static and Dynamic Random Access Memories (sRAMs and dRAMs) [4.1, 4.2, 4.3], Charge Coupled Devices (CCDs) [4.4], Charge Injection Devices (CIDs) [4.5], Gallium Arsenide diodes (GaAs) [4.2] and silicon pn junction diodes PINs [4.6]. The mechanism of detection in all cases is the charge deposited within the sensitive region of the device by the secondary high LET particles produced by neutron radiation. In the case of high-energy neutrons, the secondary particles are the recoil protons produced within a hydrogenous converter. Thermal neutrons require a charged particle converter, such as lithium or boron that produce an alpha particle through the (n,α) reaction, the (n,p) reaction in 3He is impractical as no solid ^{3}He compound exists.

Prior work by Darambara [4.3, 4.7] had indicated that the phenomenon of Single Event Upsets (SEUs) in dRAMs was a potential mechanism through which thermal neutrons could be detected.

4.1.1 Mechanism of Neutron Detection in dRAMs

The phenomena of alpha particle induced (Single Event Upset) SEUs in dRAMs, where a SEU is defined as a "random, nonrecurring, single bit error", was first reported by May [4.8] in 1979. However, in 1980 Cerofolini [4.9] proposed the use of a dRAM as an alpha particle detector. The potential for neutron detection using a dRAM was described by Davis in 1985 [4.10] and again by Lund et al in 1986 [4.11].

In order to understand the mechanism of SEU it is necessary to understand the operation of a dRAM. A random access memory device is an integrated circuit that allows the storage and retrieval of data in a binary form. The memory is arranged in a matrix form with 2^{a} columns and 2^{b} rows, so giving the device a total storage capacity of 2^{a+b} bits. The columns are referred to as bit lines whilst the rows are referred to as word lines.

To read or write data to a particular storage cell, known as addressing, the word (row) address is first specified. This will select an entire word (row) of the storage matrix.

Subsequently the bit (column) address is specified, this will select a particular bit of the previously specified word.

Obviously the key component of such a memory device is the storage cell itself. It is at this point that two distinct classes of RAM may be identified. If the storage cell is arranged so that the data is non-volatile (i.e. no further action is required once the logic state of the storage cell has been set) then these devices are described a static RAMs. Alternatively if the data is volatile they are referred to as dynamic RAMs. The most commonly encountered sRAM storage cell is a bistable flip-flop circuit; data is stored by selecting the storage location and then driving the bistable to the required logic state 1 or 0. Dynamic RAMs almost exclusively use a capacitor as their storage cell. A schematic of a typical dram storage cell is shown in Figure 4.1.

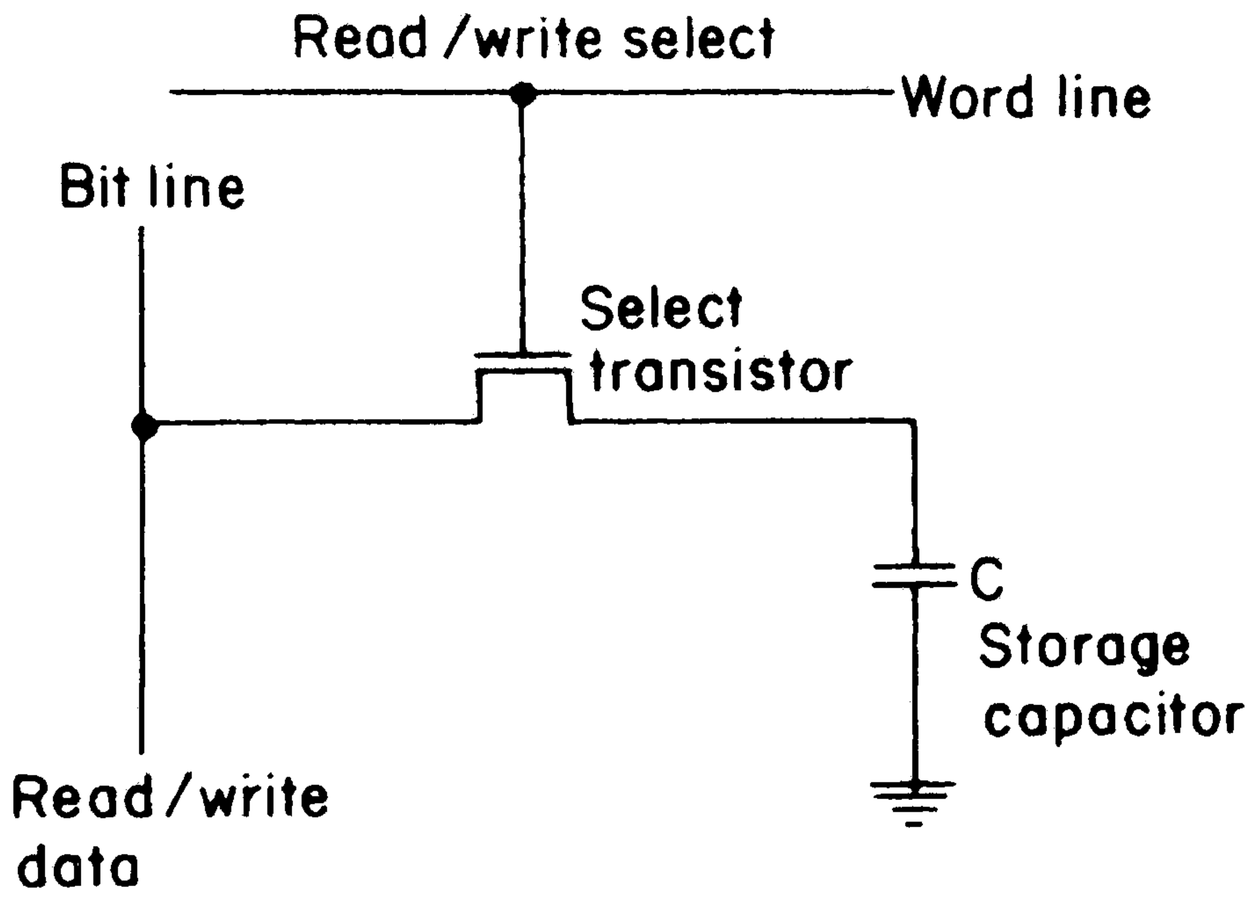

Figure 4.1 Schematic of a typical dram storage cell from [4.12]

The storage cell consists of two elements, a switching transistor T and a storage capacitor C. Transistor T is arranged such that its source is connected to the bit line, the drain to the storage capacitor and its gate to the word (row) line. Therefore, when the word address W is first specified all 2^b storage cells on the W^{th} row will have a voltage applied to the transistor T. This will switch the source to drain path to a conducting state. The data stored in the storage cell corresponding to the required bit address B can then be addressed by connecting to the B^{th} bit line.

The logic state, data, of each storage cell is stored by the presence or absence of a charge in the storage capacitor C, conventionally absence indicates logic 1 whilst presence indicates 0. To read or write data to a particular cell a means is necessary to transfer charge in and out of the capacitor and also to determine the charge stored in

the capacitor. This is achieved by a circuit know as a sense amplifier. This is a bi-directional circuit which when its sense input is connected to the appropriate bit line can in the case of a read operation transfer the stored charge from the storage capacitor via the bit line and then compare this charge with a reference storage cell to determine the logic state i.e. presence or absence of charge of that particular storage cell. In a write operation the sense amplifier can either charge or discharge the capacitor depending on the input logic state. The output of the charge comparator is fed via a buffer to the output pins of the device whilst the input to the sense amplifier is connected, again via a buffer, to the input data pins of the device.

Unfortunately the simple design of the storage cell introduces an additional consideration in dRAM operation. In the case of a read operation as the capacitance of the bit line/sense amplifier is considerably greater than the storage capacitor when the charge stored is transferred, the logic state of the cell is essentially lost. Therefore, immediately after the read operation the logic state of the storage cell must be re-stored. Additionally, due to charge leakage from the storage capacitor over time the data stored would become corrupted. The periodic re-writing of the stored data is referred to as refreshing.

Dynamic RAMs incorporate a dedicated circuit that is responsible for periodic refreshing each storage location; the minimum time between the refreshing of an individual storage cell is primarily controlled by the rate of charge leakage from the storage capacitor.

Modern dRAMs are fabricated using the well known technologies of Very Large Scale Integration (VLSI), the details of which are well described in Prince [4.12] and Sze [4.13]. Essentially, by a process of lithography, ion implantation and chemical vapour deposition regions of either silicon both p and n-type and silicon dioxide are formed on a silicon wafer substrate. When considering the SEU phenomenon the key feature is the size and hence capacitance of the storage capacitor so formed.

Early dRAMs such as Philips [4.14] 4k device produced in 1973 had a cell size of 864 μm^2, later devices such as the Intel 16k device [4.15] had a cell size of 455 μm^2. By this point an effective industry standard had arisen in which the individual circuits comprising the dRAM where arranged in a planar fashion across the device surface. This planar architecture remained up to an including the 1 Mb devices. Advances in

fabrication technology eventually allowed cell sizes as small as 40 μm^2 to be used in the 1 Mb device [4.12]. After this point subsequent (4 and 16 Mb) devices used more complicated two dimensional architectures to further reduce cell size, particularly important was the trend to bury the storage capacitor beneath the switching transistor, the so called trench architecture.

A SEU will occur if an ionising particle deposits sufficient energy to alter the logic state of a storage cell. In the case of a dRAM primarily by depositing charge in the region of the storage capacitor however it is possible that charge may be deposited in the region of the bit lines and sense amplifiers. It is possible to estimate the minimum charge deposition Q_{crit} necessary to disturb the logic state of a storage capacitor if a number of assumptions are made. Firstly that a typical 1 Mb dRAM has a storage capacitance of C_{cell} 50 fF [4.12] and operates with a + 5 volt supply V_{op}. It is also assumed that the sense amplifier will consider a logic 0 to be represented by a charge in the range Q_{max} - $Q_{max}/2$ and a logic 1 in the range $Q_{max}/2$ – 0, where Q_{max} is the maximum charge stored and is given by Equation 4.1. This range of values will allow for the gradual leakage of charge out of the capacitor. Therefore if at least $Q_{max}/2$ is deposited into the storage capacitor the logic state can be altered from 1 to 0, it is immediately apparent that a 0 to 1 transition is not possible as the deposition of additional charge will not affect a logic 0 state as the cell is already above the critical threshold $Q_{max}/2$

$$Q_{\max} = C_{cell} \bullet V_{op} \qquad \textit{Equation 4.1}$$

$$Q_{crit} = \frac{Q_{\max}}{2} \qquad \textit{Equation 4.2}$$

With these assumptions the critical charge is 1.25×10^{-13} coulomb. This charge corresponds to the production of 7.8×10^5 electrons. In silicon at room temperature the generation of 1 electron-hole pair requires 3.62 eV [4.16] energy. Therefore, if an incident ionising particle deposits at least 1.4 MeV of energy in the region of the capacitor its state will be altered.

Even allowing for the attenuating effect of various passivation layers, which are commonly applied to the devices surface, this amount of energy deposition is certainly within the range achievable from alpha particles. In fact the occurrence of SEU, first reported by May [4.8] in 1979, was attributed to energy deposition by alpha

particles emitted by uranium and thorium impurities in the ceramic material forming the dRAM packaging.

4.2 Modelling of the Converter

If the occurrence of SEU in semiconductor memory devices is to be used as the basis of a neutron dosemeter it is necessary that the incident neutrons be converted to charged particles. The conversion to charged particles can be addressed in two ways. For low energy neutrons use will be made of the high cross section (n,α) reactions of either ^{6}Li or ^{10}B, whilst for fast neutrons the conversion can either be directly to recoil protons produced in a hydrogenous material or by moderation and then (n,α) conversion.

Modelling of the converter has focused on an (n,α) converter, as this conversion mechanism is applicable to both low energy and, following moderation, to fast neutrons. The objective of this modelling is to optimise the choice of converter material and its thickness. The parameter to be maximised is the total alpha particle fluence rate exiting the converter with sufficient energy to cause a SEU.

The total SEU causing alpha particle fluence rate $\dot{\Phi}_{\alpha}$ exiting the converter is given by Equation 4.3.

$$\dot{\Phi}_{\alpha} = \frac{A\rho\theta N_a \sigma_{\alpha}^{Li}}{M_a} \int_o^t z\dot{\Phi}_n(z) P(z \rightarrow t) dz \qquad \textit{Equation 4.3}$$

where, σ_{α}^{Li} - microscopic cross section considering only ^{6}Li(n,α) reaction

A - surface area of converter

ρ - density of converter film

N_a - Avogardro's constant

M_a - Atomic mass of converter compound

θ - number of ^{6}Li atoms per molecule of converter compound

$\dot{\Phi}_n(z)$ - neutron fluence rate at a depth z through converter

$P(z \rightarrow t)$ - Probability that an alpha particle produced at a depth z exits the converter with sufficient energy to cause a SEU

t - thickness of converter

The terms $\dot{\Phi}_n(z)$ and $P(z \rightarrow t)$ have each been examined and an expression for them proposed. Considering first the neutron fluence rate through the converter, this term was first [4.17] modelled by a 'simple' thermal neutron only diffusion theory model.

Later a more realistic modelling of the converter was undertaken using the Monte Carlo code MCNP.

The following discussion is restricted to lithium-based converters. Whilst the $^{10}B(n,\alpha)$ reaction has a higher cross section, 3746 barn compared to 924 barn, the resulting alpha particle has a lower energy of 1471 keV versus ^{6}Li's 2055 keV. Previous work [4.3, 4.7] has focused on lithium compound converters since the alpha particle from $^{10}B(n,\alpha)$ would not have been sufficiently energetic to cause a SEU in the device under study at that time. Furthermore, only three lithium compounds were considered lithium carbonate, lithium hydroxide and lithium fluoride. This selection was made on two grounds, firstly the other commercially available lithium compounds are chemically unstable and secondly, and more importantly, the compounds are commercially available enriched to at least 95% atom ^{6}Li.

4.2.1 Diffusion theory model of thermal neutron fluence rate through the converter

The neutron fluence rate through a lithium compound converter has previously been described by Equation 44 [4.17].

$$\dot{\Phi}(z) = \dot{\Phi}_0 e^{-\Sigma_c^{Li} z} \qquad \textit{Equation 4.4}$$

where, Σ^{Li}_c = macroscopic cross-section considering *only* ^{6}Li (n,α) ^{3}H

The objection to this expression is that it assumes the converter may be modelled using the formalisms of neutron diffusion theory. A requirement for this is that the system must be large compared to the mean free path (m.f.p) of neutrons within it and that the medium is not strongly absorbing i.e. the ratio of the macroscopic absorption Σ_A to total Σ_T cross section should be small. Neither of these conditions are satisfied by the converter, it is by design both small compared to the m.f.p and strongly absorbing. Macroscopic cross sections were calculated (see Table 4.1) using the 'method of mixtures' where ;

$$\Sigma = \frac{N_A \rho}{A_W} \sum_{all\, i} F_i \sigma_i \qquad \textit{Equation 4.5}$$

where ,
ρ - compound density
A_W - compound atomic weight
F_i - fractional abundance of i^{th} isotope
σ_i - microscopic cross section of i^{th} element

However, the use of diffusion theory does allow a "simple" model to be produced that does not rely on Monte Carlo simulations. Rather than reject this model and solely rely on simulations a number of revisions were made.

Table 4.1 - Cross section data for converters

Compound	Σ_T - cm^{-1}	Σ_A - cm^{-1}	Σ_S - cm^{-1}	m.f.p - cm
Li_2CO_3 - enr	5.211	5.157	5.415×10^{-2}	0.1919
Li_2CO_3 - nat	0.4522	0.3977	5.443×10^{-2}	2.211
LiOH - enr	11.60	11.16	0.4393	8.621×10^{-2}
LiOH - nat	1.280	0.8531	0.4266	0.7813
LiF - enr	27.95	27.81	0.1421	3.5878×10^{-2}
LiF - nat	2.268	2.123	0.1456	0.4409

Note : (1) Cross section data was extracted from the ENDFB6 compilation [4.18]

(2) Atomic weights and densities were taken from the CRC Handbook 81st Edition [4.19]

(3) *Enr* - refers to lithium enriched to 95% (atom) ^{6}Li : *Nat* - refers to natural isotopic lithium 7.5% (atom) ^{6}Li

By using Σ^{Li}_c as the characteristic constant no account is made for competing absorption reactions. However, the proposed compounds of lithium do not contain other significantly absorbing isotopes, all other compounded isotopes have total absorption cross-sections of less than 0.4 barn. In comparison with the 924.6 barn cross section of $^6Li(n,\alpha)^3H$ competing absorption reactions will have a small effect and be of most significance in natural lithium compounds.

Scattering is known [4.20] to be anisotropic in the laboratory frame of reference for low energy neutrons in light elements. The anisotropy can be described by the term $\bar{\mu}_0$, the average cosine of the scattering angle per collision in the laboratory frame. $\bar{\mu}_0 = 0$ indicates a perfect isotropic angular distribution whilst $\bar{\mu}_0 > 0$ indicates anisotropy.

$$\bar{\mu}_0 = \frac{\sum_{all\,i} F_i \sigma_{i,s} \left(2/3A_i\right)}{\sum_{all\,i} F_i \sigma_{i,s}} \qquad \textit{Equation 4.6}$$

where, $\sigma_{i,s}$ – scattering cross section of i^{th} isotope
A_i – atomic weight of i^{th} isotope
F_i – atom fraction of i^{th} isotope

Compounds containing hydrogen are expected to show the most significant deviation from isotropic scattering, calculations of $\bar{\mu}_0$ support this expectation. For all compounds other than LiOH $\bar{\mu}_0$<0.06 whilst for enriched ^{6}LiOH $\bar{\mu}_0 = 0.5777$.

Therefore the neutron fluence rate through the converter has been modelled by a more rigorous application of diffusion theory. The two characteristics constants are now the diffusion constant D and the diffusion length L. When calculating L it is not possible to use the well-known expressions [4.21] as these are only valid in the case where Σ_A / Σ_T is small; clearly not the case for our converters. Instead, use was made of the expression given by Price and Horton [4.20] for L in media where Σ_A / Σ_T is not small i.e. strongly absorbing media. The value of L is the positive root of Equation 4.7 shown below. The values of L for the compounds of interest are shown below in Table 4.2.

$$\frac{L\Sigma_S}{2}\ln\left(\frac{L\Sigma_T+1}{L\Sigma_T-1}\right)=\frac{1+3L^2\Sigma_S\Sigma_A\bar{\mu}_0}{1+3L^2\Sigma_T\Sigma_A\bar{\mu}_0} \qquad \textit{Equation 4.7}$$

Table 4.2 – Diffusion model constants

Compound	Σ_S / Σ_T	Σ_A / Σ_T	L - cm
Li_2CO_3 - enr	1.039×10^{-2}	0.9896	20.51
Li_2CO_3 - nat	1.204×10^{-1}	0.8795	182.8
LiOH - enr	3.787×10^{-2}	0.9621	2.220
LiOH - nat	3.333×10^{-1}	0.6665	21.00
LiF - enr	5.084×10^{-3}	0.9950	3.978
LiF - nat	6.420×10^{-2}	0.9361	48.50

The neutron fluence rate through the converter is now approximated by Equation 4.8 [4.20].

$$\dot{\Phi}(z)=\dot{\Phi}_0 e^{-z/L} \qquad \textit{Equation 4.8}$$

4.2.2 MCNP model

Whilst use has been made of diffusion theory its applicability is simple and limited, the converter is both thin compared to the mean free path and $\Sigma_A / \Sigma_T \approx 1$.

Furthermore, the previous model considered only thermal neutrons. In light of these reservations it was decided that no attempt would be made to extend the model to account for moderation or epi-thermal, intermediate energy neutron reactions. Instead use was made of Monte Carlo simulations undertaken using MCNP4b [4.22].

A 5 μm thick converter onto which were incident thermal neutrons generated from a planar source located at the origin was considered. The neutron fluence rate was tallied by means of surface crossing tallies at intervals throughout the converter. Two objectives were set for this model, firstly to identify any potential convergence or stability problems and secondly to compare with the results of the diffusion theory model.

Initially no attempts were made at variance reduction and the model was ran for 10^6 incident neutrons (requiring an approximate run time of 120 minutes). On inspection the tallies all had unacceptably high relative errors (MCNP documentation recommends only accepting tallies if the relative error is less than 0.01) and most showed non-random behaviour in the history probability density function (p.d.f) indicating poor convergence due to un-sampled histories.

An extensive series of tests of various variance reduction strategies was then undertaken. Most obvious of these was to angle bias the source in the forward direction whilst 'killing' all neutrons generated with directions away from the converter. This greatly improved the tally statistics but at the cost of a marginal increase in run time. Traditional techniques such as importance mapping, forced collisions and partial deterministic transport (DXTRAN spheres) all failed to significantly improve on this result, and so as to retain simplicity in the model were discounted.

MCNP by default treats capture events implicitly, at a capture event the neutron is not 'killed' but instead its scoring weight is appropriately reduced and transport continues. In highly absorbing media repeated captures treated implicitly leads to considerable processor time being spent transporting very low weight neutrons which contribute little to the tally. Therefore, implicit capture was disabled and all capture events are now analogue. This considerably improved both the relative error and convergence.

Despite the improvements achieved in relative error the small variations in fluence rate expected through the converter require that very low relative errors are achieved and long runs were therefore required (t > 900 minutes).

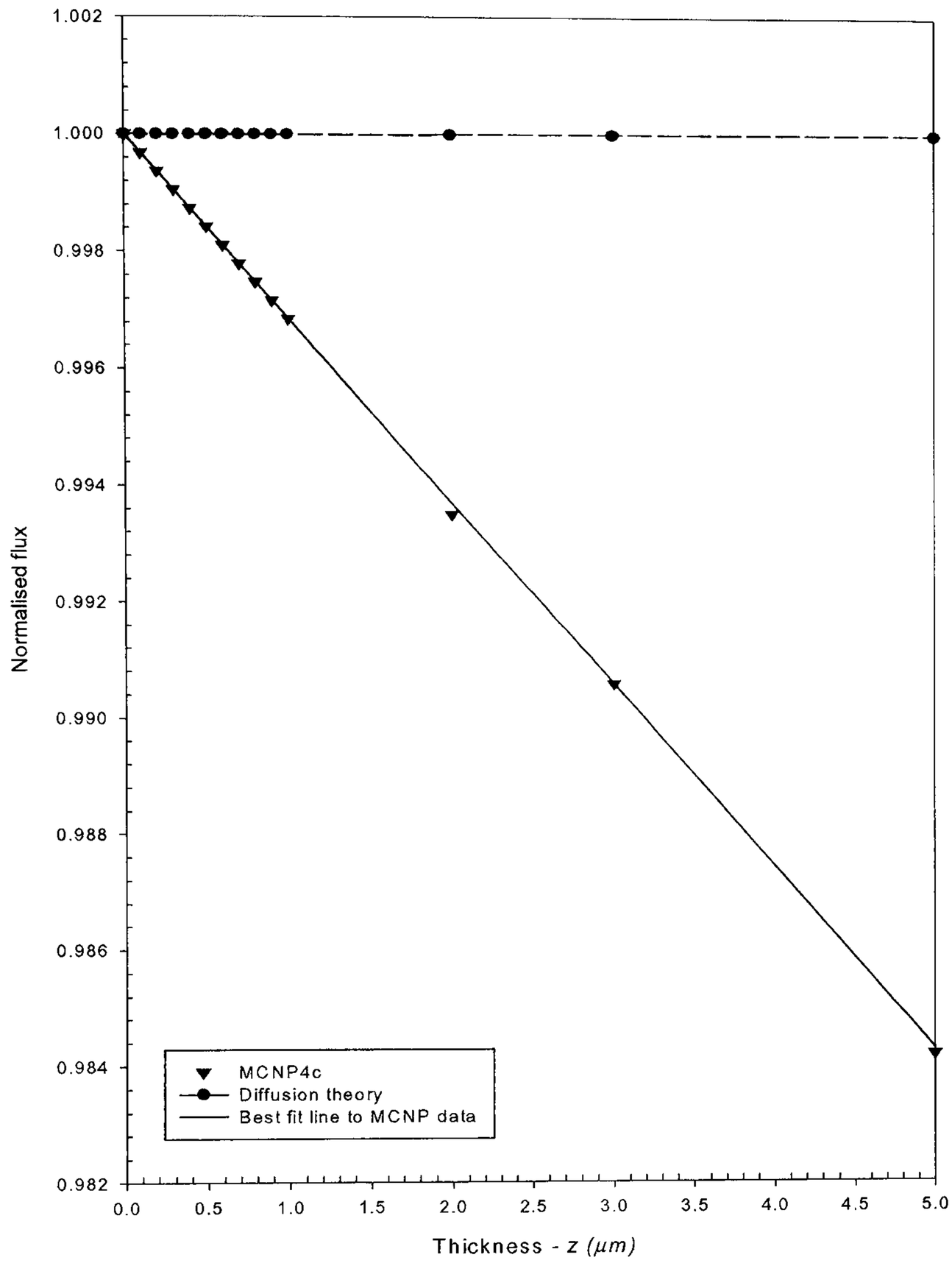

Figure 4.2 Comparison MCNP simulations with diffusion theory model

A plot comparing the MCNP simulations with that predicted by the earlier diffusion model for the case of enriched lithium carbonate is shown in Figure 4.2. It is immediately apparent from Figure 4.2 that the neutron fluence rate is inadequately modelled by diffusion theory. An essentially constant fluence rate is predicted yet MCNP simulations confirm this is not the case. This confirms the belief that the small size and highly absorbing nature of the converters render the converters unsuitable for analysis by diffusion theory. A similar result was observed for the other converter compounds in both the enriched and natural state.

Re-plotting the MCNP results on a natural logarithmic scale suggested that the profile could be described by an equation of the form shown below.

$$\dot{\Phi}(z) = \dot{\Phi}_0 e^{-zc} \qquad \textit{Equation 4.9}$$

A curve of the form of Equation 4.9 was fitted to the MCNP results using a least squares method, solid line in Figure 4.2, and yielded the following value for the constant c, see Table 4.3.

Table 4.3 – MCNP fitted values

Compound	C – cm^{-1}
Li_2CO_3 - enr	31.5 ± 0.4
Li_2CO_3 - nat	2.62 ± 0.06
LiOH - enr	36.3 ± 0.3
LiOH - nat	3.04 ± 0.06
LiF - enr	38.4 ± 0.3
LiF - nat	3.20 ± 0.05

4.2.3 Alpha Particle Transmission - SRIM Simulations

An exponential function has been used to express $P(z \rightarrow t)$, probability that an alpha particle produced at a depth z exits the converter with sufficient energy to cause a SEU [4.17]. Whilst this leads to an expression that may easily be integrated, it is not a physically realistic description. Mono-energetic alpha particles have high and equal, for a particular initial energy, Linear Energy Transfer (LET) rates and so unlike photons they all suffer almost identical stopping hence they have a well-defined range.

Therefore, this exponential function was replaced with a more realistic expression for $P(z \rightarrow t)$. This function is the result of fitting the two-parameter step function (Equation 4.10) to the results of Monte Carlo simulations of alpha particles transported through various thicknesses of converter compounds.

$$P(z \rightarrow t) = \frac{1}{\left[1+\left(\frac{z}{a}\right)^{b}\right]} \qquad \textit{Equation 4.10}$$

The Monte Carlo code SRIM [4.23] was obtained and this has been used to perform the transport simulations. SRIM was used to transport 50 000 normally incident alpha particles (requiring an approximate run time of 45 minutes) through thickness of lithium compounds in the range 0.1 to 10μm. The incident alpha particles were assumed to be produced by the $^{6}Li(n,\alpha)$ reaction and so had an initial energy of 2055 keV, the threshold energy was set at 1950 keV. This threshold energy was selected as it had previously been established as the alpha particle SEU threshold energy for 16 Kbit Texas Instrument dRAMs [4.17] and so would allow comparison with previous work.

The code option to produce an output file of all transmitted particles was enabled, amongst other tallies this output file records the particles residual energy. A FORTRAN 90 program was written to read this file and tally the total number of incident alphas N_{TOT}, their average energy and the total number above some threshold energy N_{THR}. The value of $P(z \rightarrow t)$ was then calculated as,

$$P(z \rightarrow t) = \frac{N_{THR}}{N_{TOT}} \qquad \textit{Equation 4.11}$$

A plot of $P(z \rightarrow t)$ versus z for enriched 95% $^{6}Li_2CO_3$, together with the fitted curve of the form Equation 4.10 is shown in Figure 4.3.

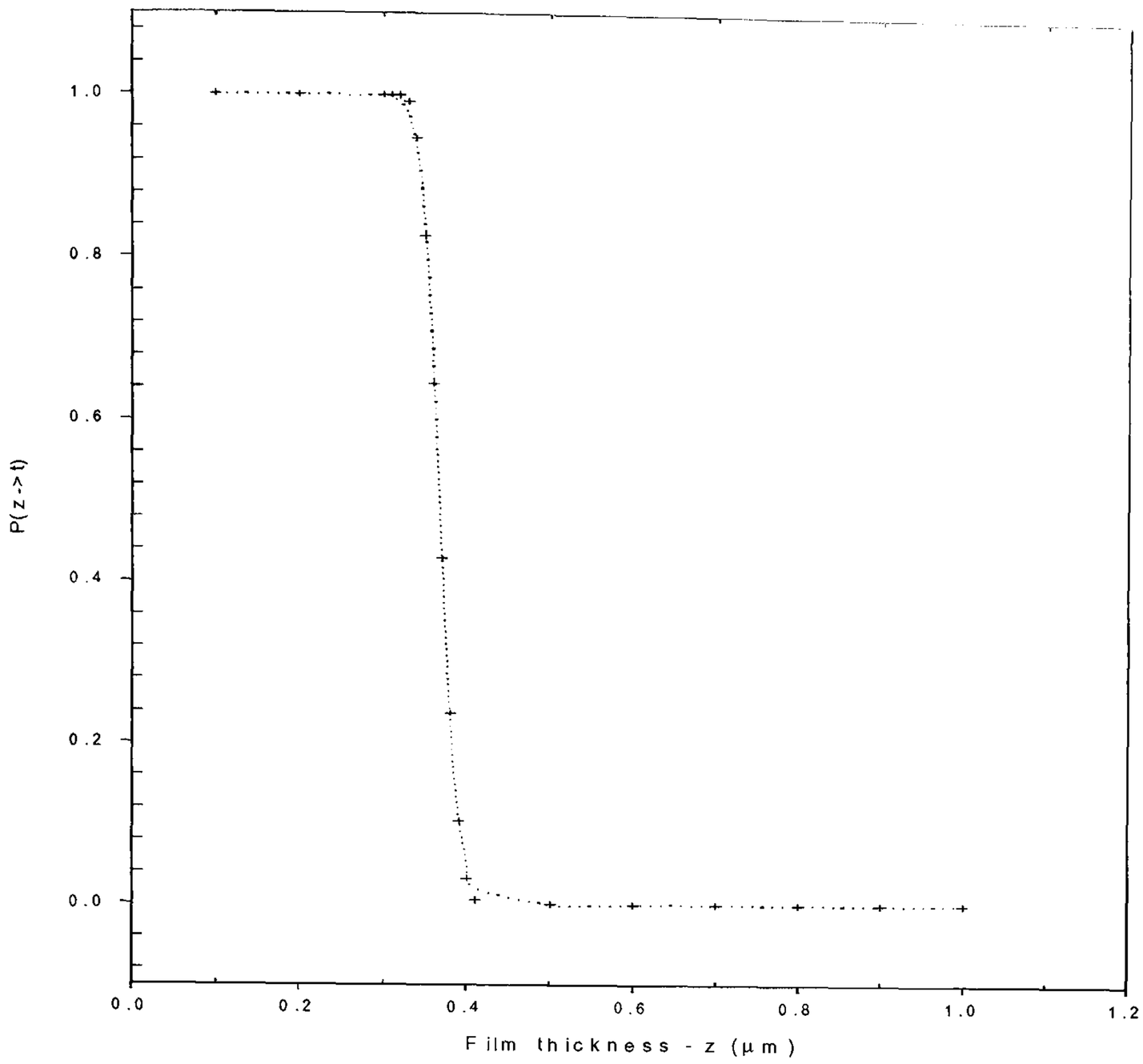

Figure 4.3 - $P(z \rightarrow t)$ versus z for enriched Li_2CO_3

The values of a and b for various enriched lithium compounds are tabulated below in Table 4.4. Its is believed that as the nuclear component of the stopping power is small compared to the atomic component the difference between natural and isotopically enriched lithium compounds will not be significant. This observation is supported by the results for all three lithium compounds which show no significant difference (the two sets of *a* and *b* differ by less than the standard error at 2σ associated with them) in the final values of *a* and *b*.

Table 4.4 - Fitting parameters of Equation 4.10 to experimental $P(z \rightarrow t)$ values

Compound	a - µm	b
Li_2CO_3 - enr	0.3668 ± 0.0004	34.9 ± 1.2
Li_2CO_3 - nat	0.3775 ± 0.0009	34.1 ± 1.5
LiOH - enr	0.4770 ± 0.0005	36.0 ± 1.1
LiOH - nat	0.4824 ± 0.0007	36.2 ± 1.4
LiF - enr	0.3118 ± 0.0004	34.5 ± 1.2
LiF - nat	0.3201 ± 0.0006	34.2 ± 1.3

The choice of the fitting function was not entirely arbitrary, the constants a and b have a physical interpretation. Of most relevance is the value of a this may be interpreted as the thickness of converter at which 50% of the incident alpha particles exit with an energy greater than the chosen threshold i.e. $P(z \rightarrow t) = 0.5$. The constant b can be regarded as proportional to the final energy straggling in the transmitted alpha, low b indicates large straggle.

4.2.4 Converter sensitivity

All the terms required in Equation 4.3 are now available and are stated explicitly in Equation 4.12 and are summarised in Table 4.5 below.

$$\dot{\Phi}_{\alpha} = \frac{A\rho\theta N_a \sigma_{\alpha}^{Li}}{M_a} \int_o^t z\dot{\Phi}_0 e^{-zc} \frac{1}{\left[1+\left(\frac{z}{a}\right)^b\right]} dz \qquad \textit{Equation 4.12}$$

Table 4.5 - Summary of constants used in equation 4.12

Compound	a – cm	b	c - cm^{-1}
Li_2CO_3 - enr	$(3.668 \pm 0.004) \times 10^{-5}$	34.9 ± 1.2	31.5 ± 0.4
Li_2CO_3 - nat	$(3.775 \pm 0.009) \times 10^{-5}$	34.1 ± 1.5	2.62 ± 0.06
LiOH - enr	$(4.770 \pm 0.005) \times 10^{-5}$	36.0 ± 1.1	36.3 ± 0.3
LiOH - nat	$(4.824 \pm 0.007) \times 10^{-5}$	36.2 ± 1.4	3.04 ± 0.06
LiF - enr	$(3.118 \pm 0.004) \times 10^{-5}$	34.5 ± 1.2	38.4 ± 0.3
LiF - nat	$(3.201 \pm 0.004) \times 10^{-5}$	34.2 ± 1.3	3.20 ± 0.05

It is however not the absolute value of $\dot{\Phi}_{\alpha}$ that is required but the value of t at which $\dot{\Phi}_{\alpha}$ is at maximum. The maximum will occur when $\frac{d}{dt}\left[\dot{\Phi}_{\alpha}\right] = 0$, therefore,

$$\frac{d}{dt}\left[\frac{A\rho\theta N_a\sigma_\alpha^{Li}}{M_a}\int_o^t z\dot{\Phi}_0 e^{-zc}\frac{1}{\left(1+\frac{z}{a}\right)^b}dz\right]=0$$

Equation 4.13

So let f(z) = $\frac{A\rho\theta N_a\sigma_\alpha^{Li}}{M_a} z\dot{\Phi}_0 e^{-zc}\frac{1}{\left(1+\frac{z}{a}\right)^b}$

now $F(z)=\int f(z)dz \Rightarrow f(z)=\frac{d}{dz}F(z)$

hence $\int_0^t f(z)dz=F(z)_0^t=F(t)-F(0)$

therefore, $\frac{d}{dt}\left[\int_0^t f(z)dz\right]=\frac{d}{dt}\left[F(t)-F(a)\right]=f(t)-f(0)$

hence,

$$\frac{d}{dt}\left[\frac{A\rho\theta N_a\sigma_\alpha^{Li}}{M_a}\int_o^t z\dot{\Phi}_0 e^{-zc}\frac{1}{\left(1+\frac{z}{a}\right)^b}dz\right]=\frac{A\rho\theta N_a\sigma_\alpha^{Li}}{M_a}\dot{\Phi}_0 te^{-tc}\frac{1}{\left(1+\left(\frac{t}{a}\right)^b\right)}$$

Equation 4.14

Equation 4.14 can only be set equal to zero if *t* is infinite or zero, suggesting that there is no physical value of *t* that optimises the converter. However, this observation is misleading as is apparent if the term describing the alpha particle transmission probability P(z→t) is examined in comparison with the physical phenomena it is modelling. This term is attempting to algebraically model the transmission of alpha particles and whilst it adequately describes the behaviour for thicknesses comparable with the alpha particle range it fails for large *z*. If *z* is many times the range physically no alpha particles will be transmitted P(z→t) = 0 but the above expression will not produce a zero for P(z→t) but instead a very small but finite value i.e. for a value of $t=10a$ and $b=34.75$ (the average value of all compounds listed in Table 4.3) this term equals 1.8×10^{-35} rather than the physical zero.

Therefore, to investigate the variation of SEU causing alpha particle fluence rate with converter thickness Equation 4.12 was numerically integrated for a range of *t*. This numerical integration was performed using the program MACSYMA. In this program it is possible to set a lower limit which when a numerical variable falls below the variable is set equal to zero (the constant epsilon). By enabling this option it was possible to force P(z→t) to zero for large *t* and so realistically model the physical situation.

Equation 4.12 was integrated for *t* in the range 0 to 5 μm with ϕ_0 set to 1 and a converter surface area in 1 cm^2. The value $\dot{\Phi}_\alpha$ resulting therefore represents the SEU causing alpha particle fluence rate normalised to 1 neutron cm^{-2} and so can be thought of as a sensitivity. The results of this integration are shown in Figure 4.4. Summarised in Table 4.6 are the efficiencies of each particular converter.

It is clear that enriched lithium hydroxide represents the most efficient converter and that provided a minimum thickness of at least 1 μm is achieved the converter efficiency is not affected by variation in the converter thickness.

Table 4.6 - Summary of detection efficiencies of converters

Compound	% of incident neutrons converted to SEU causing alpha particle
Li_2CO_3 - enr	2.1 ± 0.1
Li_2CO_3 - nat	0.17 ± 0.03
LiOH - enr	3.8 ± 0.2
LiOH - nat	0.30 ± 0.02
LiF - enr	2.2 ± 0.1
LiF - nat	0.17 ± 0.03

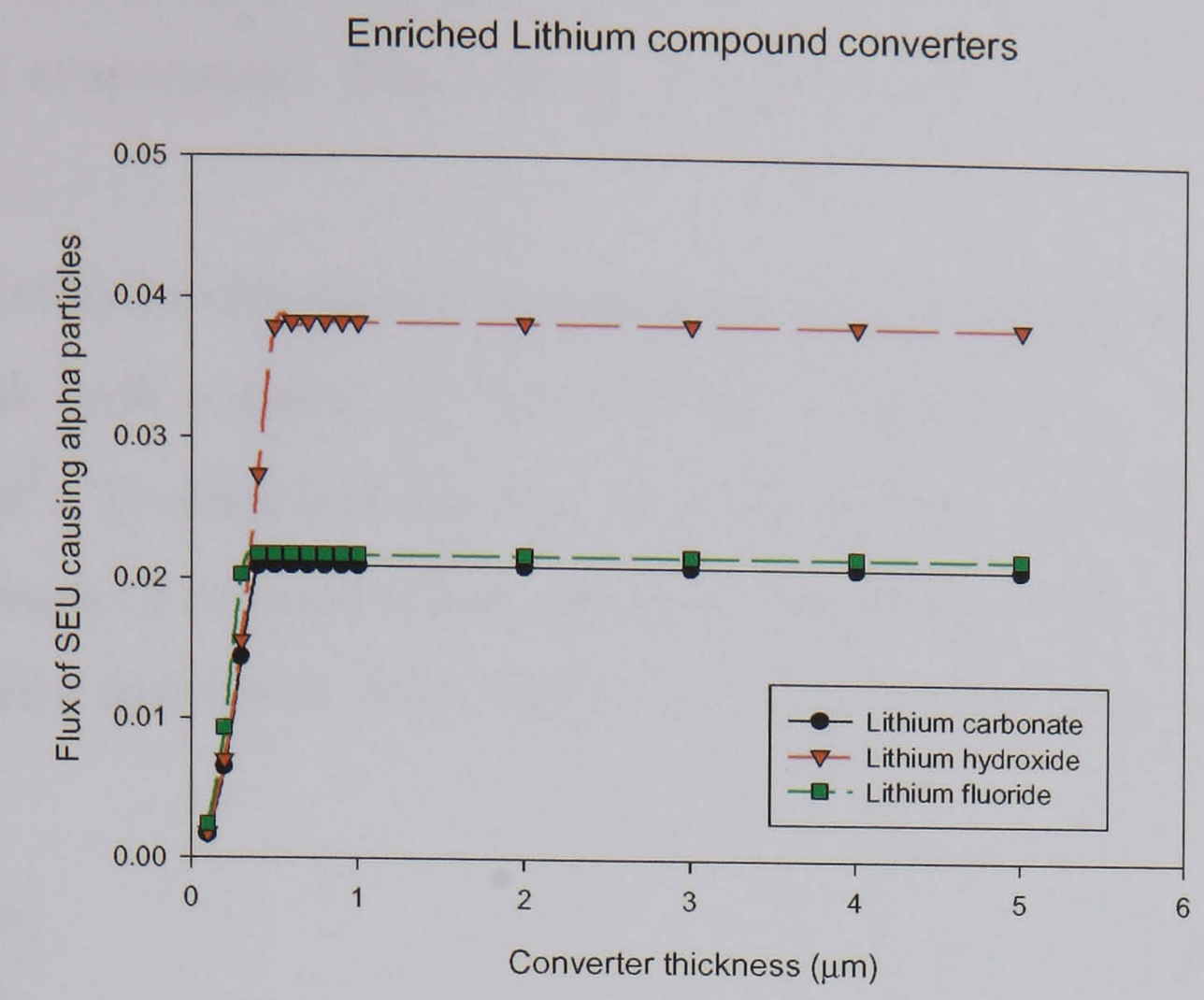

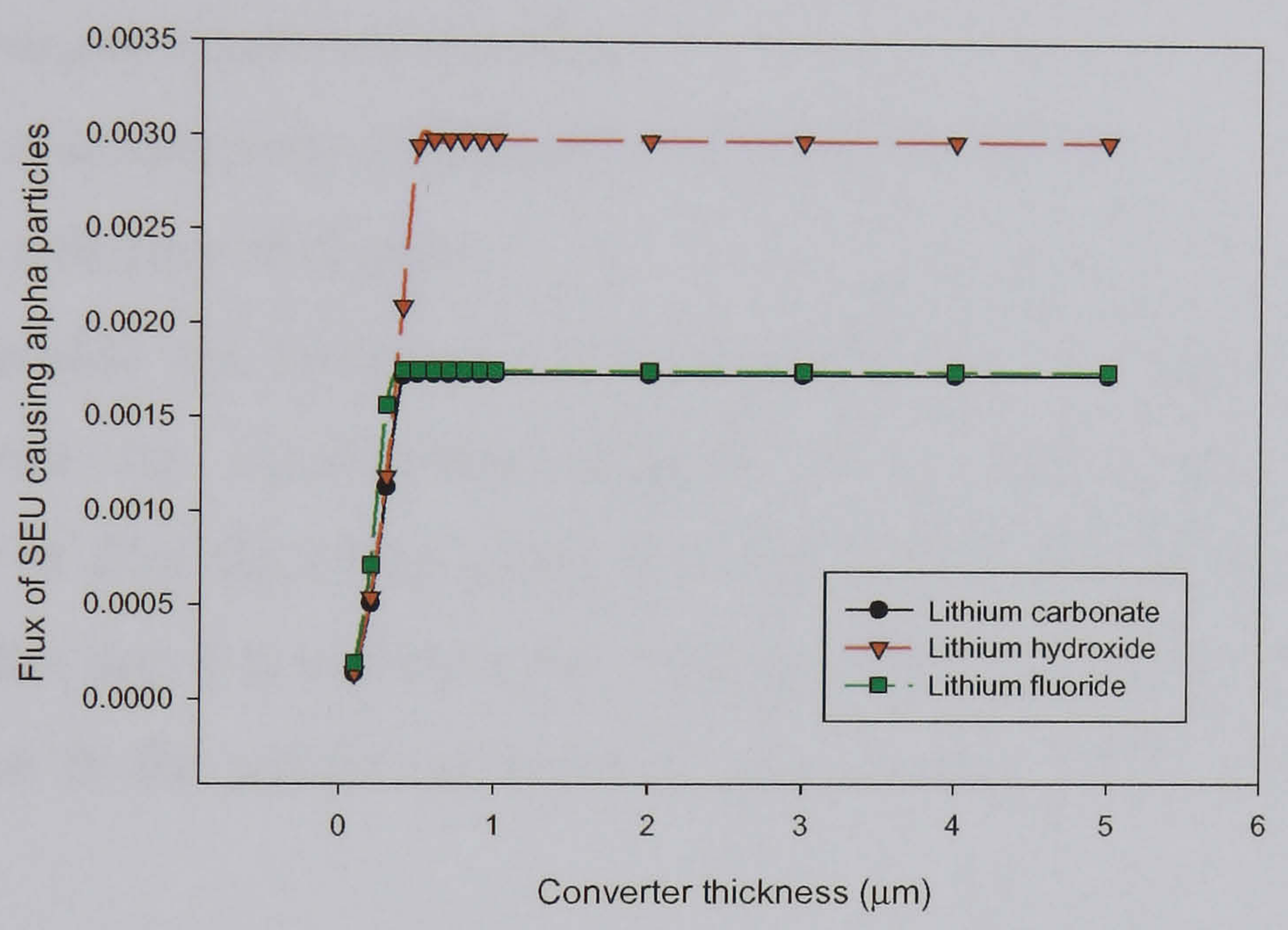

Figure 4.4 Detection sensitivity versus converter thickness

4.3 Investigation of the Converter Response

4.3.1 Fabrication of converter films

The converter fabrication was carried out using an Edward's vacuum evaporator system. Broadly, this consisted of a chamber which can be highly evacuated in which is located an electrically heated molybdenum boat, above this evaporation source is a rotating sample mount. The molybdenum boat was loaded with the compound of interest, preferably in a fine powder form, the chamber is then evacuated and when an acceptable vacuum has been achieved the boat is slowly warmed by increasing the

heater current carried by it. Eventually, the compound will melt and at that point it will escape by evaporation. This vapour will then condense on any cold surface it encounters.

Enriched lithium hydroxide films were deposited onto a polyethylene substrate held in a circular mask with a radius of (1.50±0.05) cm, therefore a total surface area of (7.07±0.47) cm^2. To determine the film thickness the mass gained was calculated by recording the mass (5 determinations and then averaged) of the substrate before and immediately after deposition. The thickness t was then determined using Equation 4.15.

$$t = \frac{m_f - m_i}{A.\rho} \qquad \textit{Equation 4.15}$$

where, m_f mass after deposition

m_i mass before deposition

A surface area of deposit

ρ density of deposit

In order to calculate the thickness it was assumed that the density of the deposited film would not be significantly different from that of the bulk material. Determination of film thickness using Equation 4.15 is further complicated by the uncertainty in the deposits surface area. Although care was taken when the mask was milled the error in the surface area due to inaccuracies in the mask dimensions is 6.7%.

Given the inherent uncertainties discussed above in determining film thickness by gravimetric means it was decided that a relative method should be adopted, using a transmission densitometer to determine the optical density of all the deposited films. Additionally these measurements allowed the uniformity of the deposited film to be assessed by recording the optical density at the centre and four equally spaced points across the film. The standard deviation of these results was used to quantify the non-uniformity of the films.

The results for 11 of the 13 films prepared on polyethylene substrates are shown in Table 4.7 and Figure 4.5. Two films suffered mechanical damage to the backing during handling and thus mass gained could not be measured. However, optical

density measurements were taken as the deposited film was undamaged and so could still be included in the irradiations.

Table 4.7 - Calculated Thickness and Optical Density Measurements

Nos.	Mass increase (μg)	Calculated film thickness (μm)	Optical density
1	400 ± 5	0.39 ± 0.01	0.085 ± 0.002
2	300 ± 5	0.29 ± 0.01	0.060 ± 0.009
3	830 ± 5	0.80 ± 0.03	0.211 ± 0.007
4	150 ± 5	0.145 ± 0.007	0.025 ± 0.002
5	No data	n/a	0.101 ± 0.002
6	310 ± 5	0.30 ± 0.01	0.217 ± 0.003
7	No data	n/a	0.646 ± 0.014
8	360 ± 5	0.35 ± 0.01	0.222 ± 0.001
9	260 ± 5	0.252 ± 0.009	0.137 ± 0.002
10	235 ± 5	0.228 ± 0.008	0.114 ± 0.009
11	1940 ± 5	1.88 ± 0.06	0.933 ± 0.002
12	340 ± 5	0.33 ± 0.01	0.027 ± 0.001
13	1130 ± 5	1.10 ± 0.03	0.702 ± 0.006

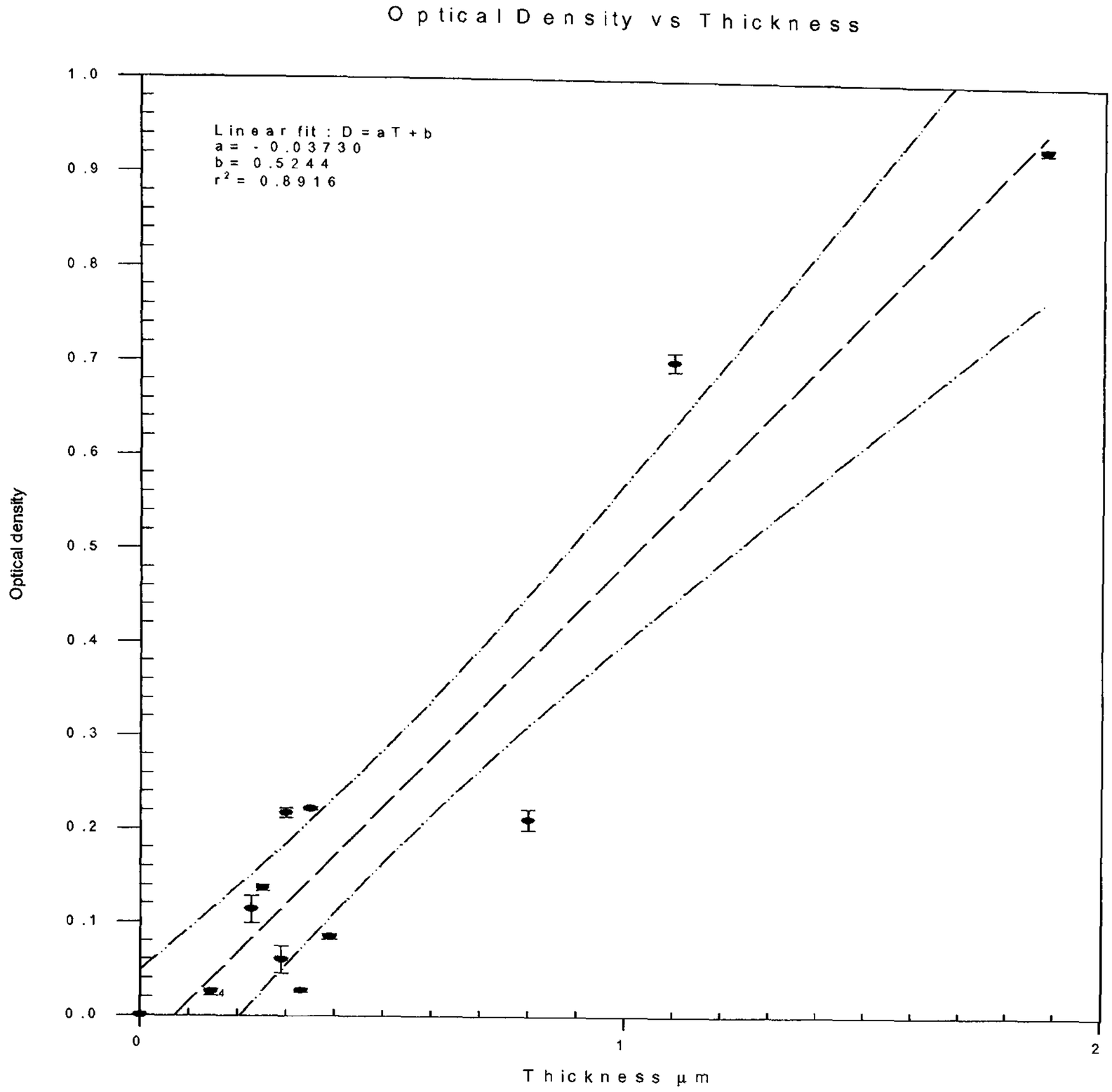

Figure 4.5 - Optical Density versus Thickness

It was observed that some films which had an almost equal thickness showed significant deviation from the best fit line e.g. films 6 and 12, 3 and 8. The explanation of these anomalous results concerned the preparation method. In some cases the films were prepared in two evaporations to achieve the required thickness, films 3, 6 and 12 were prepared in this manner. Two evaporations were necessary in cases were the initial charge was mostly blown out of the crucible by the outgassing of the lithium hydroxide. It was later discovered that this effect was due to a fault in the low voltage supply heating the crucible, which caused a too rapid rate of heating

During evaporation, each lasting around 120 seconds, the mask holding the film was rotated (at approximately 60 rpm) about its centre line to ensure uniformity of the deposited layer. There will inevitably be a variation in radial thickness since the distances from film to evaporating source will increase with radial distances. If the evaporating crucible is regarded as point-like, in this particular case a valid assumption as the source had a maximum diameter of 3 mm and was separated from the substrate by at least 23 times this diameter, an expression for this variation is

given in [4.24]. For the two source to film separations used, 10.0 cm (films thickness < 1.0 μm) and 7.0 cm (thickness > 1.0 μm), this variation is 2.2% and 4.4% respectively (centre point to edge). Only films 2,4 and 10 showed variations in density significantly greater than that predicted above, 15%, 8.0% and 7.9% respectively. Interestingly there was no correlation between non-uniformity and two stage evaporations.

4.3.2 Neutron irradiations of converters

The variation in the energy spectrum of the alpha particles produced by a converter, when exposed to a neutron fluence rate, was studied as a function of thickness with a surface barrier detector [4.25]. To achieve this a vacuum chamber was fabricated which allowed the converters to be repeatably mounted relative to the surface barrier detector.

All measurements were therefore made using an unmoderated 1.85×10^{11} Bq ^{241}Am/Be at Surrey University. The detector system consisted of Canberra surface barrier detector (type PD450-23-100), a Canberra pre-amplifier (model 2004DM), and an integrated spectroscopy amplifier (model 2020) and multi-channel analyser (model 1501). The Canberra software package Genie-PC was used to control and integrate the detector system. In accordance with the manufacturers instructions a shaping time of 0.5 μs was used with a bias voltage of 60 volts.

The detector system was calibrated using a mixed alpha source containing ^{239}Pu, ^{241}Am and ^{244}Cm with an activity of 7.5 kBq and a ^{148}Gd source with an activity 1.96 kBq. Peak centroids were determined using GENIE-PC for all observed peaks in the spectrum and are summarised in Table 4.8.

Table 4.8 Energy calibration of detector system

Peak	Isotope	Energy MeV	Centroid
1	^{239}Pu	5.1429	1249
2	^{239}Pu	5.1554	1260
3	^{241}Am	5.3890	1318
4	^{241}Am	5.4429	1331
5	^{241}Am	5.4857	1342
6	^{244}Cm	5.7628	1410
7	^{241}Cm	5.8049	1420
8	^{148}Gd	3.1820	811

Using a least squares fitting routine the best-fit line to was found and gave a calibration of 3.92 keV per channel.

Prior to collection of spectra from irradiated converters the response of a 'bare' detector was examined. The concerns being that the boron implanted contacts would contaminate the spectrum due to (n,α) reactions or that photon interactions would produce an unacceptably high background. Long irradiations of a bare detector confirmed that there was a background due to photon interactions but it was limited to channels corresponding to alpha energy less than 1.3 MeV, a similar observation was made by [4.26]. Since the energy range of interest was around 2 MeV this effect is not significant. No features were observed in these spectra that could be attributed to neutron interactions with the boron in the contacts.

Spectra were collected for a live time of 3600 seconds. Three key features were observed in all of the spectra: a low energy background due to photon interactions below 1.3 MeV, a broad low energy tailed peak centred around 2 MeV and a sharp well defined peak at 2.7 MeV. The peaks at 2 MeV and 2.7 MeV were attributed to the 2.055 MeV alpha and the 2.728 MeV triton produced by the lithium (n,α) reaction. The alpha peak, as expected, showed considerable low energy tailing due to straggling effects.

It was not possible to use the analysis routines of Canberra's GENIE-PC software to analyse the spectra as, as expected, the alpha peak had poor symmetry, FW0.1M/FWHM ratio typically 2.7 compared to the true Gaussian value of 1.82. Consequently the fitting algorithm frequently rejected these peaks. Instead regions of interest for the integrations were set by hand around each of the peaks. This was relatively easy for the triton peak as it retained a well defined shape for all film thicknesses and could be fitted by the Gaussian peak fit algorithms of the software. The low energy tailing of the alpha peak complicated the analysis as this tail began to merge into the photon background and the exact width of the peak could not be determined. This effect was particularly severe in the thicker films. To standardise the integration of the alpha peak the region of integration ROI was fixed over the energy range 1.8 to 2.1 MeV.

The results for 7 of the thirteen films are shown in Table 4.9 and Figure 4.7. Films 3,5,6,7 and 12 were excluded as they were either prepared using a two-stage evaporation and their optical density showed poor correlation with calculated thickness or no thickness data was available due to damage to the substrate. Film 2 was damaged during mounting in the chamber and consequently no data could be collected.

Table 4.9 – Converter thickness and alpha peak areas

Nos.	Thickness (μm)	Peak Area
4	0.145 ± 0.007	459 ± 42
1	0.39 ± 0.01	822 ± 57
10	0.228 ± 0.008	1360 ± 73
9	0.252 ± 0.009	1695 ± 80
8	0.35 ± 0.01	1683 ± 80
13	1.10 ± 0.03	1503 ± 76
11	1.88 ± 0.06	1642 ± 80

As may be seen in Figure 4.6, the variation of the alpha fluence rate shows the predicted step like behaviour. The variation of peak area shows two distinct regions. For thicknesses less than 0.4 μm a steep increase in peak area is seen, beyond this region the peak area remains relatively constant. It was therefore concluded that of the compounds considered the optimum choice was a layer of enriched lithium hydroxide with a thickness of at least 1 μm.

As noted earlier, together with a peak attributable to the alpha particle, a peak attributable to the triton was also observed in the spectra. The preceding analysis has only considered the alpha particles produced in the converter. It is well known that the range of tritons in silicon is considerably larger than the alpha range. Therefore, the energy deposited by a triton will be dispersed over a much larger region and hence it has previously been assumed [4.17] that tritons will be less effective at causing SEUs.

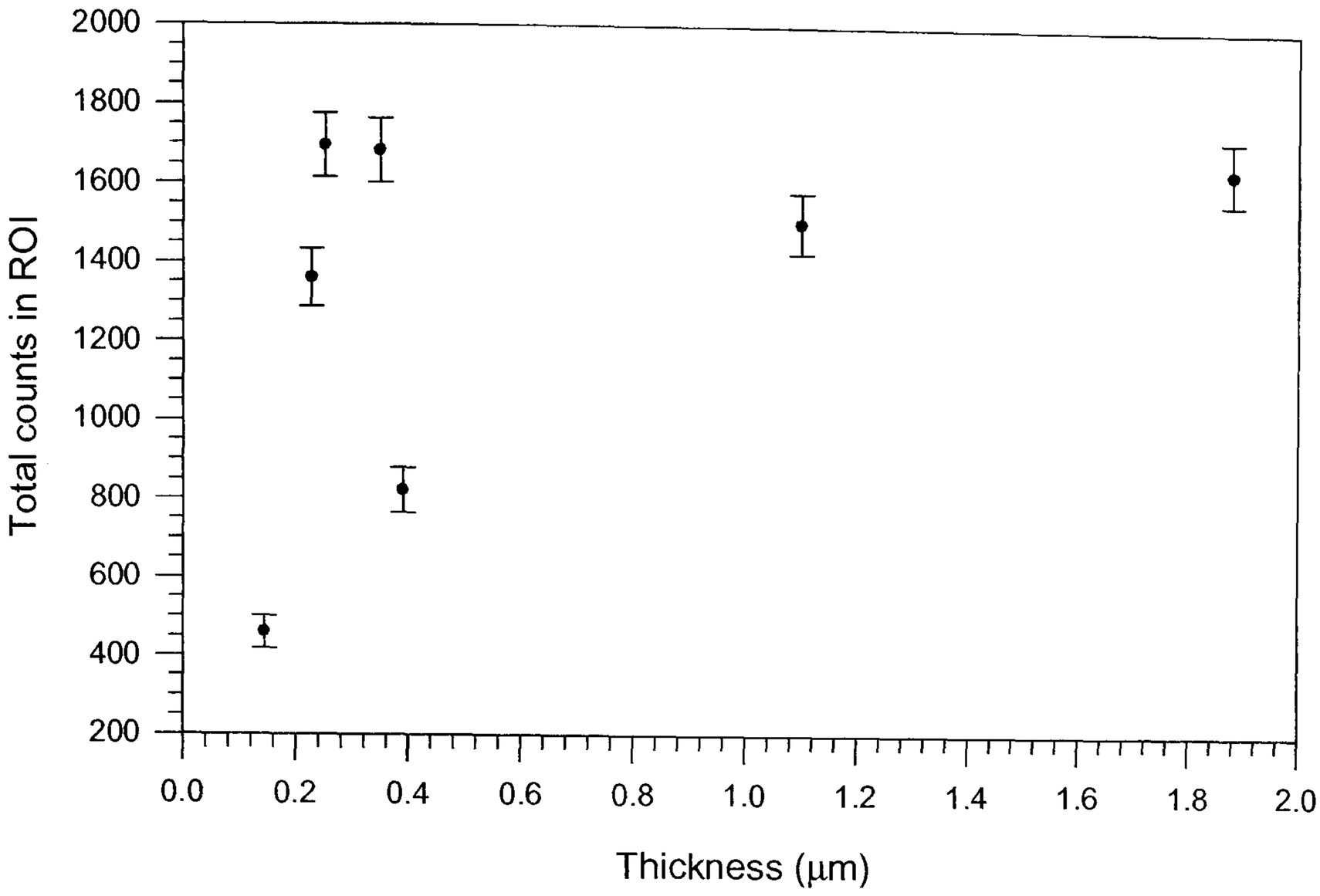

Figure 4.6 Total counts in alpha ROI versus Converter thickness

Since these tritons also have a longer range in the converter layer the maximum thickness of converter which they may still traverse and yet still have sufficient energy will be consequently larger. Therefore, a converter optimised for tritons will be thicker than that optimised for alpha particles. This additional thickness will not enhance the alpha particle SEU rate as alphas produced in this deeper region will either not exit the converter or have less than the required threshold energy. However, the additional thickness will reduce, by absorption, the neutron fluence rate in the region where alpha particles are produced which are capable of causing an SEU. It was, therefore, concluded that an optimised converter should have a thickness closer to the alpha particle optimum value rather than the triton. Additionally it was found that to deposit layers with thickness greater than ≈ 5µm very long evaporation times were required (>300 seconds). Considerable thermal damage could be seen both to the substrate and the film itself.

4.4 Experimental Study of 1 Mbit dRAMs

4.4.1 Alpha particle induced SEUs

1 Mbit dRAMs were obtained from three manufactures Siemens, Hyundai, and Fujitsu. To allow access to the die face the device packaging was partially removed. The de-encapsulation was undertaken by Defence Evaluation and Research Agency (DERA) Aquilla. The devices were first examined using a microfocal X-ray system to determine the position of the die within the package. A rubber mask was prepared which exposed only the portion of the packaging immediately above the die. The packaging was then removed by etching with hot nitric acid in a commercial de-encapsulation system. A micrograph of the Siemens 1Mb device is shown in Figures 4.7, and Figure 4.8 shows this device after the packing has been etched to expose the device surface.

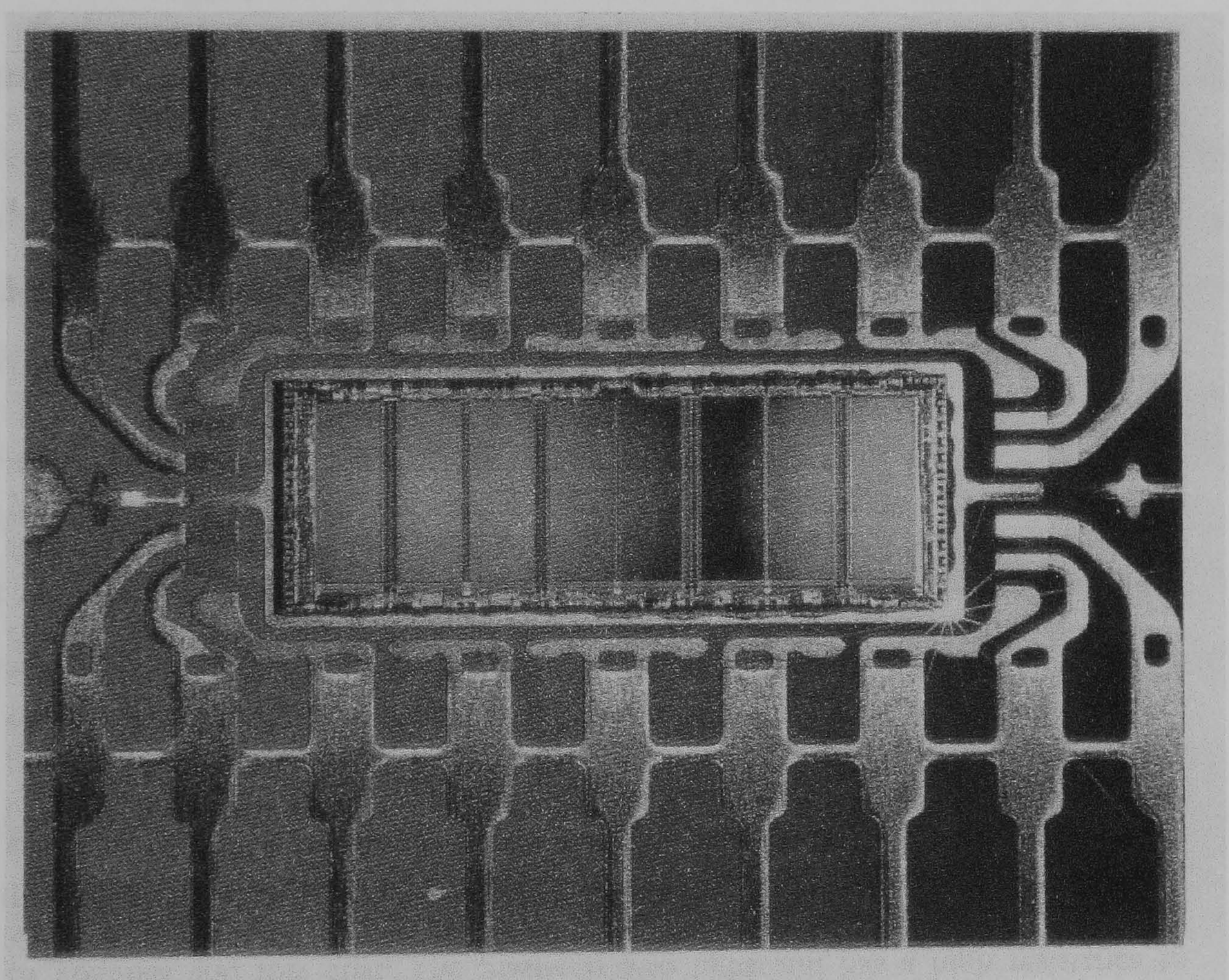

Figure 4.7 Micrograph X-ray of Siemens 1Mb dRAM

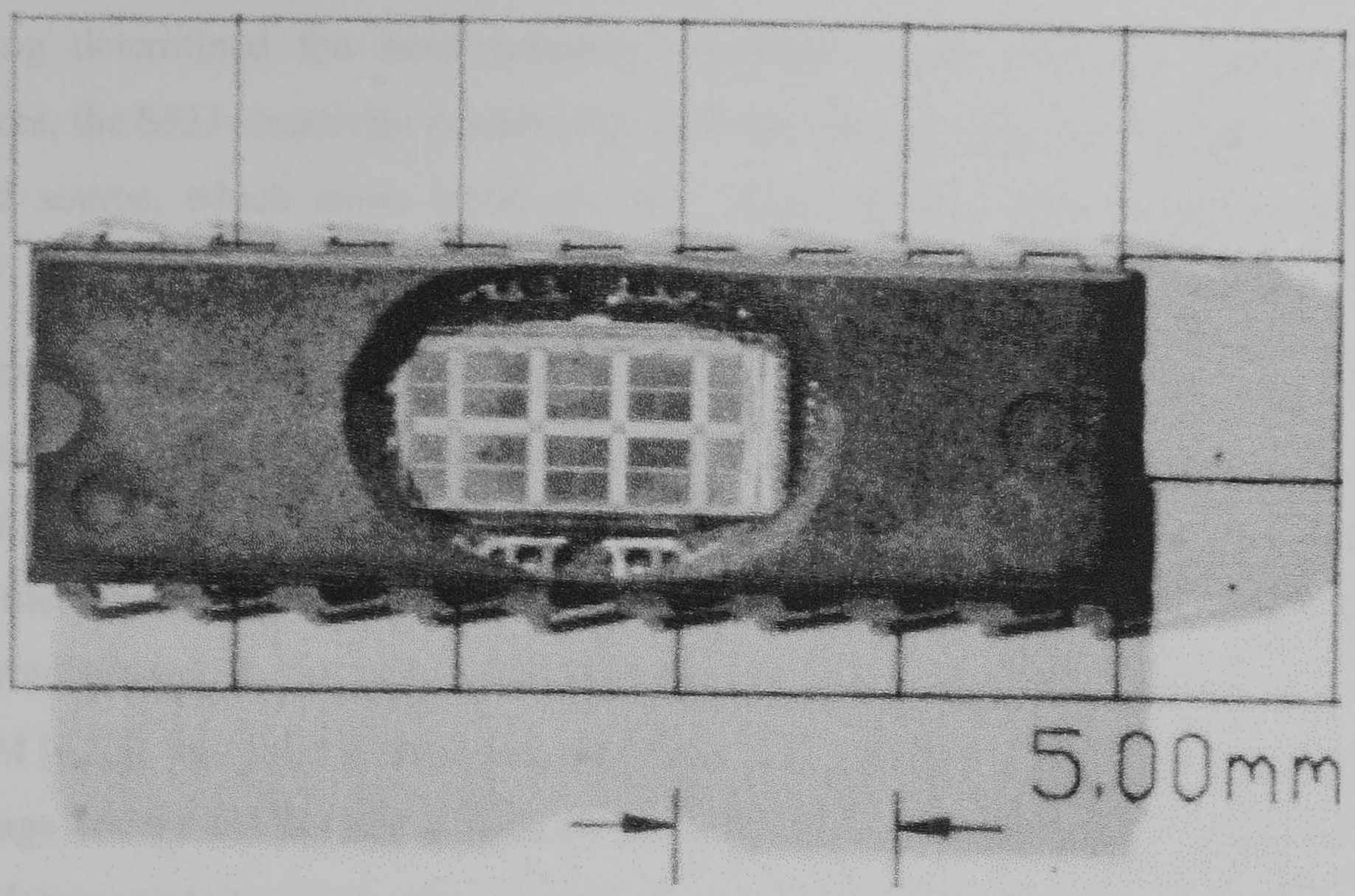

Figure 4.8 Siemens 1Mb dRAM showing exposed surface

A test rig was designed [4.27], which allowed a test pattern to be repeatedly written and read from each memory location and also to provide the necessary control and refresh signals. Any difference between the written data pattern and the subsequent read data pattern would indicate that a SEU had occurred. An output file is generated which tallies the read data pattern and the total run time.

It has previously been reported that the SEU sensitivity of a dRAM is dependent upon the device operating voltage [4.28], cycle time [4.12] and data pattern [4.17]. The effect of these three parameters on the SEU sensitivity of each of the three manufacturers device has been studied, the results of which may be found elsewhere [4.27].

The operating parameters that gave the greatest SEU sensitivity for alpha particles originating from an ^{241}Am source are summarised below in Table 4.10.

Table 4.10 – Operating parameters for highest SEU sensitivity

Manufacturer	Operating voltage (V)	Refresh cycle time (μs)	Data pattern
Siemens	3.4	13.6	1111
Hyundai	3.1	13.6	1111
Fujitsu	2.9	13.6	1111

Having determined the most sensitive conditions under which to operate these devices, the SEU sensitivity to alpha particles of a lower energy was examined using a ^{148}Gd source, which emits mono-energetic alpha particles with an energy of 3.18 MeV. The source used had an activity of 1.96 kBq at the time of measurement.

All measurements were made at atmospheric pressure with a source to die surface separation of 4 mm; this value dictated by the packaging design of the devices. An alpha spectrum under these conditions was collected to determine the attenuation of the intervening 4-mm air gap; the resulting spectrum indicated a single peak with a centroid located at 2.4 MeV. Additionally, the charged particle Monte Carlo code SRIM [4.23] was used to simulate this experimental arrangement and determine the average energy of the alpha particles reaching the die surface. The results of this simulation predicted an average energy of 2.64 MeV. The SEU absolute efficiencies of the three devices are given in Table 4.11.

Table 4.11 – SEU efficiency for ^{148}Gd alpha particles

Manufacturer	SEU (s^{-1})	ε_α - Efficiency
Siemens	1.28 ± 0.07	$(6.5 \pm 0.4)\times10^{-4}$
Hyundai	0.68 ± 0.05	$(3.5 \pm 0.3)\times10^{-4}$
Fujitsu	0.78 ± 0.05	$(4.0 \pm 0.3)\times10^{-4}$

4.4.2 Neutron Detection

It is known that within dRAM devices boron is used as a dopant. The potential therefore exists for neutrons to interact with this boron dopant and so produce alpha particles through the high cross-section (n,α) reaction. The response of unconverted dRAM to neutrons was therefore examined.

In order to study the device response to neutrons the header board holding the device under test was positioned within the beam of the 135° face of the Imperial College London CONSORT II reactor. The beam was characterised using manganese foils to determine the thermal neutron fluence rate with the reactor operating at 100 kW. The neutron dose rate as indicated by a Leake type Mark 7 NRM spherical neutron dosemeter was also recorded. These results are shown in Table 4.12.

Table 4.12 – Characteristics of the 135° face beam line

Determination	Value
Manganese foils (mean of 3 measurements) - $\dot{\Phi}_{th}$	$(8.6 \pm 1.4) \times 10^{4}$ cm^{-2} s^{-1}
Neutron dose rate	1.0 ± 0.1 mSv h^{-1}
Gamma dose rate	≈ 35 mSv h^{-1}

The devices were each exposed for 20 minutes firstly bare and then with a 3-mm cadmium filter to absorb the thermal component of the beam. The results of these exposures are given in Table 4.13.

Table 4.13 – Neutron SEU sensitivities for un-coated devices

Manufacturer	R_b – SEU rate Bare (s^{-1})	R_{bCd} – SEU Cd covered (s^{-1})	ε_u – Neutron SEU sensitivity $R_b/\dot{\Phi}_{th}$ (cm^2)
Siemens	$(9 \pm 3) \times 10^{-3}$	$(8 \pm 4) \times 10^{-4}$	$(10 \pm 4) \times 10^{-8}$
Hyundai	$(20 \pm 6) \times 10^{-3}$	0	$(23 \pm 8) \times 10^{-8}$
Fujitsu	0	0	0

Although the previous work had suggested a lithium hydroxide converter would be the optimum converter its long-term stability was questionable. When the films previously produced were re-examined some weeks later it was noticed that they had considerably deteriorated. On close inspection portions of the coating had become detached from the substrate. It was considered likely that this deterioration could be attributed to the hydroscopic nature of lithium hydroxide, the films may be especially sensitive as the material deposited by evaporation will be in the anhydrous form. As long-term stability of the converter layer is required for repeatable detector operation lithium fluoride was used instead. Lithium fluoride had initially been discounted because of its known toxicity. However, chemically it is a much more stable than lithium hydroxide. Having taken appropriate precautions lithium fluoride, enriched to 95% by atom ^{6}Li, was deposited onto the device surface again by vacuum evaporation.

An Edward's resonating quartz crystal film thickness monitor was now available for use in the vacuum evaporation system. This device makes use of the change in

resonant frequency of a quartz crystal as material is deposited onto one of its surfaces. With knowledge of the deposit's density, assumed to be equal to the bulk density, the monitor can be calibrated to directly read deposited film thickness. The crystal head was positioned such that the quartz crystal face lay at the same distance from the evaporating source as the dRAMs surface when positioned in the rotating sample mount. All deposited film thickness could then be measured directly using the monitor. In all cases a nominal thickness of 3 μm was deposited; the precise values are shown in Table 4.14, the uncertainty quoted is the scale reading error of the digital display.

Again the devices were each exposed for 20 minutes firstly bare and then with a 3-mm cadmium filter. The results of these exposures are given in Table 4.14.

Table 4.14 – Neutron SEU sensitivities for coated devices

Manufacturer	Converter thickness (μm)	R_c – SEU rate Bare (s^{-1})	R_{cCd} – SEU Cd covered (s^{-1})	ε_c – Neutron SEU sensitivity $R_c/\dot{\Phi}_{th}$ (cm^2)
Siemens	3.9 ± 0.1	$(7 \pm 2) \times 10^{-3}$	0	$(8 \pm 3) \times 10^{-8}$
Hyundai	3.7 ± 0.1	$(23 \pm 6) \times 10^{-3}$	0	$(27 \pm 8) \times 10^{-8}$
Fujitsu	3.8 ± 0.1	$(38 \pm 6) \times 10^{-3}$	$(3 \pm 2) \times 10^{-3}$	$(44 \pm 9) \times 10^{-8}$

4.5 Discussion and Conclusions

4.5.1 Charged Particle Converter

The alpha range has been found to be small in the compounds of interest and the neutron fluence rate can be regarded as virtually constant over distances comparable to this range. Hence the effect of varying the converter thickness will be to act solely on the alpha particles, since for the small changes involved, the variation in neutron fluence rate will be very small. For example, assuming a 95% ^{6}LiOH converter the worst case due to the moderating effect of the hydrogen present, the variation in neutron fluence rate over 5 μm has been found to be less than 1.6%.

If an alpha particle is produced at a depth much greater (i.e. > 3*a* see Table 4.5) than the range then the probability of it exiting with sufficient energy to cause a SEU is very small. A SRIM simulation of a 1 μm (approximately 2*a*) thick ^{6}LiOH for 5×10^5 2055 keV alphas found no transmitted particle with an energy greater than 1950 keV,

limiting the probability to less than 0.0002%. It is therefore suggested that provided the converter is thicker than the $2a$ no significant increase in SEU causing alpha particle fluence rate will be seen. Alpha particles produced any deeper than $2a$ in the converter are extremely unlikely to contribute to the error cause fluence rate.

The suggestion that once some maximum thickness is reached further increases in converter thickness will not alter the total error causing alpha fluence rate is supported by the results of the numerical integrations, see Figure 4.4. The results of the numerical integration's show that the lithium compounds considerably affect the detection sensitivity.

4.5.2 1 Mbit dRAMs

A theoretical prediction based on the scaling of the storage capacity from previously measured sensitivities for 64 kbit devices to 1 Mbit capacity devices predicted an alpha SEU efficiency of 8.6×10^{-5}. The previously determined 64 kbit sensitivity was measured using an ^{241}Am source and consequently the observed sensitivity for 1 Mbit was anticipated to be lower as a consequence of the lower energy of ^{148}Gd alpha source used in these measurements. The observed mean sensitivity of 4.7×10^{-4}, however, indicates that the alpha SEU efficiency of the new generation of devices has increased in excess of that expected due solely to the increased number of storage cells. Furthermore, whilst a lower energy alpha source was used this did not reduce the SEU efficiency. These observations may be due to the architecture of the new devices – an area that requires further investigation.

A simple theoretical model for predicting the expected neutron induced SEU sensitivity of these devices was developed, described below. This model analyses the SEU process in two stages, first calculating the reaction rate for the generation of alphas through the (n,α) reaction and then using the measured alpha efficiency to convert the reaction rate to a predicted SEU sensitivity.

The Monte Carlo code MCNP4b [4.22] was used to determine the likely neutron fluence rates at the embedded detector positions. A typical result from these simulations indicates that for a dose rate of 100 μSv h^{-1} with a neutron energy of 200 keV the predicted fluence rate at the detector positions is of the order 150 cm^{-2} s^{-1}. This fluence rate would generate an SEU rate of approximately 3.9×10^{-5} s^{-1}. This

SEU rate is too low for a dRAM to be considered as the embedded detector within an operational dosemeter that may be required to monitor dose rates as low as 1 $\mu Sv\ h^{-1}$.

4.5.3 Conclusion

This study has demonstrated that 1 Mbit dRAM memories are sensitive to low energy alpha particles and that this sensitivity has increased beyond that expected from the increase in storage capacity. Furthermore, it has been demonstrated that through the use of an external lithium fluoride converter they can be sensitised to neutrons.

The measured sensitivity for neutrons indicates that although neutron detection is achievable, the sensitivity is too low for them to be considered, using present technology, as the embedded detectors in an operational dosemeter. The use of PIN diodes was therefore investigated and no further work on dRAMs was undertaken.

4.6 Reference for Chapter 4

[4.1] Schroder O., Schmitz T., Can a personal dosemeter for neutron radiation based on a semiconductor chip match the new ICRP recommendation. **Rad. Prot. Dosim**., 54(3/4),361, 1994.

[4.2] Schroder O., Schmitz T., The application of commercial semiconductor chips for personal neutron dosimetry. **Rad. Prot. Dosim**., 61(1-3), 9, 1995.

[4.3] Darambara D.G., Spyrou N.M., Neutron detection using soft-errors in dynamic random access memories. **Nucl. Instr. and Meths. in Phys. Res**., A348, 491, 1994.

[4.4] Pierschel M., Ehwald K.E., Heinemann B., Januschewski F., Schmitz T., Schroder O., A BCCD based Dosemeter for mixed radiation fields. **Nucl. Instr. and Meths. in Phys. Res**., A326, 304, 1993.

[4.5] Downing R.G., Zeissler C.J., Chen H.. High resolution charged particle and neutron imaging using charge injection devices. **SPIE**, 1737, 308, 1992.

[4.6] Bordy J.M., Lahaye T., Landre F., Hoflack C., Lequin S., Barthe J., Single diode detector for individual neutron dosimetry using a pulse shape analysis. **Rad. Prot. Dosim**., 70(1-4), 73, 1997

[4.7] Darambara D.G., Beach A.C., Spyrou N.M., Development of a novel neutron detector for imaging and analysis. **J. Radioanal. Nucl. Chem. Art**., 167(1), 197, 1993.

[4.8] May T.C., Woods M.H., Alpha particle induced soft errors in dynamic memories. **IEEE Trans. Elect. Dev**., ED 26(1), 2, 1979.

[4.9] Cerofolini G., Ferla G., A proposal : Dynamic RAMs as particle detectors. **Nucl. Instr. Meths**., 169, 125, 1980.

[4.10] Davis J.L., Use of computer memory chips as the basis for a digital albedo neutron Dosemeter. **Health Physics**, 49(2), 259, 1985.

[4.11] Lund J.C., Sinclair F., Entine G., Neutron Dosemeter using a dynamic random access memory as a sensor. **IEEE Trans. Nucl. Sci**., 33(1), 620, 1986.

[4.12] Prince B., **Semiconductor memories: A handbook of design, manufacture and application**, 2nd ed. Chichester: John Wiley & Sons, 1991.

[4.13] Sze S.M., **VLSI Technology**. Singapore: McGraw-Hill, 1983.

[4.14] Boonstra L., Lambrechtse C.W., Salters R.H.W., A 4096 bit One Transistor per Bit Random Access Memory with Internal Timing and Low Dissipation. **IEEE J. Sol-St Circ.**, SC-8, 305, 1973.

[4.15] Kuo C., Kitagawa N., Ogden D., Hewkin J., 16 k RAM Built with Proven Process may Offer High Start-up Reliability, **Electr**., 49, 81, 1976.

[4.16] Knoll G.F., **Radiation Detection and Measurement**, 2nd ed., Chichester: John Wiley & Sons, 1989.

[4.17] Darambara D.G., **Use of Single Event Upsets in Dynamic Random Access Memories as the Basis for a Position Sensitive Radiation Detector**, Ph.D. thesis, University of Surrey, 1994.

[4.18] JEFF-PC ver 2.2

[4.19] Lide D.R. Editor-in-Chief. **CRC Handbook of Chemistry and Physics 73rd Edition**, Boca Raton Florida: CRC Press, 1992.

[4.20] Price B.T., Horton C.C., Spinney K.T., **Radiation Shielding**, London: Pergamon Press, 1957.

[4.21] Henry A.F., **Nuclear-Reactor Analysis**, London: MIT Press, 1980.

[4.22] Briesmeister J.F. Eds. **MCNP – A General Monte Carlo N-Particle Transport Code**. Los Alamos National Laboratory, 1997. LA-12625-M.

[4.23] Ziegler J.F., Biersack J.P. and Littmark U., **The Stopping and Range of Ions in Solids"**, New York: Pergamon Press, 1985.

[4.24] Holland L., Vacuum Deposition of Thin Films, London: Chapman and Hall Ltd, 1961.

[4.25] Chapman N., **An Investigation into the Response of a Neutron Converter Layer to Thermal Neutron Irradiation**, MSc thesis, University of Surrey, 1996.

[4.26] Tanner J.E., Witts D., Tanner R.J., Bartlett D.T., Burgess P.H., Edwards A.A., More B.R., Taylor G.C., Thomas D.J., An assessment of the feasibility of using Monte Carlo calculations to model a combined neutron/gamma electronic personal dosemeter. **Rad. Prot. Dosim**., 61(1-3), 183, 1995.

[4.27] Harvey S., **Charged Particle Induced Soft Errors in 1 Mbit and 4 Mbit dRAMs as the Basis for a Portable Radiation Detector System**, PhD thesis, University of Surrey, 1998.

[4.28] Lund J.C., Sinclair F., Entine G.. Neutron Dosemeter using a dynamic random access memory as a sensor. **IEEE Trans. Nucl. Sci**., 33(1), 620, 1986.

Chapter 5 Neutron Detection using Photodiodes

5.1 Properties of Semiconductors

Prior to the discussion of PN photodiodes (PIN) themselves a review of semiconductor physics is provided. An exhaustive discussion of this subject is beyond the scope of this thesis, however, Davies [5.1] discusses semiconductor theory comprehensively.

5.1.1 Intrinsic semiconductors

In a semiconductor material there is a small energy separation, typically less than 2 eV, between the valence and conduction bands, the band gap E_G. An intrinsic semiconductor is a semiconducting material that is sufficiently free of impurities that its properties are solely determined by the material itself (i.e. band gap) and the temperature. For example, germanium has a band gap E_G of 1.12 eV (at 298 K) the required impurity level is less than 1 part in 10^{13} [5.1].

For a semiconductor at 0 K all of the available energy states in the valence band up to an energy E_V are completely filled leaving the conduction band ($E > E_C$) empty. As there are no free states available for an electron to move to the material will behave as an insulator. For any temperature above 0 K thermal excitation energy, given by kT, will promote a proportion of the electrons in the valence band to the conduction band. At room temperature the mean thermal energy is approximately 0.025 eV and therefore only a very small proportion of the valence electrons will receive sufficient energy to cross the band gap. This situation is shown schematically in Figure 5.1.

5.1.2 Extrinsic semiconductors

An extrinsic semiconductor is a semiconducting material whose electrical characteristics are determined by the impurities present rather than the material itself. Considering the case of the most common semiconductor materials silicon and germanium). Both of these elements are Group IV elements and form a tetrahedral covalently bonded crystal structure (i.e. an individual atom shares its four valence electrons with its four nearest neighbours). If a small amount of a Group V element such as phosphorous or arsenic is introduced into the semiconductor, substitutions of phosphorus atoms instead of silicon atoms in the crystal lattice leads to a surplus electron. Although weakly bound, energy level E_D, to the parent impurity atom, at room temperature there is sufficient thermal energy to allow this electron to escape

from its parent atom. The electron is now free to move through the crystal. The impurity is said to have donated an electron to the conduction band, hence Group V elements are referred to as donor impurities. However, if a small quantity of a Group III element such as boron is introduced, substitutions of boron atoms lead to a deficiency of electrons. Again at room temperature this deficiency is not localized due to the weak 'bonding' to the parent atom E_A. The absence of an electron so caused may be regarded as behaving like a free electron but with a positive charge, these are often referred to as holes. Such dopants are referred to as acceptors. These two cases are shown schematically in Figure 5.2.

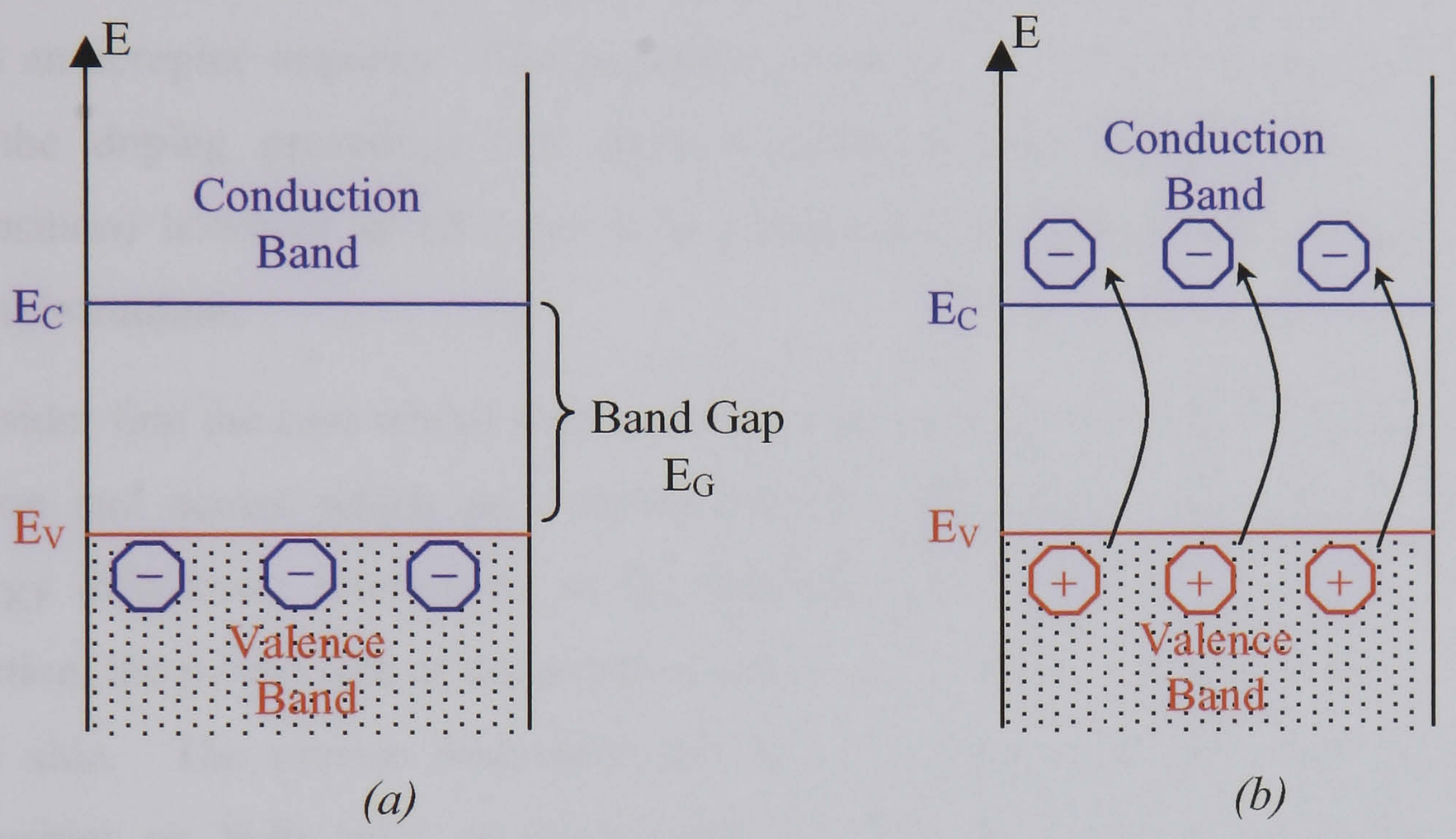

(a) (b)

Figure 5.1 (a) Intrinsic at 0K (b) thermal excitation of valence electrons

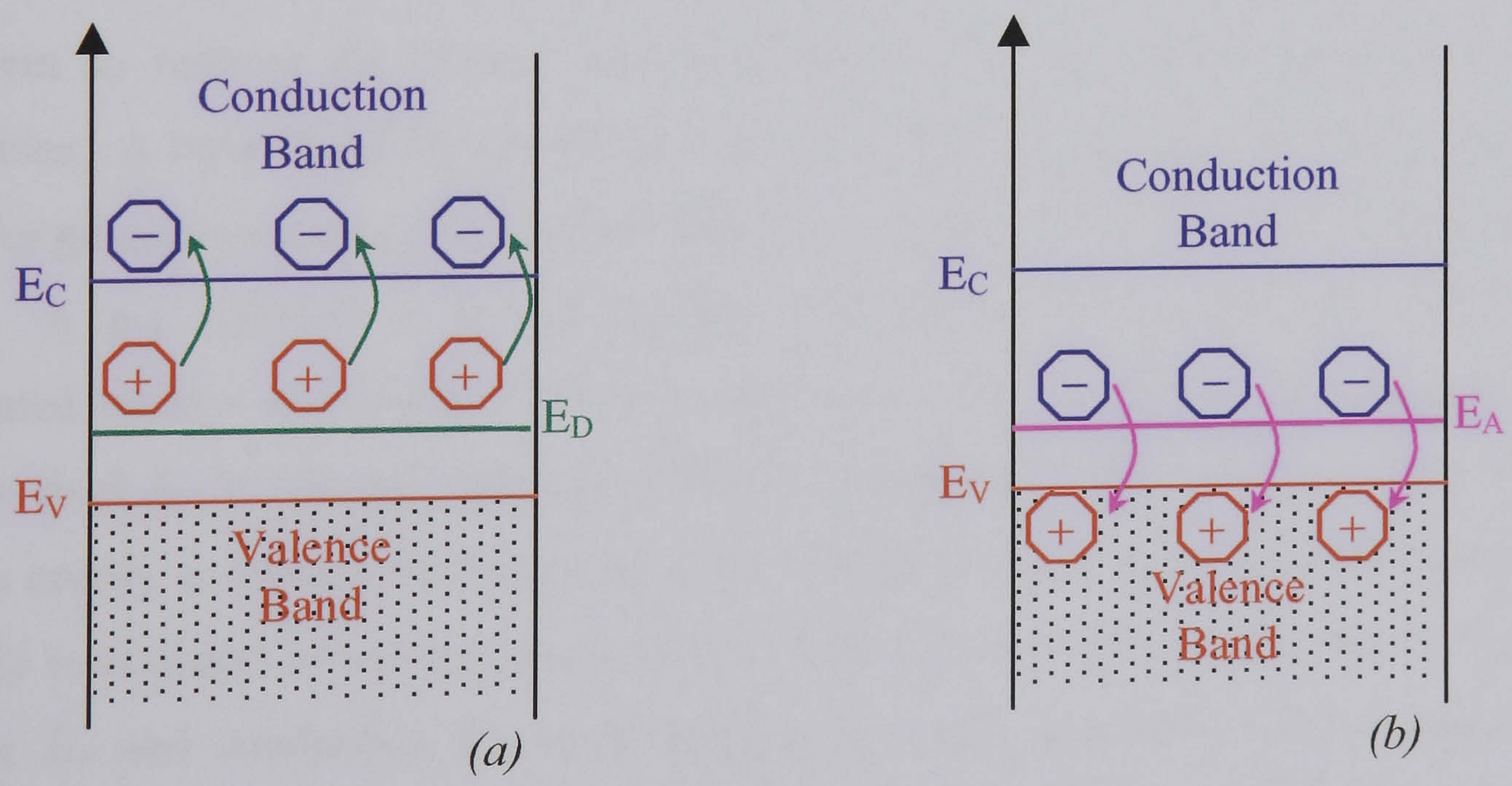

Figure 5.2 (a) Donor impurity (b) Acceptor impurity

In the case of silicon doped with a donor the majority charge carriers will be the excess electrons and the material is referred to as n-type. Whilst for an acceptor doping the majority charge carriers will be the holes, absence of an electron, and the material is referred to as p-type. Within a bulk sample of silicon both p and n type material can exist. At the transition between p and n-type material a p-n junction will be formed.

5.1.3 Electrical characteristics of the p-n junction

A p-n junction is formed when, within the bulk of silicon substrate, an abrupt transition occurs between a region doped with a donor impurity and a region doped with an acceptor impurity. The particular physical form of the junction will depend on the doping procedure (i.e. thermal diffusion, ion implantation or epitaxial deposition) however in all cases it is necessary to maintain the continuity of the crystal structure.

Consider first the case where such a p-n junction has been formed in a bulk sample of silicon and across which no external potential difference is applied. A potential energy difference, referred to as the diffusion potential U_D will exist across this junction, the p-type side of the junction will be at a negative potential relative to the n-type side. The precise magnitude of U_D will depend upon the concentration of impurities on both sides of the junction N_D and N_A, however, for lightly doped semiconductors U_D is well approximated by the band gap. Effectively a region will be formed in which the internal electrical field, due to the diffusion potential, is sufficient to remove the charge carriers produced by the ionised donor/acceptor impurities. A layer on either side of the junction will be formed in which there are no free charge carriers and for this reason this layer is often referred to as the depletion layer. A p-n junction is shown schematically in Figure 5.3 together with the associated energy and charge carrier distributions. On the energy distribution an energy level E_F is shown, this is the Fermi energy and represents the maximum kinetic energy a valence electron may have. In the absence of an applied electrical field E_F is constant across the p-n junction. Since the position of E_F relative to the valence E_V and conduction E_C band energies is solely dependent on the impurity concentration to maintain a constant E_F throughout the material the energies of the valence and conduction bands E_V and E_C must vary.

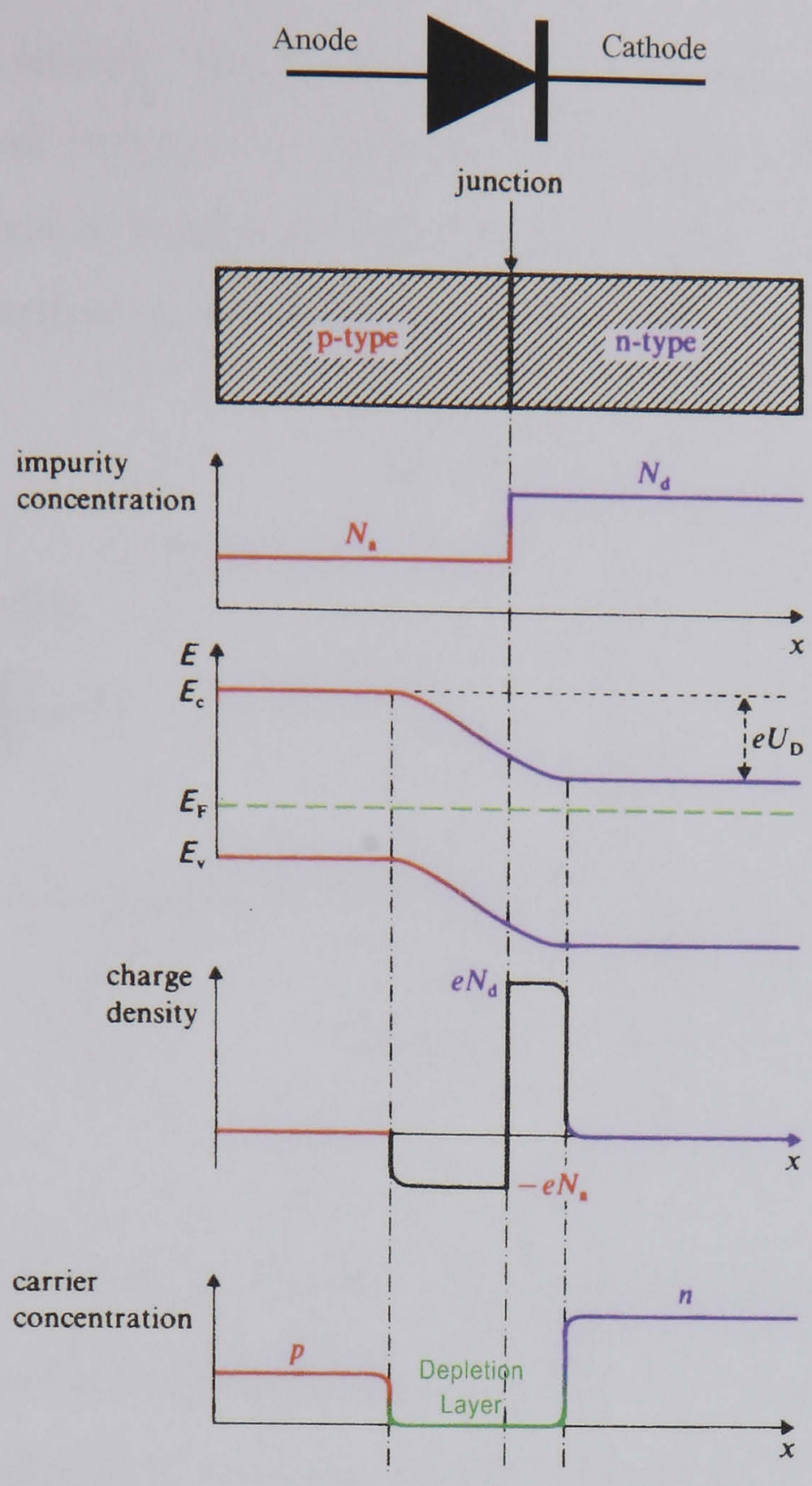

Figure 5.3 Schematic of a p-n junction redrawn from [5.1]

The p-n junction can also be used with an external potential difference applied. Two possibilities exist, forward bias where the p-type layer is at a positive potential and reverse bias where the p-type layer is at a negative potential. In the case of forward bias if the external bias V_B is less than U_D (which may be approximated by the band gap E_G) then essentially no current will flow, however, once V_B exceeds U_D a large current will flow. Qualitatively, as the external bias V_B, which is in the opposite sense to the diffusion potential U_D, is increased the effective diffusion potential ($U_D - V_B$) reduces. Consequently the width of the depletion layer will also be reduced. When V_B exceeds U_D there is no effective diffusion potential and hence no depletion layer, the p-n junction will now conduct. With reverse bias (i.e. the p-type layer is at a negative potential) the external bias V_B is in the same sense as the diffusion potential U_D and so the effective diffusion potential will be enhanced ($U_D + V_B$). In this case the width of the depletion layer will be increased. As V_B is increased further the width of the depletion layer will grow ever greater until eventually it extends across the

whole bulk of the silicon. The p-n junction is then said to be fully depleted. Further increases in V_B will enhance the electrical field strength in the depletion layer until eventually a destructive breakdown occurs. The current versus voltage characteristics of a typical p-n junction are shown in Figure 5.4.

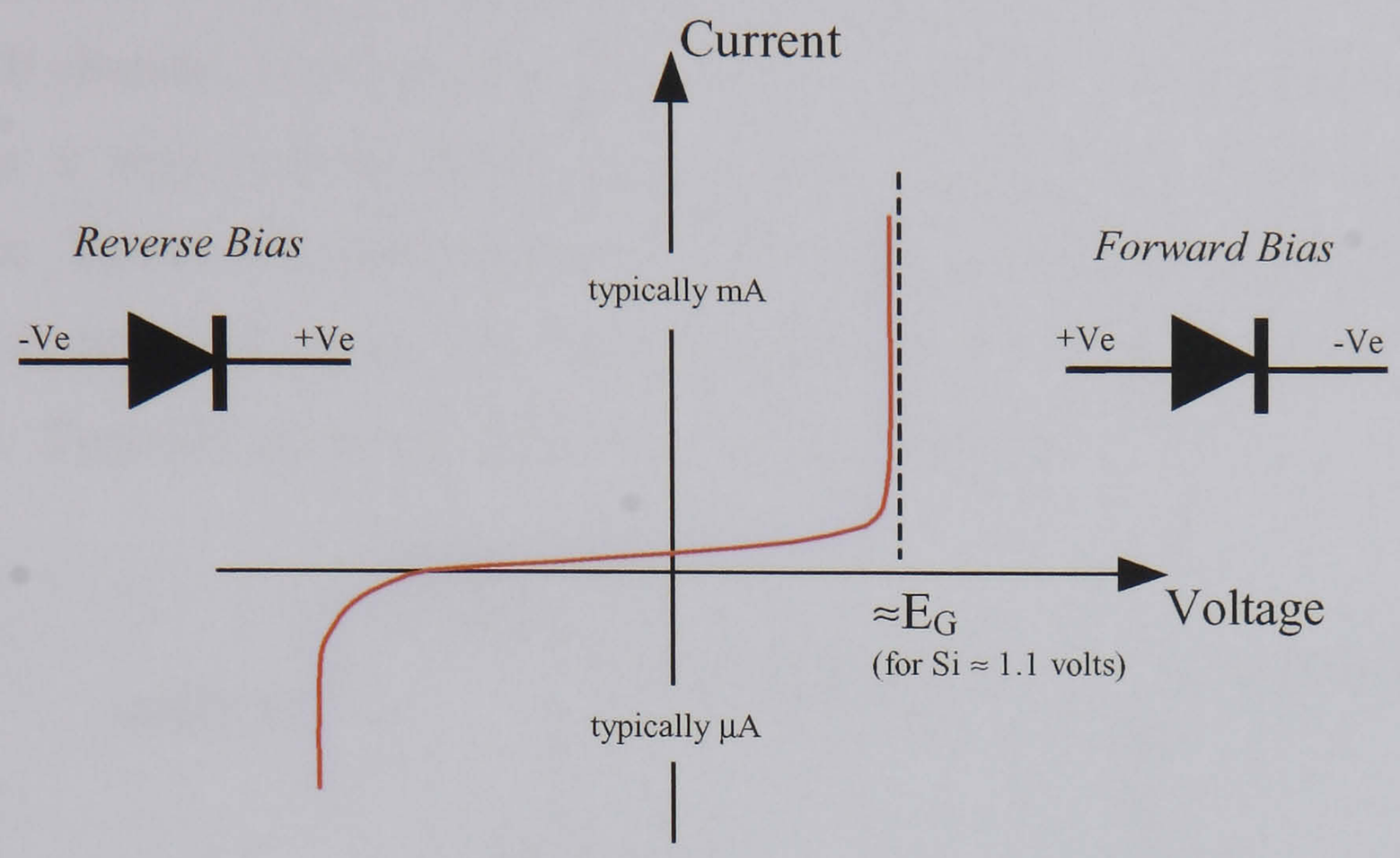

Figure 5.4 Current vs. Voltage characteristics of a typical p-n junction

If the depletion layer in a p-n junction is considered as forming a simple parallel plate capacitor (i.e. edge effects are ignored) the classical expression for the capacitance may be used and is given in Equation 5.1.

$$C = \frac{A \varepsilon \varepsilon_0}{d} \qquad \textit{Equation 5.1}$$

where, C – capacitance of junction (F)

ε - dielectric constant of material (relative to vacuum) = 12 for silicon [5.2]

ε_0 – dielectric constant of vacuum = $8.854187817 \times 10^{-12}$ (F m^{-1}) [5.3]

A – area of depletion layer (m^2)

D – width of depletion layer (m)

5.2 The Silicon p-n Junction Photodiode (PIN)

5.2.1 Fabrication

A schematic cross section of a PIN photodiode is shown in Figure 5.5. On a substrate of n-type silicon a layer of p-type material is produced by selectively diffusing a Group III element, most usually boron, into the substrate. On the rear surface of the substrate a very heavily doped n-type layer, signified n^+, is also produced by diffusion. Electrodes, most commonly aluminium, are then deposited by evaporation to provide electrical connections to the p-type layer, the anode, and to the n^+ layer, the cathode. Typically the p-type layer is less than 1 μm thick.

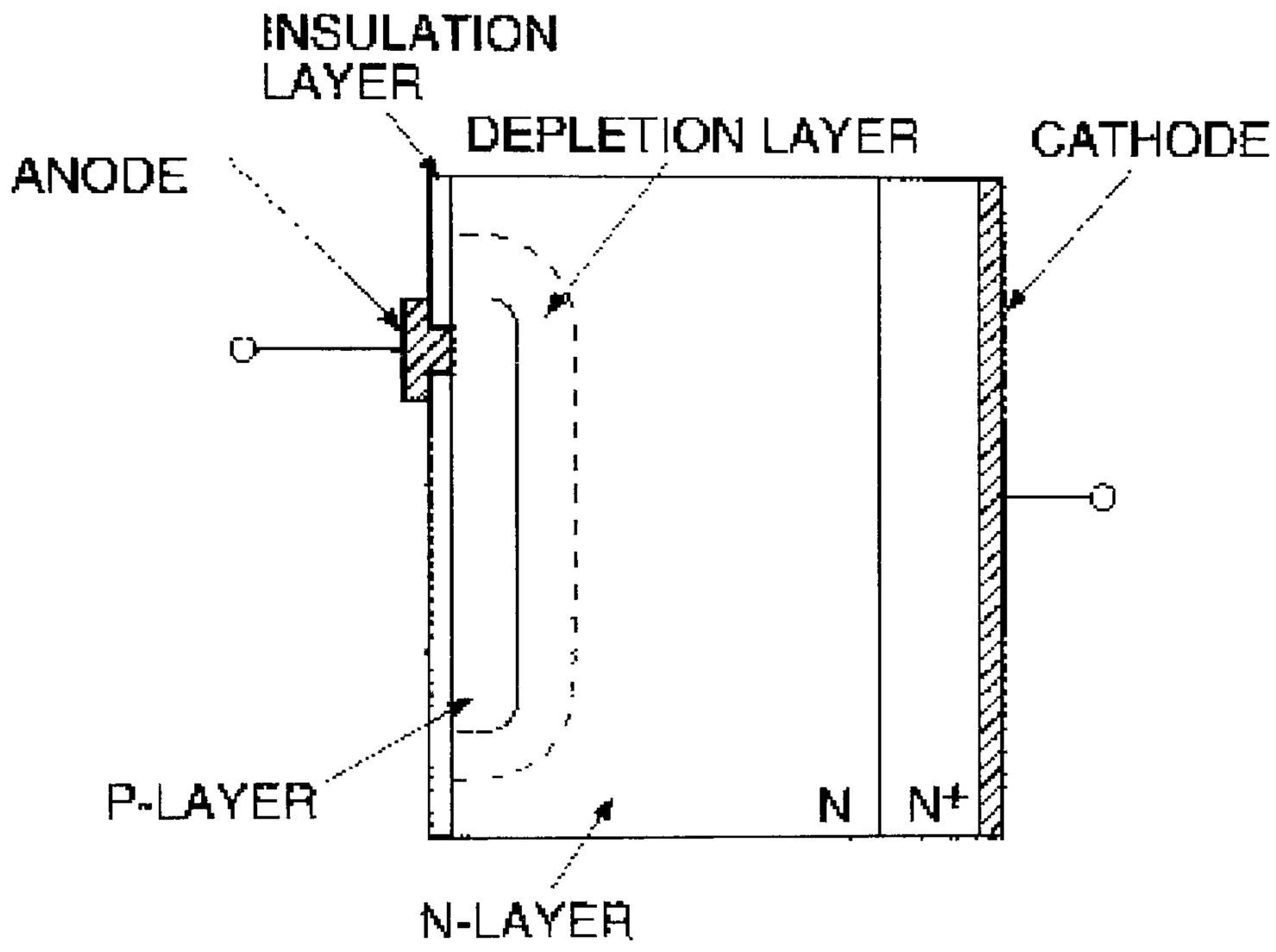

Figure 5.5 Cross section of a typical photodiode redrawn from [5.4]

Photodiodes were initially developed for use as infra red/visible/ultra-violet photon detectors. By careful adjustment of the p-type layer thickness, n^+-type layer thickness and dopant concentrations it is possible to tailor the spectral and frequency response to particular applications. In this work photodiodes manufactured by Integrated Photomatrix (IPL) type IPL10050CW were selected as they offered a larger active area. For reasons of commercial confidentially the manufacture would not disclose detailed architecture or dopant specifications. Physical and electrical characteristics, taken from the manufacturers data sheets [5.5] of these devices are given in Table 5.1. A photograph of the photodiode as supplied is shown in Figure 5.6 together with packaging details.

Table 5.1 Characteristics of PIN photodiodes studied

Device	Active Area (mm^2)	Maximum Reverse Bias (volts)	Dark Current (pA)	Capacitance (pF)	Calculated depletion layer thickness from Equation 5.1 (μm)
IPL10050CW	41.3	60	420 $V_R = 40$	65 $V_R = 40$	68 $V_R = 40$

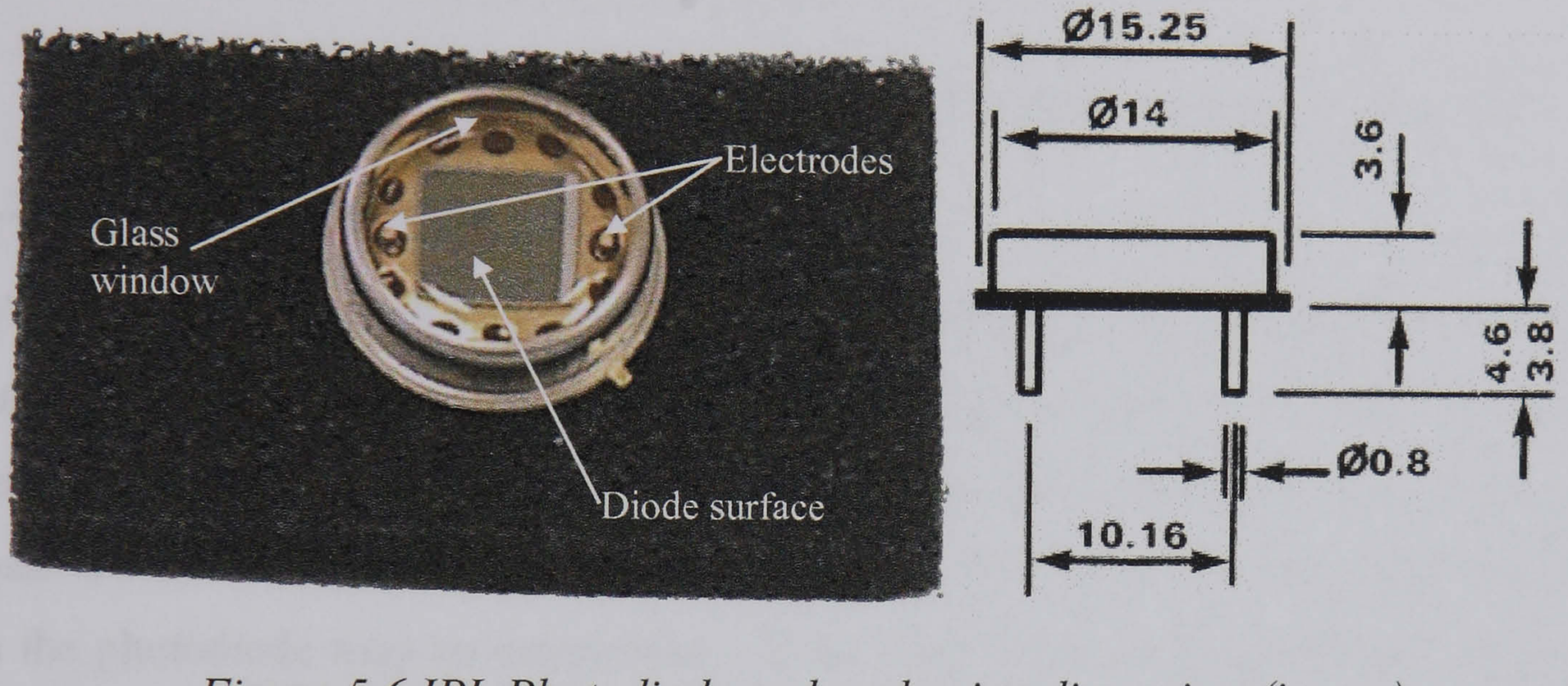

Figure 5.6 IPL Photodiode and packaging dimensions(in mm)

5.2.2 Principle of Detection

5.2.2.1 Photons

When sufficiently energetic photons of light are incident on the diode surface electrons are excited from the valence band up into the conduction leaving holes in the valence band. These electron hole (e^--h^+) pairs will be produced throughout the diode up to the maximum range of the photons and secondary photoelectrons. In the electric field induced within the depletion layer these e^--h^+ pairs will become separated, the electrons will tend to drift towards the n-type layer and the holes will drift towards the p-type layer. A similar mechanism will operate for e^--h^+ generated in the p and n-type layers. The net effect will be to accumulate a positive charge in the p-type layer and a negative charge in the n-type layer. The amount of charge generated will be proportional to the ionisation induced by the incident photons and the intensity. This mechanism is shown schematically in Figure 5.7.

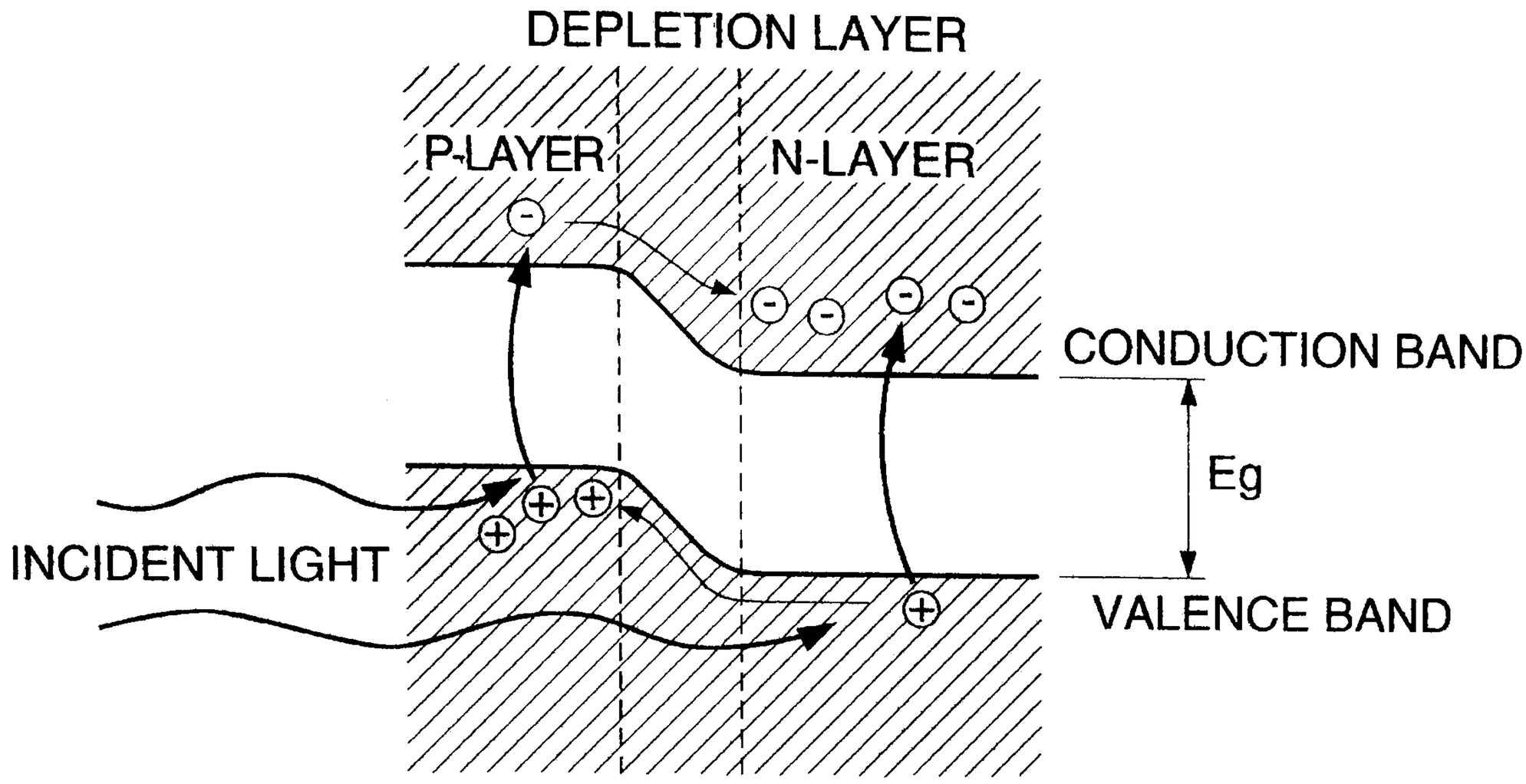

Figure 5.7 Principle of operation of a p-n photodiode redrawn from [5.1]

5.2.2.2 Charged particles

When charged particles such as protons, alphas and tritons are incident upon the diode surface e^--h^+ pairs will be generated along the length of their track. The number of pairs generated is independent of the particle type and depends solely on the energy loss. Therefore, by detecting the induced charge, the energy loss the particle suffered in the photodiode may be determined. If the depletion layer is sufficiently thick that the particle is completely stopped the total energy of that particle may be determined. A number of authors describe the use of photodiodes for charged particle spectroscopy. Gooda et al [5.6] describes the detection of alpha particles using a small area photodiode and conventional counting electronics. Honsono et al [5.7] discussed the detection of recoil protons originating from fast neutron interactions in a polyethylene converter. More exotic applications have included heavy ion detection and identification [5.8].

The detection of thermal neutrons using PIN photodiodes can be achieved by applying a suitable charged particle converter to the front surface of the diode. Previously, see Chapter 4, lithium charged particle converters were examined for use with dRAMs. The availability of enriched ^{6}LiF and the previous experience of successfully producing thin films by vacuum evaporation lead these to be adopted for use with the PIN photodiodes.

Although no external bias need be applied to a photodiode for it to detect charged particles, the internal electric field within the depletion layer is sufficient to separate

the e^--h^+ pairs, by applying a reverse bias the width of the depletion layer can be increased. Operation with a reverse bias is beneficial for two reasons. The un-biased depletion layer is unlikely to be sufficiently thick to fully stop energetic particles, by increasing the reverse bias the depletion layer width is enhanced. And secondly as the reverse bias is increased the capacitance of the junction will be reduced. Since for a large part the electrical noise generated by the photodiode is proportional to its capacitance a reduction will allow the detection of low energy particles which would otherwise be 'lost' in the electrical noise. If the reverse bias is sufficient that the depletion layer extends throughout the whole thickness of the n-type substrate the detector is said to be fully depleted. Any further increase in the reverse bias will intensify the electric field within the diode until eventually a destructive breakdown will occur.

Recalling from Chapter 1 the range of alpha, triton and lithium recoils generated by the (n,α) reaction with ^{6}Li (see Table 1.4) it may be seen that for the IPL photodiode with a reverse bias of 40 volts the depletion layer will be sufficiently thick to stop all of the generated particles. The longest-range reaction product is the triton, which has a maximum range of 41.6 μm, compared to the calculated depletion layer thickness of 68 μm (see Table 5.1). Therefore, for all measurements the photodiode was operated with a reverse bias of 40 volts as specified by the manufacturer.

5.3 Experimental Study of IPL Photodiodes

5.3.1 Neutron Detection

Three IPL photodiodes were obtained through RS Components Ltd (stock nos. 651-995) and the front glass window removed by carefully cutting the packaging using a diamond-slitting saw. Prior to this process the dark current was recorded and then re-measured after the de-encapsulation. It was noted that a substantial increase, at least a four fold, in dark current occurred. However, when the diodes where cleaned in analytical grade acetone and dried in a laboratory desiccator the dark current then returned almost to the previous value. It is believed that this temporary increase could be attributed to the small quantity of demineralised water that was used to lubricate and clear the diamond-slitting saw. A photograph of a de-encapsulated photodiode is shown in Figure 5.8.

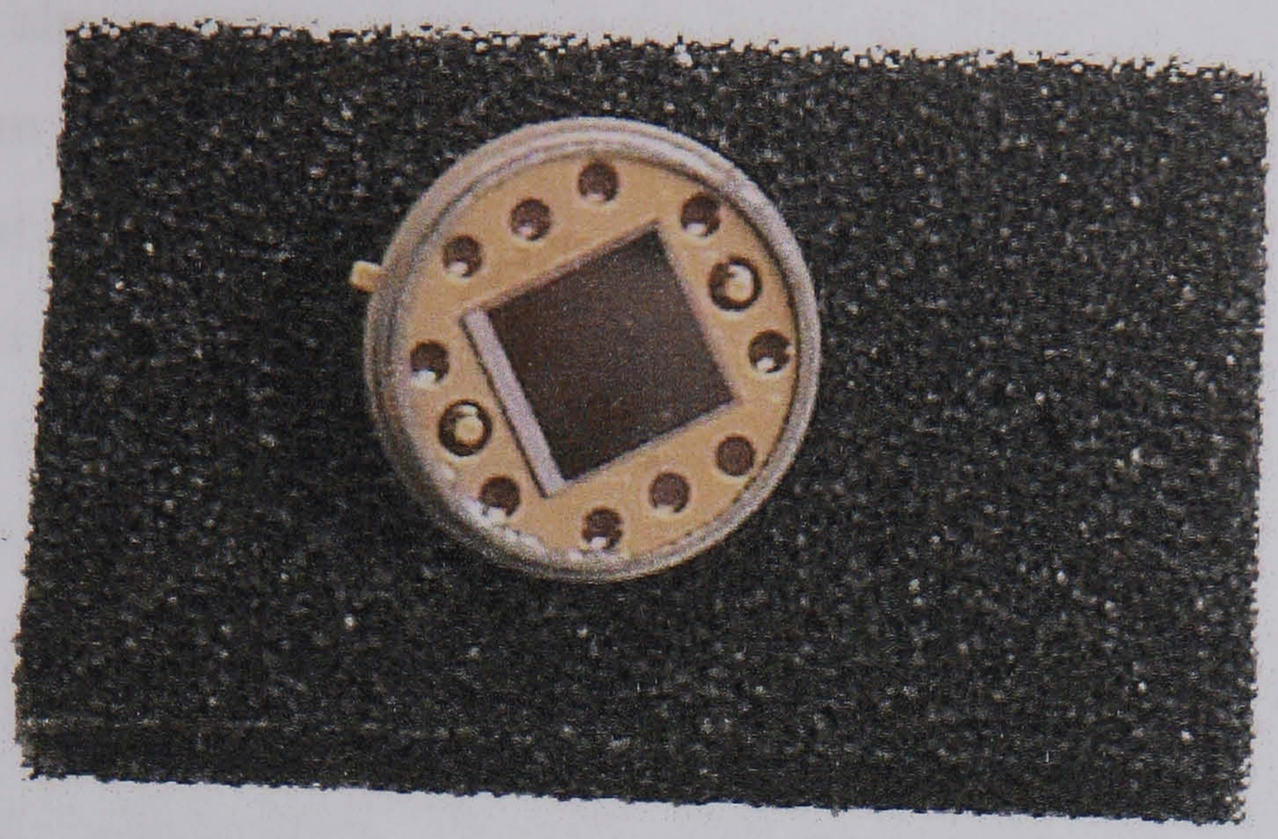

Figure 5.8 De-encapsulated IPL Photodiode

Using thin aluminium foil a mask was prepared which protected the gold bond wires leading from the diode surface to the external electrode connections. All three masked diodes were then mounted on a rotating stage suitable for use in an Edward vacuum evaporator unit, as described in Chapter 4, and positioned approximately 7 cm from the molybdenum boat. The previously described resonating quartz crystal film thickness monitor was again used to determine the evaporated film thickness. A coating of 95% enriched ^{6}LiF was then deposited onto the diode's surface with a measured thickness of (5.0 ± 0.5) μm. To protect the coating, bond wires and to provide mechanical strength a layer of low melting point polyethylene 'glue' was carefully deposited onto the diodes surfaces so that it filled the metal casing of the diode. A photograph of a completed photodiode is shown in Figure 5.9.

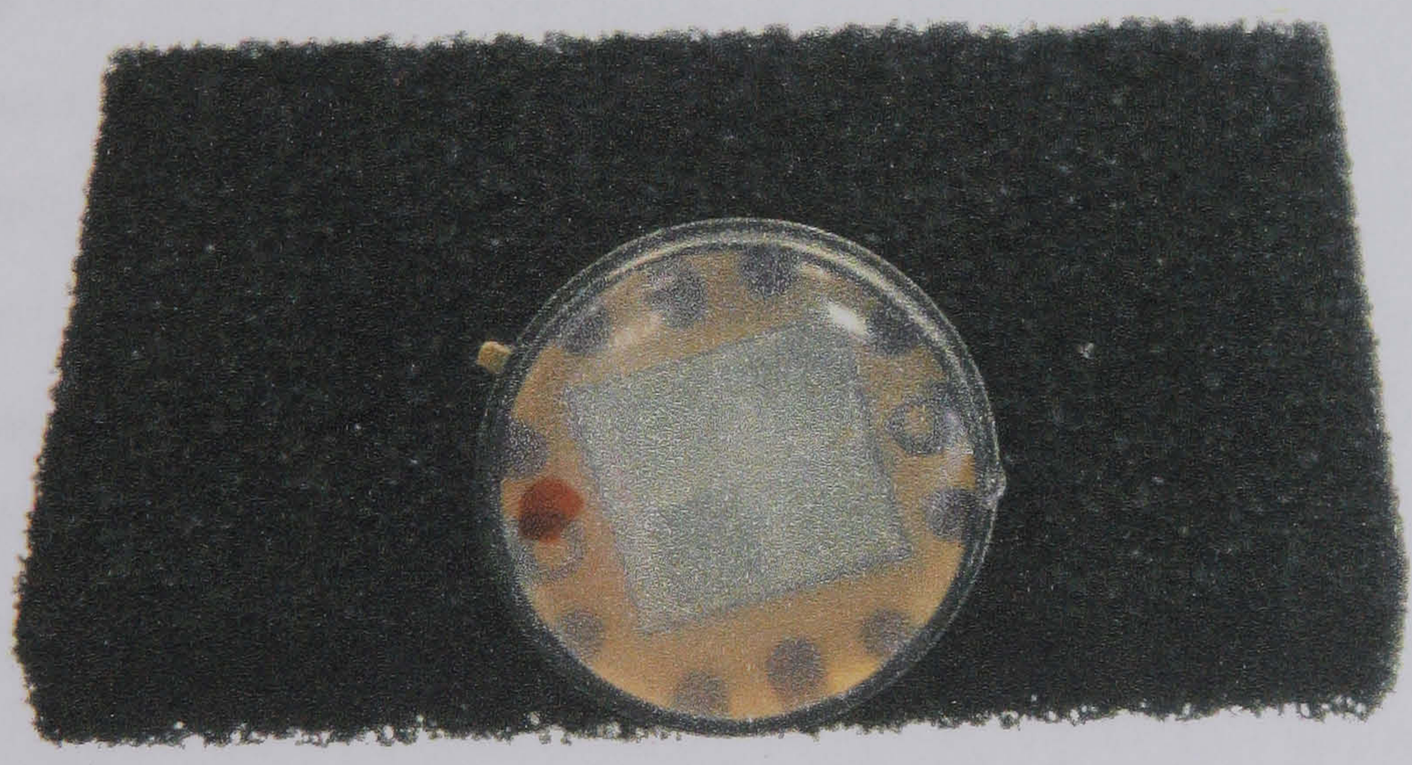

Figure 5.9 Coated and polyethylene encapsulated photodiode

As has been noted photodiodes are light sensitive and therefore a packaging was required which would exclude daylight. Conveniently thin walled (≈ 0.5 mm) 25 mm diameter pure aluminium tubing was available. Such packing would not only exclude

light but would also provide good electrical screening. Polyethylene plugs (25 mm diameter, 10 mm thick) were produced and machined with a recess such that the photodiode fitted closely inside the plugs. Low noise screened co-axial cable was used to provide a lead out from the photodiode electrodes, a connection from the outer aluminium case to the screening of the cable was also made to ensure good electrical screening. A photograph of this assembly is shown in Figure 5.10.

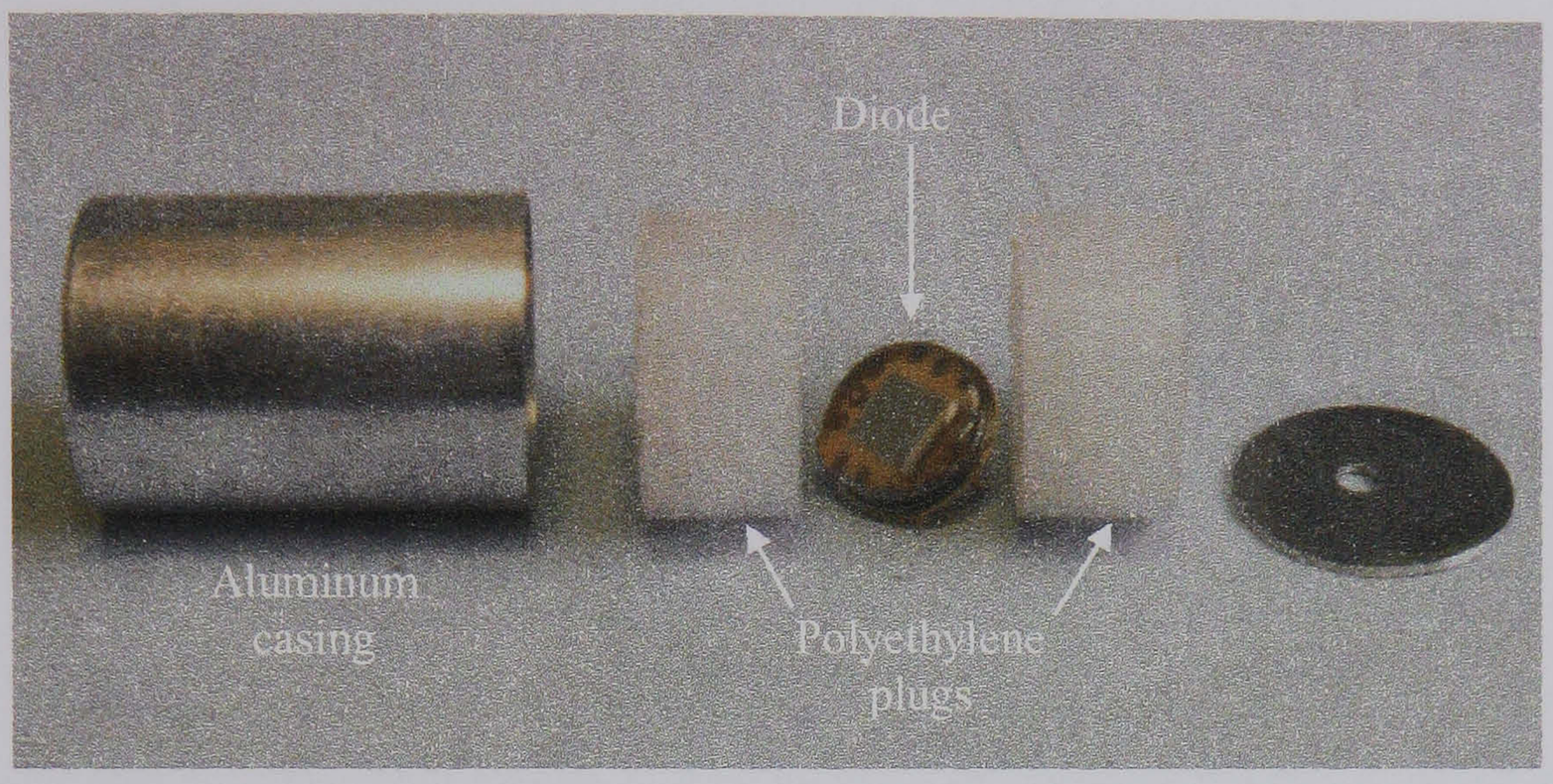

Figure 5.10 Packaging of photodiode

The output from the photodiode was taken via a Canberra pre-amplifier (model 2004) and a Canberra amplifier (model 2011) to an EG&G mult-channel analyser PC card. The counting electronics are shown schematically in Figure 5.11. Pulse height spectra were recorded and analysed using the EG&G program Maestro. Pulse height spectra were recorded in four conditions for each of the three-photodiode assemblies, hence referred to as D1, D2 and D3. Firstly a long background count (≈ 5 hours) with no sources present, secondly with a ^{60}Co source positioned such that a dose rate (measured with a Nuclear Instruments PDR2) at the photodiode position was 200 μSv h^{-1}. Thirdly, with a 3.7×10^{10} Bq ^{241}Am/Be source positioned on top of the aluminium packaging and finally with an additional 1 mm cadmium thick cadmium cover over the photodiode assembly A typical pulse height spectrum with the ^{241}Am/Be source in place is shown in Figure 5.12.

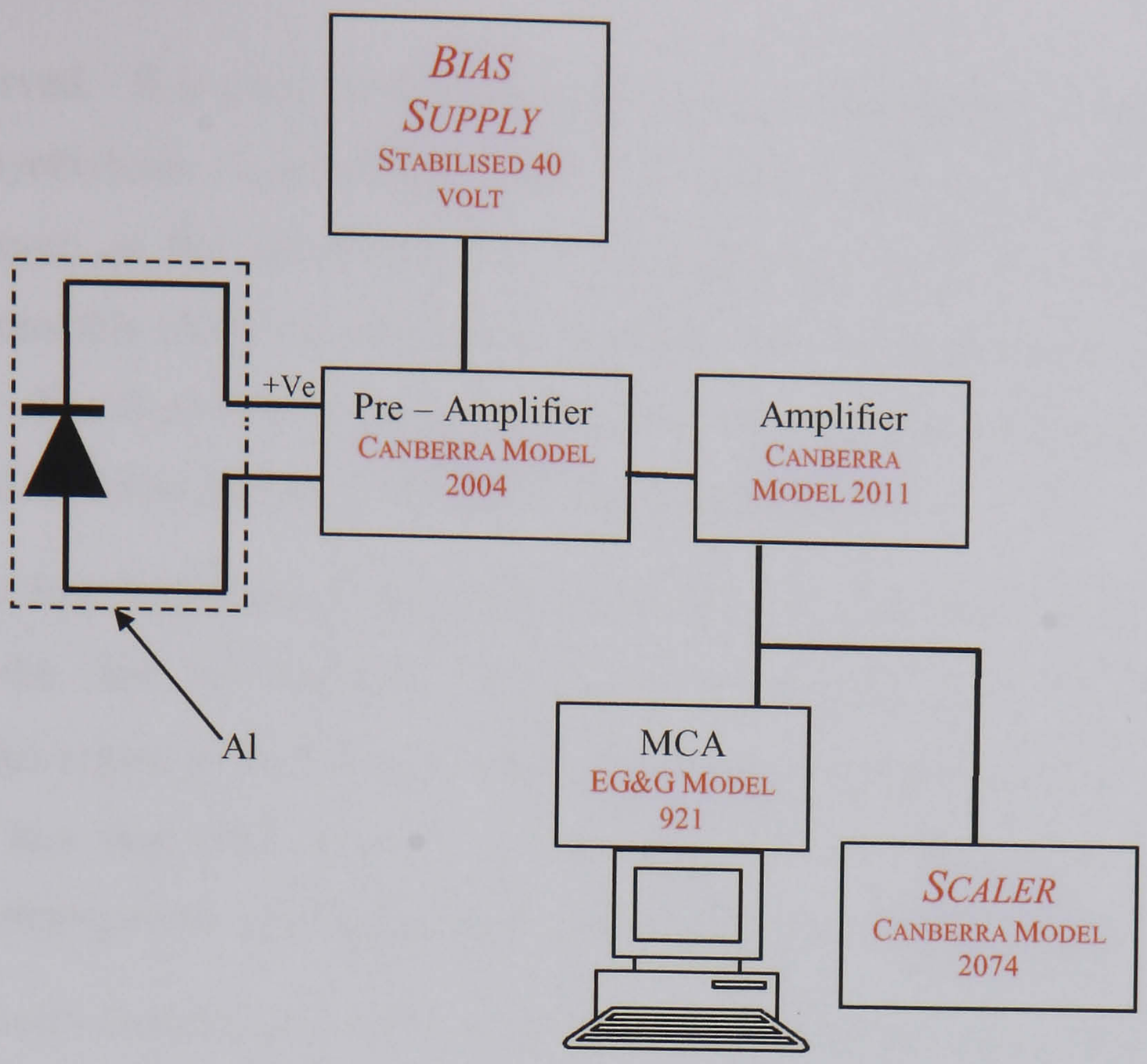

Figure 5.11 Schematic of photodiode counting electronics

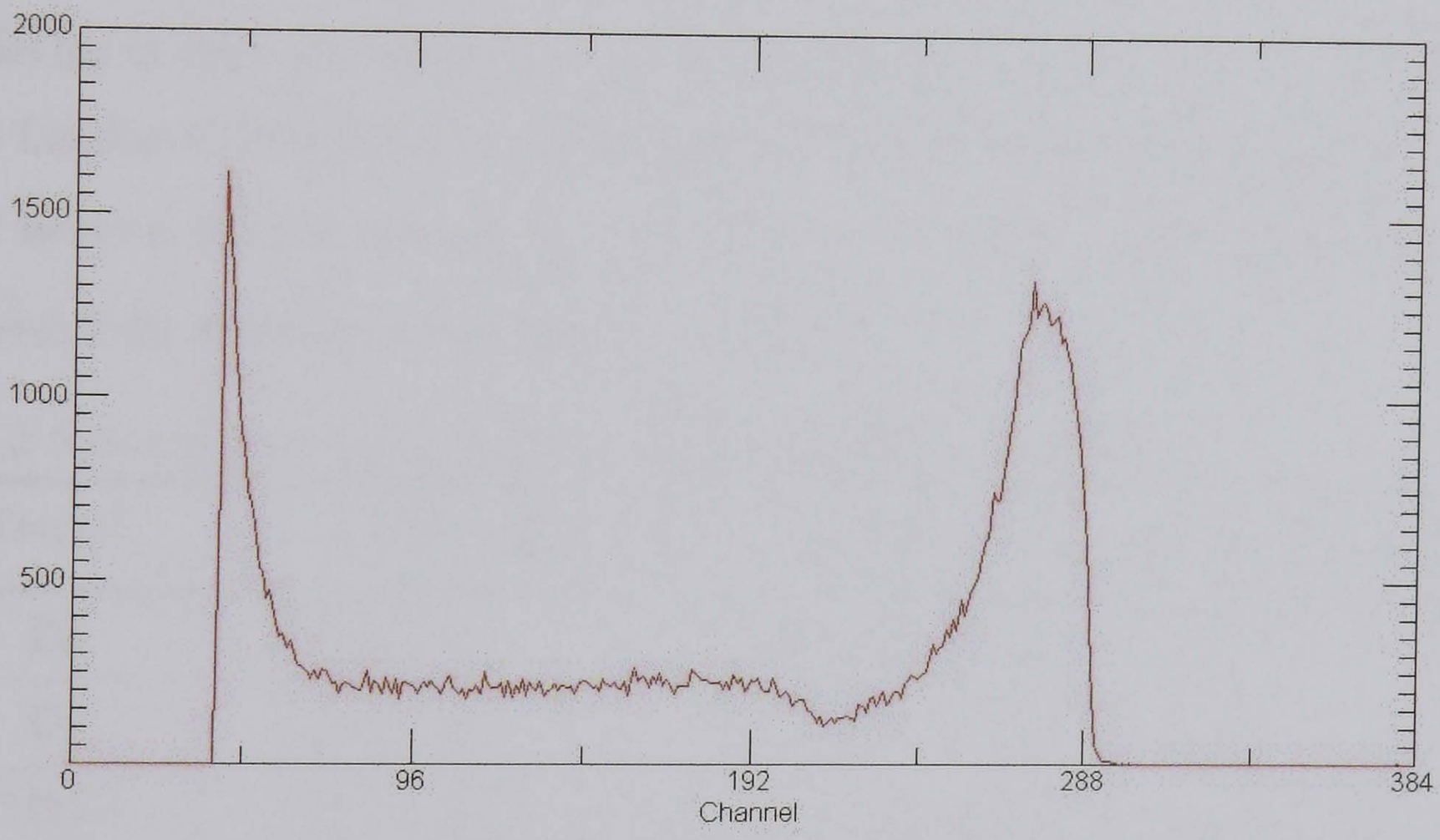

Figure 5.12 Typical pulse height spectrum from a neutron irradiated photodiode

Three features were observed in all of the neutron irradiated photodiode spectra. Firstly, a low energy background due predominately to electronic noise and energy deposited by gamma rays within the thin depletion layer of the device. Secondly, a continuum region, which was initially attributed to either alphas or tritons originating from deep within the ^{6}LiF converter layer and thus having suffered large energy losses. However, when another IPL photodiode with a ^{6}LiF coating but without the encapsulating polyethylene 'glue' was exposed to the ^{241}Am/Be source this region

was not observed. It is possible that this region can be attributed to proton recoils from the polyethylene encapsulation that is in intimate contact with the device surface, however, as the requirement of the photodiodes was for the detection of thermal neutrons this effect was not further studied. This effect has been observed by Hosono [5.7]. The third feature was a broad peak in the spectra, which was attributed to the 2.728 MeV triton and the 2.055 MeV alpha particle.

In the source free background spectrum, collected for 5 hours, counts were only observed in the first 20 channels, whilst with a 200 μSv h^{-1} ^{60}Co gamma ray background this region extended up to channel 45. All photodiodes had a background count rate of less than 0.02 counts s^{-1}. When neutron irradiated under a cadmium cover only a small gamma ray background region was observed up to channel 40.

The EG&G multi-channel analyser was replaced by a Canberra scalar (model 2074). Using a precision pulser the lower level discriminator was set such that only pulses with an amplitude corresponding to channel 50 or higher would be counted.

Each device in turn was exposed to the neutron beam at the 0° face of the Imperial College London CONSORT II to determine the neutron detection of efficiency. The thermal neutron fluence rate of $\dot{\Phi}_{th} = (5.9 \pm 1.2) \times 10^4$ cm^{-2} s^{-1} was determined using manganese foils; these results are given in Table 5.2.

Table 5.2 Neutron detection efficiencies for coated IPL photodiodes

Device	Count rate (C) s^{-1}	Neutron sensitivity ($C/\dot{\Phi}_{th}$) cm^2
D1	17.8 ± 0.2	$(3.0 \pm 0.6) \times 10^{-4}$
D2	15.5 ± 0.2	$(2.6 \pm 0.5) \times 10^{-4}$
D3	19.2 ± 0.2	$(3.3 \pm 0.6) \times 10^{-4}$

5.4 Discussion and Conclusions

5.4.1 Discussion

A simple estimate of the theoretical sensitivity to thermal neutrons can be made if a number of simplifying assumptions are made. If it is assumed that the entire active area of the diode is uniformly coated with a 5 μm thick layer of lithium fluoride and that the thermal neutron fluence rate is constant throughout the converter it is possible to calculated the $^6Li(n,\alpha)$ reaction rate, Equations 5.2, 5.3.

Total number of ^{6}Li atoms in converter layer = $N = \frac{0.95 \rho t A N_A}{M_A}$ *Equation 5.2*

where, t – thickness of converter layer

A – surface area of photodiode active area

N_A – Avogadro constant

M_A – Atomic mass of 95% enriched ^{6}LiF

Reaction rate for ^{6}Li(n,α) = $R = N\sigma_{^{6}Li}\dot{\Phi}_{th}$ *Equation 5.3*

where, $\sigma_{^{6}Li}$ - microscopic ^{6}Li(n, α) cross section

$\dot{\Phi}_{th}$ - thermal neutron fluence rate

Using Equation 5.2 and 5.3 the predicted ^{6}Li(n,α) reaction rate when irradiated in the CONSORT 0° beam would be 6.91 s^{-1}. When each ^{6}Li(n,α) reaction occurs two potentially detectable particles are produced (i.e. the alpha and the triton), hence, the total charged particle production rate in the converter will be twice the ^{6}Li(n,α) reaction rate. As this reaction essentially occurs at rest, the incident neutron energy is considerably less than the Q-value of the reaction, the charged particle products will be emitted isotropically into 4π sterdian. It is reasonable to assume that the converter/diode arrangement represents almost perfect 2π geometry and that as the depletion layer is thick compared to the particle ranges that the intrinsic efficiency is 100%. Therefore, theoretical count rate C_T from the photodiode will be given by Equation 5.4.

$$C_T = 2R\varepsilon = 2R(\varepsilon_i \varepsilon_g) = 2R\left(2\pi/4\pi\right) = R \qquad \textit{Equation 5.4}$$

where, R - ^{6}Li(n,α) reaction rate

ε_i – intrinsic efficiency, assumed to equal 1.

ε_g – geometric efficiency

The predicted count rate C_T for diodes irradiated in the CONSORT 0° beam is therefore 6.91 s^{-1}. This value is in reasonable agreement with the experimentally observed values, Table 5.2.

Irradiation of an un-coated photodiode confirmed that neutron detection through captures in the boron doping of the p-type layer was not feasible. Although no precise

data was available from the manufacturer typical boron doping concentrations are in the range 10^{15} atoms cm^{-3}. The predicted reaction rate for $^{10}B(n,\alpha)$ captures in a photodiode exposed in the CONSORT 0° beam would be approximately 10^{-8} s^{-1}. However, irradiation of an un-coated photodiode demonstrated that they were sensitive to fast neutron induced proton recoils from a hydrogenous converter (i.e. the polyethylene glue used to encapsulate). Although not pursued further this mechanism could be applied to produce a small personal active neutron dosemeter provided adequate sensitivity could be achieved. Harvey [5.9] proposed such a system a demonstrated that it would well match the requirements for a neutron personal dosemeter.

5.4.2 Conclusion

This study has demonstrated that IPL photodiodes are sensitive to low energy alpha particles and that they can be sensitised to the thermal neutrons using an external lithium fluoride converter. The measured sensitivity for neutrons indicates that neutron detection is both practicable and feasible for the typical fluence rates expected in operational use of the AAND. Additionally, the associated counting and bias electronics required for photodiodes were considerable simpler than those necessary to address a dRAM. Lithium fluoride PIN photodiodes were therefore adopted as the outer thermal neutron detectors in the active area neutron dosemeter.

5.5 – References for Chapter 5

[5.1] Davies A.H., **Semiconductor Physics**, London, Pergamon Press, 1987.

[5.2] Knoll G.F., **Radiation Detection and Measurement**, 2nd ed., Chichester: John Wiley & Sons, 1989.

[5.3] Lide D.R. Editor-in-Chief. **CRC Handbook of Chemistry and Physics 73rd Edition**, Boca Raton Florida: CRC Press, 1992.Knoll

[5.4] Hamatsu data sheet

[5.5] IPL data sheet

[5.6] Gooda P.H. and Gilboy W.B., High Resolution Alpha Spectroscopy with Low Cost Photodiodes, **Nucl. Instr. Meths. Phys. Res**., A255, 222, 1987.

[5.7] Honsono Y., SjafruddinIguchi, T., Nakazawa M., Fast Neutron Detector using PIN-type photodiodes, **Nucl. Instr. Meths. Phys. Res**., A361, 554, 1995.

[5.8] Motobayashi T., Particle Identification of Heavy Ions with Large Silicon Detectors, **Nucl. Instr. Meths. Phys. Res.**, A284, 526, 1989.

[5.9] Harvey S., **Charged Particle Induced Soft Errors in 1 Mbit and 4 Mbit dRAMs as the Basis for a Portable Radiation Detector System**, PhD thesis, University of Surrey, 1998.

Chapter 6 Construction and Experimental Verification of the AAND

This chapter describes the design and the experimental programme towards the development of a new active area neutron dosemeter with correction for the energy dependence of the incident neutron field. To achieve good sensitivity a central BF_3 neutron detector is used; its energy response has been shaped using a combination of concentric polyethylene moderators and a cadmium filter. To determine the energy dependence thermal neutron detectors are located within the moderator, their energy response being controlled by their depth within the moderator. The use of thermal detectors either on the surface of a moderating body or within it has previously been examined by a number of authors [6.1, 6.2].

The development of this device may conveniently be separated into three areas. Firstly the optimisation of the central detector, secondly the modelling of the outer detectors and finally the experimental programme.

6.1 Central Detector

A number of previous designs, discussed in Section 2.4, have utilised a central detector with concentric moderators and filters. In this design this arrangement has been retained. However, the optimisation of previous designs was limited by the relatively simple computational methods available. Monte Carlo modelling using MCNP 4b now provides the capability to further optimise these designs. Additionally, the neutron fluence to dose conversion coefficients have been revised on a number of occasions as discussed in Chapter 2. Therefore, in this work the optimisation of the central detector and its associated moderator/filter arrangement has been addressed.

The model developed using MCNP 4b is shown in Figure 6.1 and a sample input file is supplied at Appendix A. Exposure to a broad parallel beam, i.e. an expanded and aligned field was modelled by using a planar surface from which neutrons were emitted normally, this required an additional source surface to be specified. The AAND was aligned with the cylindrical axis of the device normal to the direction of the beam; as it is intended that in operational use the AAND will be held with the cylindrical axis vertical. The model was coded such that it was possible to vary the total radius R and the position of the filter r_1. A number of constraints were imposed,

most importantly that the total weight should not significantly exceed the at present preferred device a Leake type spherical dosemeter. Other restrictions included the practicality of machining the moderator and component availability i.e. the central BF_3 detector.

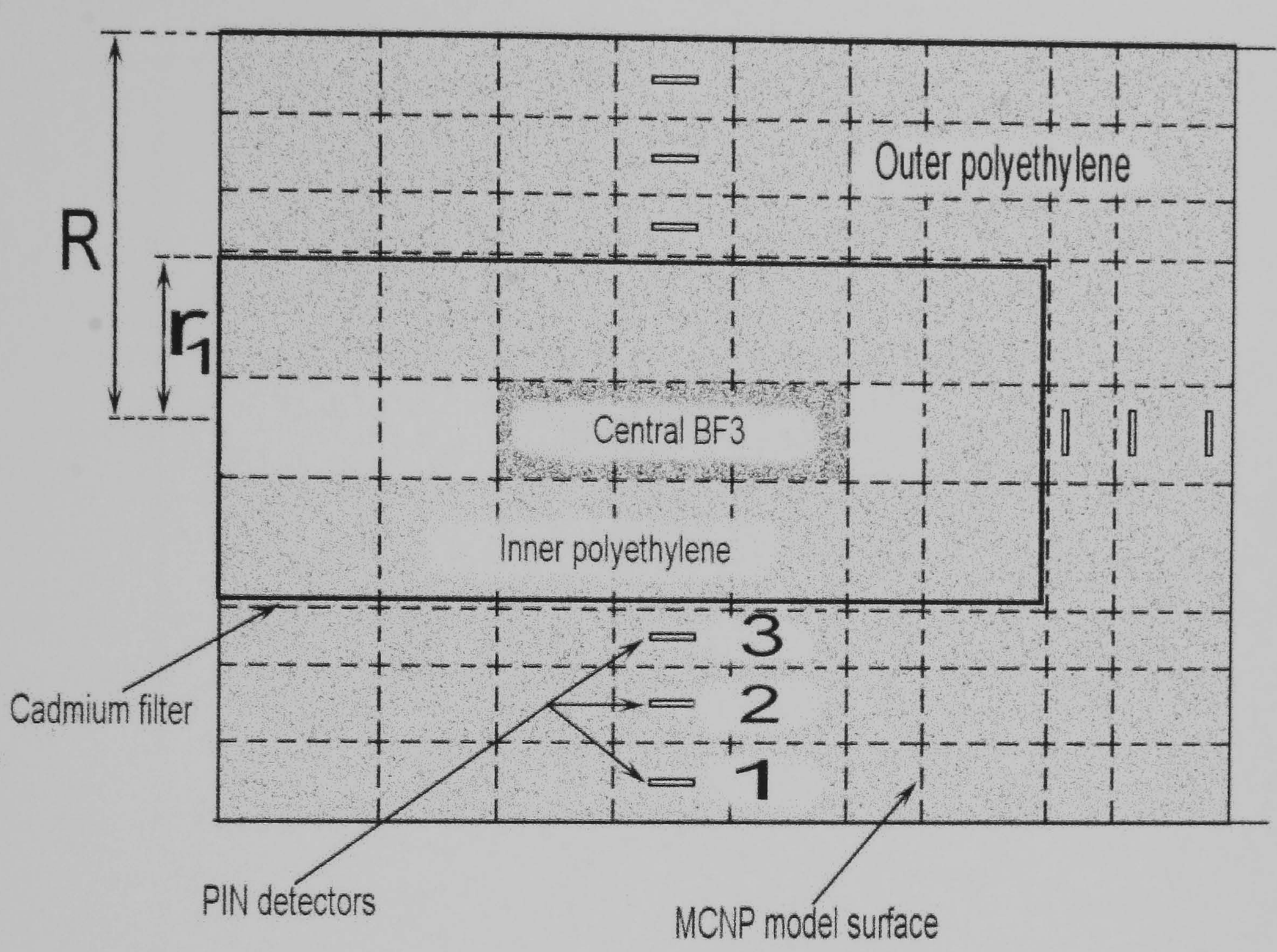

Figure 6.1 MCNP 4b model geometry

The MCNP track length fluence rate estimate tally F4 together with the ENDF/B-VI cross-section for the $^{10}B(n,\alpha)$ reaction were used to determine the reaction rate for 22 mono-energetic neutron fields. It was then assumed that the pulse output of a BF_3 detector would be proportional to this reaction rate. The aim of the optimisation was to achieve the best fit to the energy dependent dose to fluence conversion coefficients as published in ICRP74 by varying the parameters R, r_1.

The final simulated energy response for R = 10.5 cm and r_1 = 3.8 cm is shown in Figure 6.2 along with the ideal response as required by ICRP74. The over-response in the low energy region and the under-response at higher energies, identified in previous similar designs, is still present. It is these deficiencies that require spectral

correction to be applied when the device is operated in varying neutron energy spectra.

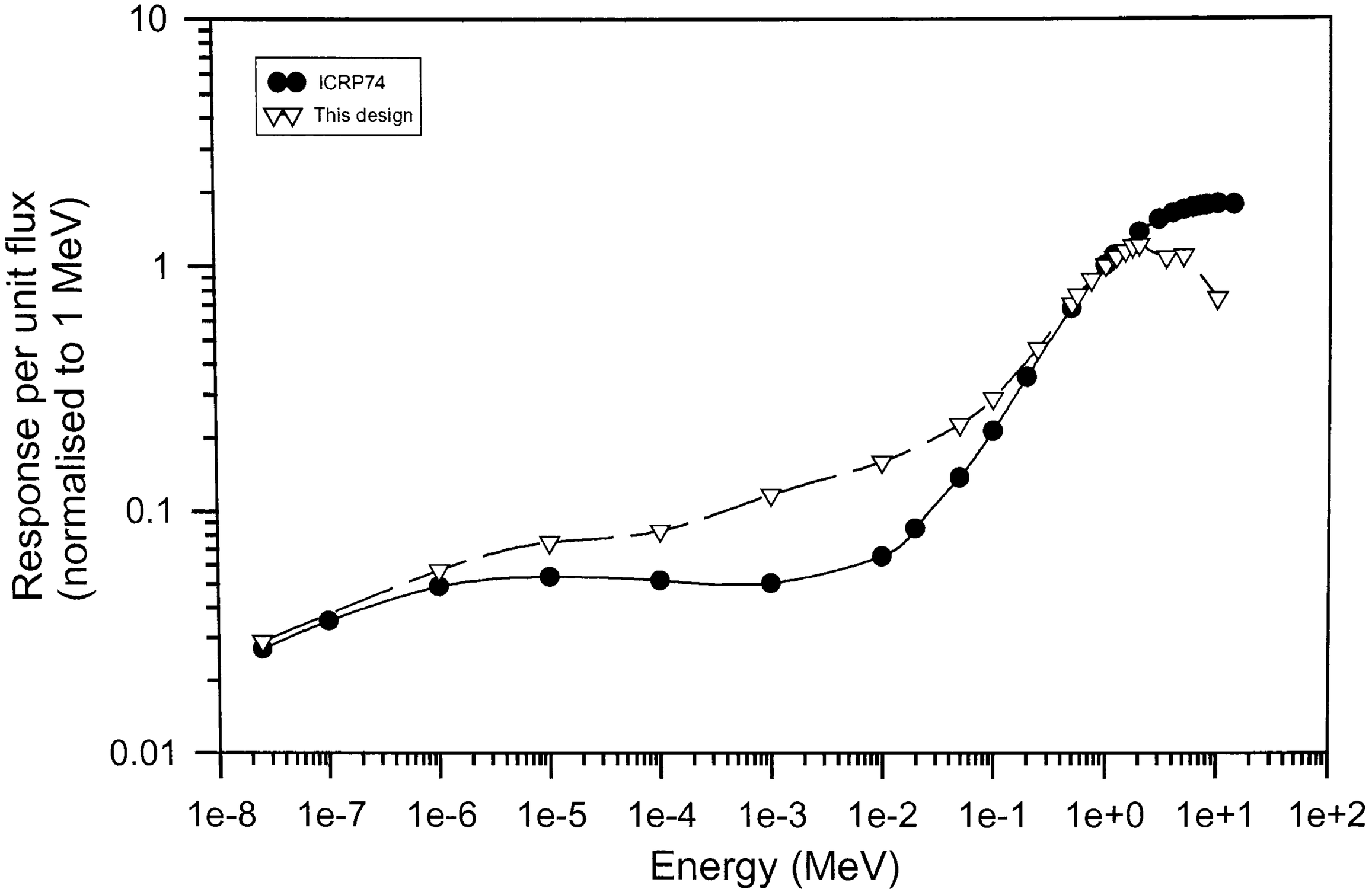

Figure 6.2 Energy response of central detector

6.2 MCNP Modelling of Outer Detectors

Previously Piesch [6.2] described a methodology for neutron radiation field characterisation using a number of shielded thermo-luminescent detectors located on the surface and within a large moderating sphere, for a fuller discussion of this method see Section 6.4.

The MCNP model referred to earlier was modified to include four sets of three LiF tally regions, shown in Figure 6.1. Four of these sets were positioned orthogonally around the cylindrical axis; all detectors were located outside of the cadmium filter. An F4 tally was used but now using the ENDF/B-VI cross-section for the $^{6}Li(n,\alpha)$ reaction. Again it was assumed that the response of the PIN would be proportional to this reaction rate.

The energy responses of the PINs were determined with them positioned at varying depths within the moderator. The aim was to determine three suitable positions for these detectors, which would produce three distinct, but overlapping energy responses. A linear superposition of these three detectors could then be taken, in a similar way to Piesch et al. [6.2], and the field characteristics could be derived.

The final working design shown in Figure 6.1 represents the most practicable design for manufacture. The shallowest detector D1 is positioned 2.2 cm below the surface; D2 is positioned at a depth of 3.4 cm with the deepest diode D3 positioned 4.6 cm below the surface. The modelled energy responses for this arrangement are shown in Figure 6.3. As may be seen detector 1 (D1), the shallowest, responds predominately below 1 keV whilst detector 3 (D3), the deepest, peaks at approximately 1 MeV. Detector 2 (D2) located between D1 and D3 has a relatively uniform response between 10 eV and 2 MeV. Piesch et al. [6.3] used similar responses in their earlier passive methodology and so these final positions were considered acceptable.

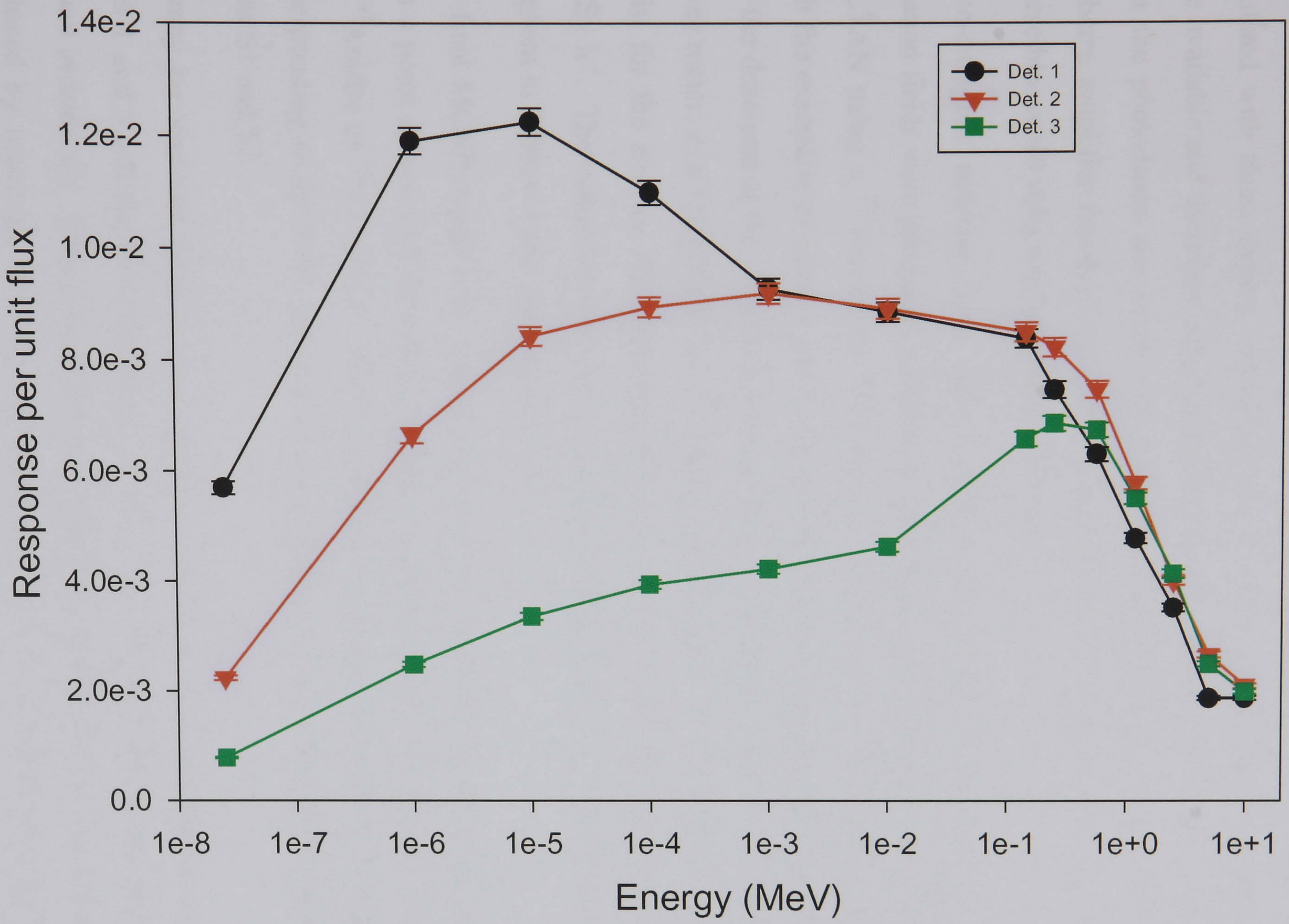

Figure 6.3 Energy responses of PIN detectors

6.3 Initial Experimental Verification with Isotopic Sources

A suitably machined polyethylene cylinder was produced which accepted the inner BF_3 with its associated cadmium filter and provided four channels into which alternating polyethylene discs and PIN detectors could be mounted, shown in Figure 6.4 and 6.5. In the proposed final design all of the four radial diode channels would be populated with three diodes. However, for the initial prototype only three diodes were available and therefore only one radial channel was fully populated. The output from the photodiode was taken via a Canberra pre-amplifier (model 2004) and a Canberra amplifier (model 2011) to a scalar counter, as discussed in Chapter 5; a reverse bias of 40 volts was applied to all diodes.

Mono-energetic neutron fields were initially not available; therefore, five neutron radiation fields were produced, detailed in Table 6.1, at the Nuclear Department HMS SULTAN using a ^{241}Am/Be or ^{252}Cf source either bare or with various shielding. With the exception of cases 4 and 5, the AAND was positioned within the field such that the dose-rate at the cylinder's front surface, as measured by a Mk7NRM neutron survey meter, was 150±10μSv h^{-1}. The dose rate using the ^{252}Cf source was 70μSv h^{-1} whilst for the heavily shielded polyethylene and steel ^{241}Am/Be the dose rate was 95μSv h^{-1}. The ratios between the outer PIN detectors (D1, D2 and D3) count rates are given in Table 6.1 and discussed below.

The final MCNP model was repeated but with the mono-energetic sources replaced with a point source with an energy distribution equivalent to that produced by either an ^{241}Am/Be or ^{252}Cf source. The ratios of the responses of the three LiF tally cells, corresponding to the PINs, were calculated and these results are also shown in Table 6.1 as S1 and S2.

As may be observed there is good agreement between the experimental results of cases 1 and 5 and the two simulations S1 and S5. It is likely that as the simulations did not include any of the room walls and ceiling the contribution of thermal neutrons produced by scattering from the surroundings will be under-estimated by MCNP. This effect would account for the slightly higher D1/D2 and D1/D3 ratios predicted by MCNP than were observed experimentally. The ratio D3/D2 appears to be relatively insensitive to variations in the energy spectrum; the two response functions are not sufficiently distinct for them to achieve good discrimination.

Considering cases 3 and 4 relative to the bare source (case 1); the energy spectrum in case 3 will be virtually identical to case 1 except that the thermal component will be removed. It is, therefore, expected that the ratios D1/D2 and D1/D3 for case 3 should decrease relative to the case 1. This is observed. Again, ratio D3/D2 was insensitive to this change in spectrum. Case 4, heavily shielded with polyethylene and steel, will significantly soften the energy spectrum and therefore it is predicted that the ratios D1/D2 and D1/D3 should increase relative to case 1. This is observed in the experimental results.

The remaining case proved of limited use, as the thickness of polyethylene used was insufficient to significantly increase the thermal component. Earlier MCNP simulations had suggested that this thickness should be adequate but as previously discussed the effect of scatter from the surroundings (i.e. walls and ceiling) had not been considered.

In conclusion, the data in Table 6.1 indicates that the arrangement of PINs within the moderating body is capable of discriminating differing energy spectra. The agreement between experimental results (cases 1 and 5) to MCNP derived results (cases S1 and S5) adequately demonstrates the usefulness of the present model as a design tool.

Table 6.1 – PIN detector responses to various neutron radiation fields

Nos.	Description	Ratio of detector response $\pm 2\sigma$		
		D1/D2	D1/D3	D3/D2
1	Bare ^{241}Am/Be	0.67 ± 0.02	0.82 ± 0.02	0.81 ± 0.03
S1	MCNP simulated Bare ^{241}Am/Be	0.68 ± 0.06	0.88 ± 0.07	0.80 ± 0.06
2	^{241}Am/Be + 25 mm polyethylene	0.65 ± 0.02	0.81 ± 0.03	0.81 ± 0.03
3	^{241}Am/Be + 1 mm cadmium	0.60 ± 0.02	0.69 ± 0.02	0.87 ± 0.03
4	^{241}Am/Be + 85 mm polyethylene + 50mm steel	0.81 ± 0.02	0.94 ± 0.02	0.86 ± 0.03
5	Bare ^{252}Cf	0.58 ± 0.02	0.71 ± 0.03	0.82 ± 0.03
S5	MCNP simulated ^{252}Cf	0.60 ± 0.03	0.73 ± 0.04	0.79 ± 0.03

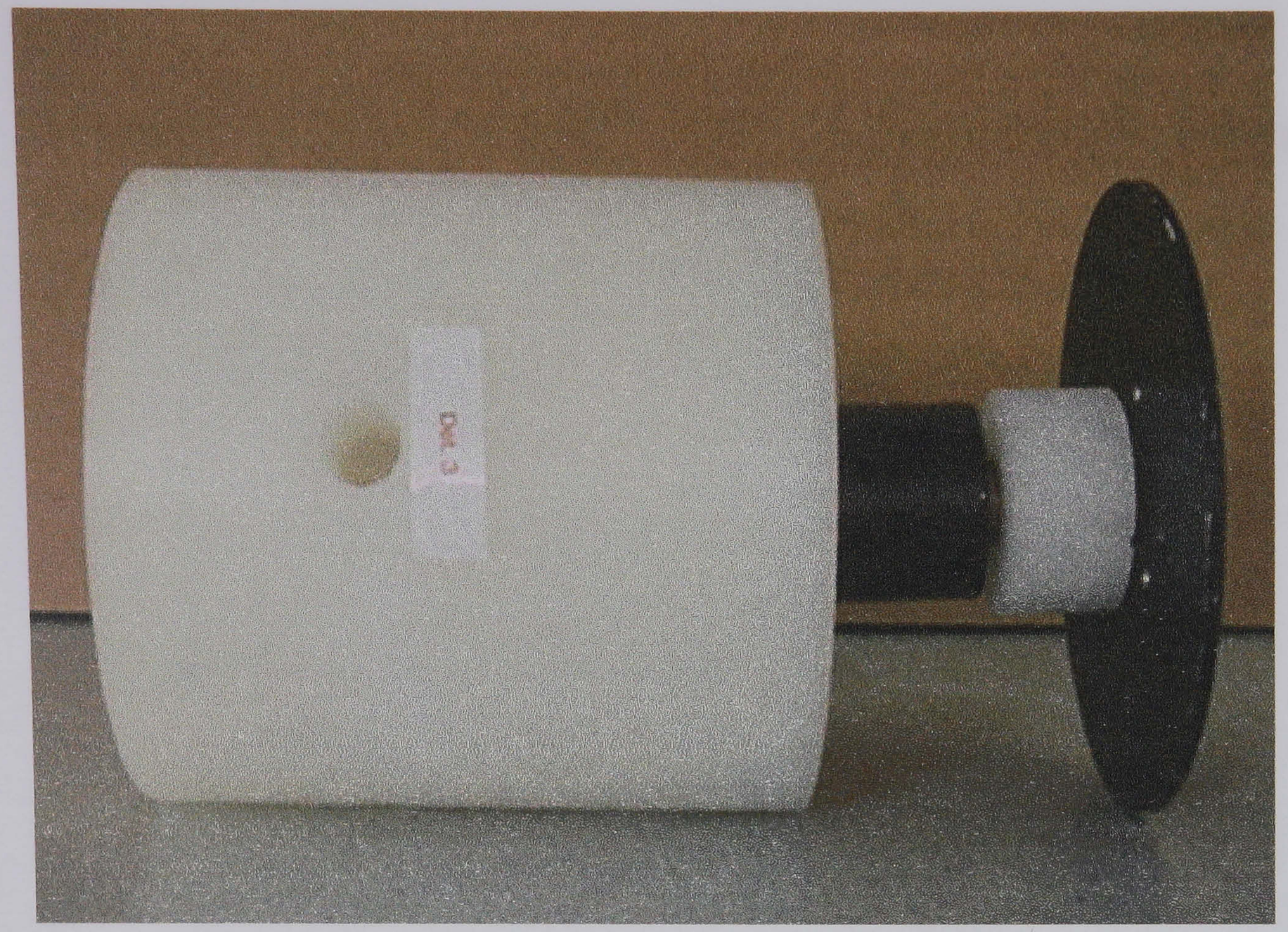

Figure 6.4 AAND Moderator and central BF_3

Figure 6.5 Photodiode assembly

6.4 Verification of Modelled Responses Using Mono-energetic Neutrons

Subsequent to this successful demonstration of the AAND an experimental validation of the MCNP modelled detector response functions was conducted. This work was conducted at the National Physical Laboratory in the low scatter (25m × 18m × 18m) facility. Mono-energetic neutrons are available at the 6 ISO recommend energies of 144, 250, 565, 1200, 2500, 5000 keV. Scatter correction was performed using the shadow cone technique and the 'true' fluence rate was measured using the NPL long counter. The experimental arrangement is shown in Figure 6.6.

At each of the six energies the AAND was positioned at four orientations relative to the neutron-producing target, as shown in Figure 6.7.

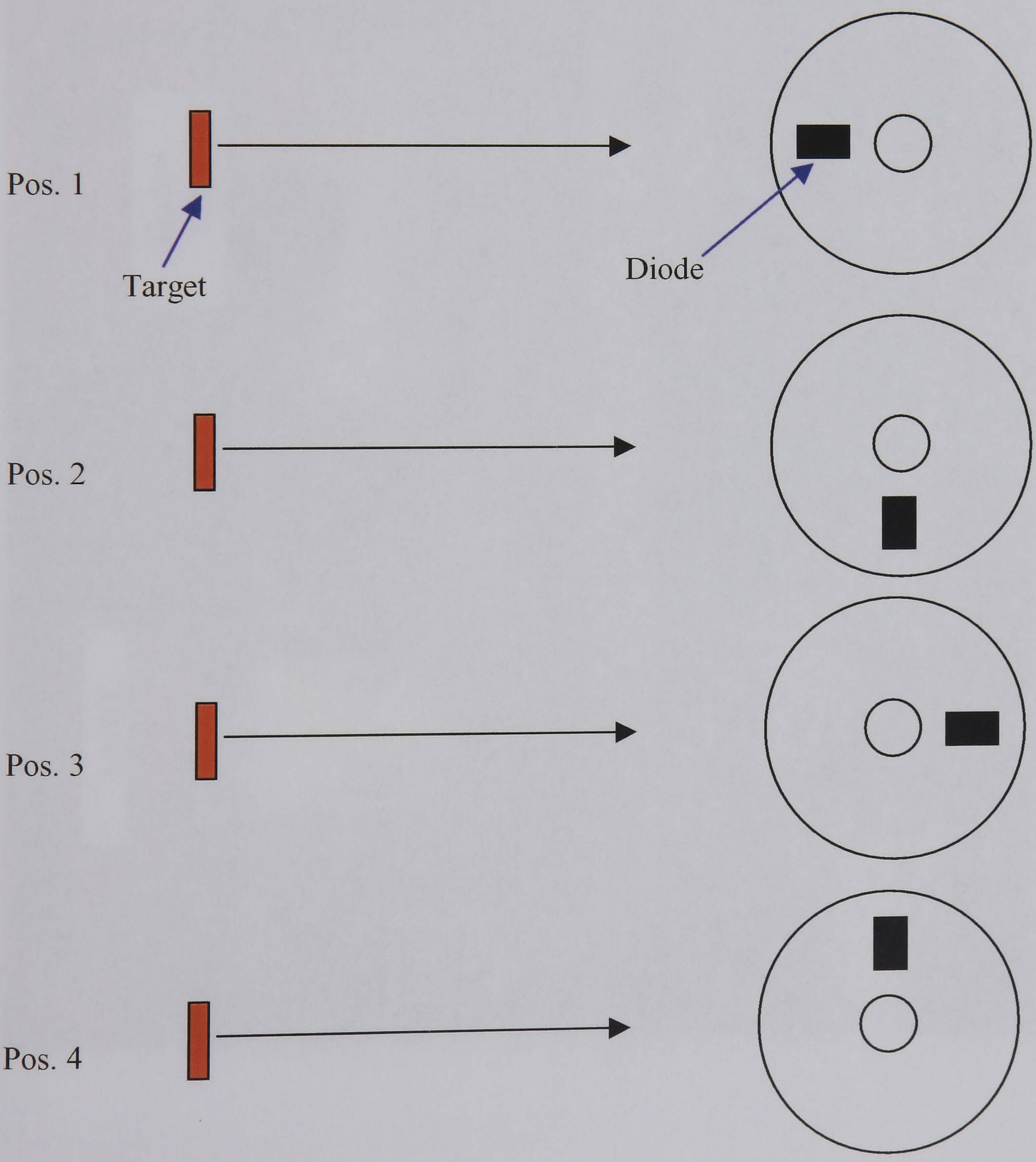

Figure 6.6 Orientation of AAND relative to target

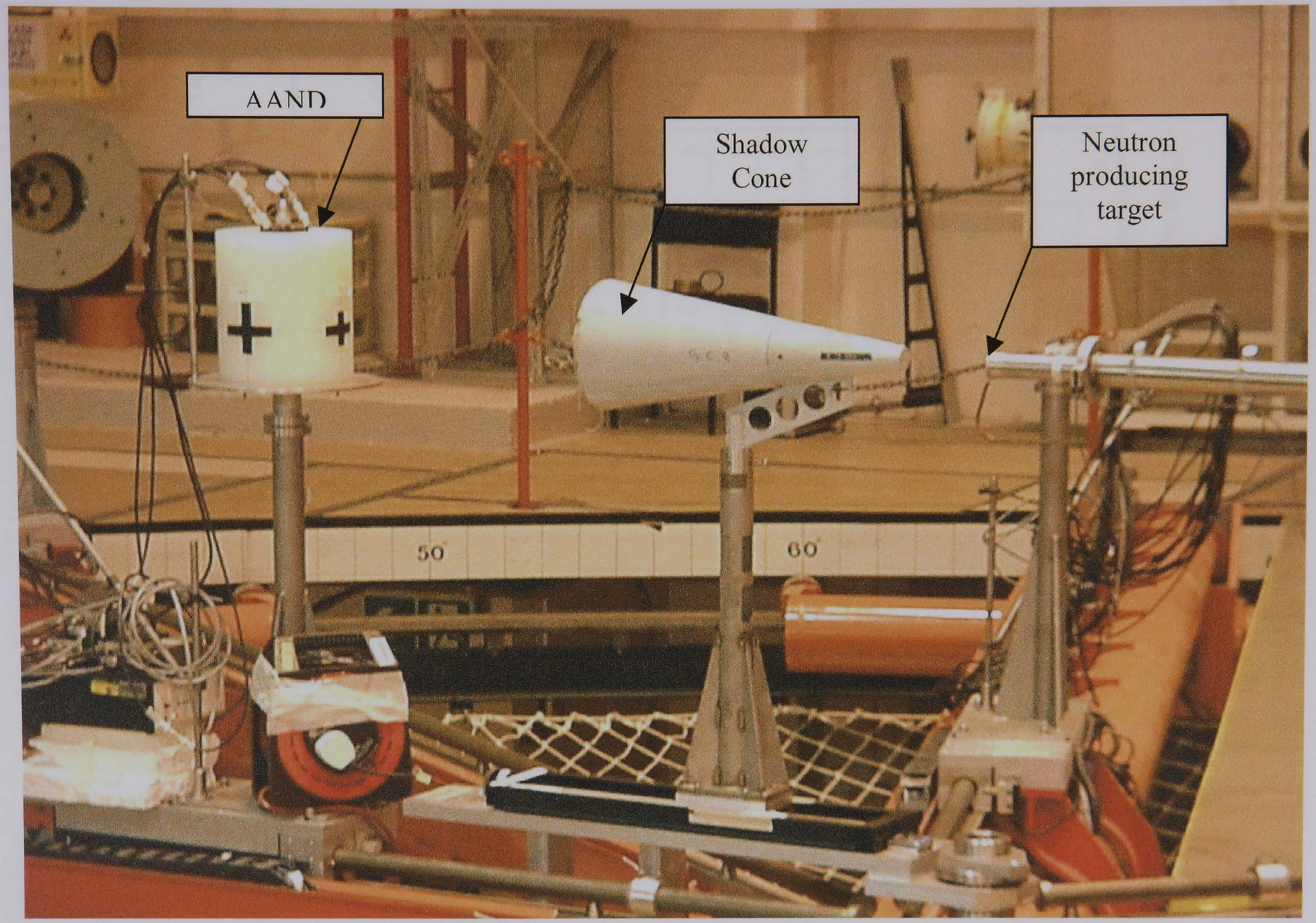

Figure 6.7 AAND in the low scatter facility at NPL

The results from position 1 may be directly compared to the MCNP predictions. Positions 2 and 4 are expected to yield identical count rates from the diode detectors as the diodes orientation relative to the neutron-producing target is simply rotated through 180. The response of each detector at all energies was recorded and the response in terms of counts per unit fluence rate determined and are given in Table 6.2.

Table 6.2 – Experimentally determined responses

Energy (keV)	Pos.	Experimental Response per unit fluence rate ± 2σ (cm^2)			
		BF_3	D1	D2	D3
144	1	$(2.9\pm0.3)\times10^{-2}$	$(6.6\pm0.7)\times10^{-3}$	$(7.5\pm0.8)\times10^{-3}$	$(6.3\pm0.6)\times10^{-3}$
	2	$(2.8\pm0.3)\times10^{-2}$	$(1.3\pm0.1)\times10^{-3}$	$(1.6\pm0.1)\times10^{-3}$	$(1.3\pm0.1)\times10^{-3}$
	3	$(2.9\pm0.3)\times10^{-2}$	$(1.5\pm0.6)\times10^{-5}$	$(6.5\pm0.4)\times10^{-5}$	$(4.8\pm0.4)\times10^{-5}$
	4	$(2.8\pm0.3)\times10^{-2}$	$(1.4\pm0.1)\times10^{-3}$	$(1.6\pm0.1)\times10^{-3}$	$(1.4\pm0.1)\times10^{-3}$
250	1	$(5.1\pm0.3)\times10^{-2}$	$(6.5\pm0.3)\times10^{-3}$	$(7.5\pm0.3)\times10^{-3}$	$(6.4\pm0.3)\times10^{-3}$
	2	$(4.9\pm0.2)\times10^{-2}$	$(1.5\pm0.1)\times10^{-3}$	$(1.9\pm0.2)\times10^{-3}$	$(1.6\pm0.3)\times10^{-3}$
	3	$(5.1\pm0.3)\times10^{-2}$	$(4.4\pm0.8)\times10^{-5}$	$(8.7\pm0.6)\times10^{-5}$	$(1.3\pm0.3)\times10^{-4}$
	4	$(5.1\pm0.2)\times10^{-2}$	$(1.5\pm0.1)\times10^{-3}$	$(1.9\pm0.1)\times10^{-3}$	$(1.8\pm0.2)\times10^{-3}$
565	1	$(7.5\pm0.8)\times10^{-2}$	$(5.6\pm0.6)\times10^{-3}$	$(6.8\pm0.7)\times10^{-3}$	$(5.7\pm0.6)\times10^{-3}$
	2	$(7.5\pm0.8)\times10^{-2}$	$(1.8\pm0.2)\times10^{-3}$	$(2.2\pm0.2)\times10^{-3}$	$(2.0\pm0.2)\times10^{-3}$
	3	$(7.5\pm0.7)\times10^{-2}$	$(1.5\pm0.2)\times10^{-4}$	$(3.1\pm0.5)\times10^{-4}$	$(2.5\pm0.3)\times10^{-5}$
	4	$(7.5\pm0.8)\times10^{-2}$	$(1.8\pm0.2)\times10^{-3}$	$(2.3\pm0.2)\times10^{-3}$	$(2.0\pm0.2)\times10^{-3}$
1200	1	$(1.2\pm0.1)\times10^{-1}$	$(4.5\pm0.3)\times10^{-3}$	$(6.0\pm0.6)\times10^{-3}$	$(5.6\pm0.6)\times10^{-3}$
	2	$(1.2\pm0.1)\times10^{-1}$	$(1.9\pm0.2)\times10^{-3}$	$(2.7\pm0.3)\times10^{-3}$	$(2.4\pm0.2)\times10^{-3}$
	3	$(1.2\pm0.2)\times10^{-1}$	$(4.5\pm0.3)\times10^{-4}$	$(6.0\pm0.2)\times10^{-4}$	$(5.6\pm0.2)\times10^{-4}$
	4	$(1.2\pm0.1)\times10^{-1}$	$(2.1\pm0.2)\times10^{-3}$	$(3.0\pm0.2)\times10^{-3}$	$(2.6\pm0.3)\times10^{-3}$
2500	1	$(1.2\pm0.1)\times10^{-1}$	$(3.3\pm0.3)\times10^{-3}$	$(4.2\pm0.3)\times10^{-3}$	$(3.9\pm0.3)\times10^{-3}$
	2	$(1.1\pm0.1)\times10^{-1}$	$(2.0\pm0.2)\times10^{-3}$	$(2.5\pm0.2)\times10^{-3}$	$(2.4\pm0.2)\times10^{-3}$
	3	$(1.2\pm0.1)\times10^{-1}$	$(8.5\pm0.6)\times10^{-4}$	$(1.0\pm0.1)\times10^{-3}$	$(1.1\pm0.1)\times10^{-3}$
	4	$(1.1\pm0.1)\times10^{-1}$	$(1.9\pm0.2)\times10^{-3}$	$(2.5\pm0.2)\times10^{-3}$	$(2.2\pm0.2)\times10^{-3}$
5000	1	$(1.1\pm0.1)\times10^{-1}$	$(2.4\pm0.1)\times10^{-3}$	$(3.2\pm0.3)\times10^{-3}$	$(3.0\pm0.2)\times10^{-3}$
	2	$(1.1\pm0.2)\times10^{-1}$	$(1.6\pm0.2)\times10^{-3}$	$(2.0\pm0.2)\times10^{-3}$	$(2.0\pm0.2)\times10^{-3}$
	3	$(1.1\pm0.1)\times10^{-1}$	$(8.9\pm0.9)\times10^{-4}$	$(1.3\pm0.1)\times10^{-3}$	$(1.2\pm0.1)\times10^{-3}$
	4	$(1.1\pm0.1)\times10^{-1}$	$(1.5\pm0.2)\times10^{-3}$	$(2.1\pm0.1)\times10^{-3}$	$(1.8\pm0.2)\times10^{-3}$

The MCNP modelled responses were determined by tallying either the ^{6}Li capture rate in the LiF converters or ^{10}B capture rate in the BF_3 gas volume. The subsequent transport of the charged reaction products was not determined; MCNP cannot transport alpha or triton particles. Instead it was assumed that the count rate from the detector would be directly proportional to the capture rate. Therefore prior to comparing the modelled responses to the actual experimental measurements it is necessary to normalise the MCNP data to the experimental data by introducing a constant of proportionality.

To determine this constant the modelled responses for each detector in turn were multiplied by a constant factor. The square of the difference between the scaled MCNP response and the actual experimental measurement was determined at all five ISO energies. The scale factor was then varied so as to minimise the sum of the squared differences.

The scale factor determined for each detector is reported in Table 6.3 below. Also shown in this Table are the scaled MCNP responses and the ratio of the experimental to scaled MCNP response. This data is also shown in Figures 6.8, 6.9, 6.10 and 6.11.

With the exception of measurements at 5000 keV agreement to within ± 15% was observed for all detectors. The cause of the disagreement at 5000 keV has not at present been definitively identified. However, subsequent to this experimental program the scalar units used to record the counts from the diode detectors were found to intermittently reset the counting time during acquisition. It is suspected that the disagreement at 5000 keV may be attributed to this fault. In light of the good agreement seen at all other energies the modelled responses at 5000 keV were not adjusted. Furthermore, the AAND is intended for application in relatively 'soft' neutron spectra as discussed in Chapter 3. In such spectra the fluence rate of neutrons with energies as high as 5000 keV is expected to be very small.

With regard to the effect of the orientation of the diode relative to the neutron-producing target it was observed, as expected, that the responses for positions 2 and 4 were equal. However, it was observed that a considerable variation in response was seen between positions 1 and 3, suggesting that it might be possible to determine the approximate angular distribution by examining the ratio of the response of opposing detector pairs.

Table 6.3 – Comparison of experimental and MCNP results

	BF3		D1		D2		D3	
Scale Factor	1.02		0.85		0.92		0.95	
Energy (keV)	MCNP	Expt./ MCNP	MCNP	Expt./ MCNP	MCNP	Expt./ MCNP	MCNP	Expt./ MCNP
144	3.00 $\times10^{-2}$	0.97	7.42 $\times10^{-3}$	0.89	7.63 $\times10^{-3}$	0.98	6.13 $\times10^{-3}$	1.03
250	4.79 $\times10^{-2}$	1.06	6.60 $\times10^{-3}$	0.98	7.38 $\times10^{-3}$	1.02	6.40 $\times10^{-3}$	1.00
565	7.87 $\times10^{-2}$	0.95	5.57 $\times10^{-3}$	1.01	6.70 $\times10^{-3}$	1.01	6.28 $\times10^{-3}$	0.91
1200	1.12 $\times10^{-1}$	1.07	4.22 $\times10^{-3}$	1.07	5.18 $\times10^{-3}$	1.16	5.12 $\times10^{-3}$	1.09
2500	1.10 $\times10^{-1}$	1.09	3.11 $\times10^{-3}$	1.06	3.60 $\times10^{-3}$	1.17	3.85 $\times10^{-3}$	1.01
5000	1.14 $\times10^{-1}$	0.96	1.65 $\times10^{-3}$	1.45	2.39 $\times10^{-3}$	1.34	2.24 $\times10^{-3}$	1.34

To determine the responses at energies for which there were no experimental data, i.e. $E < 144$ keV, the scale factor as determined by fitting the ISO energy MCNP results to the experimental data was again applied. The final energy responses to be utilised for the linear superposition method described in Section 6.5 are shown in Figures 6.12 and 6.13.

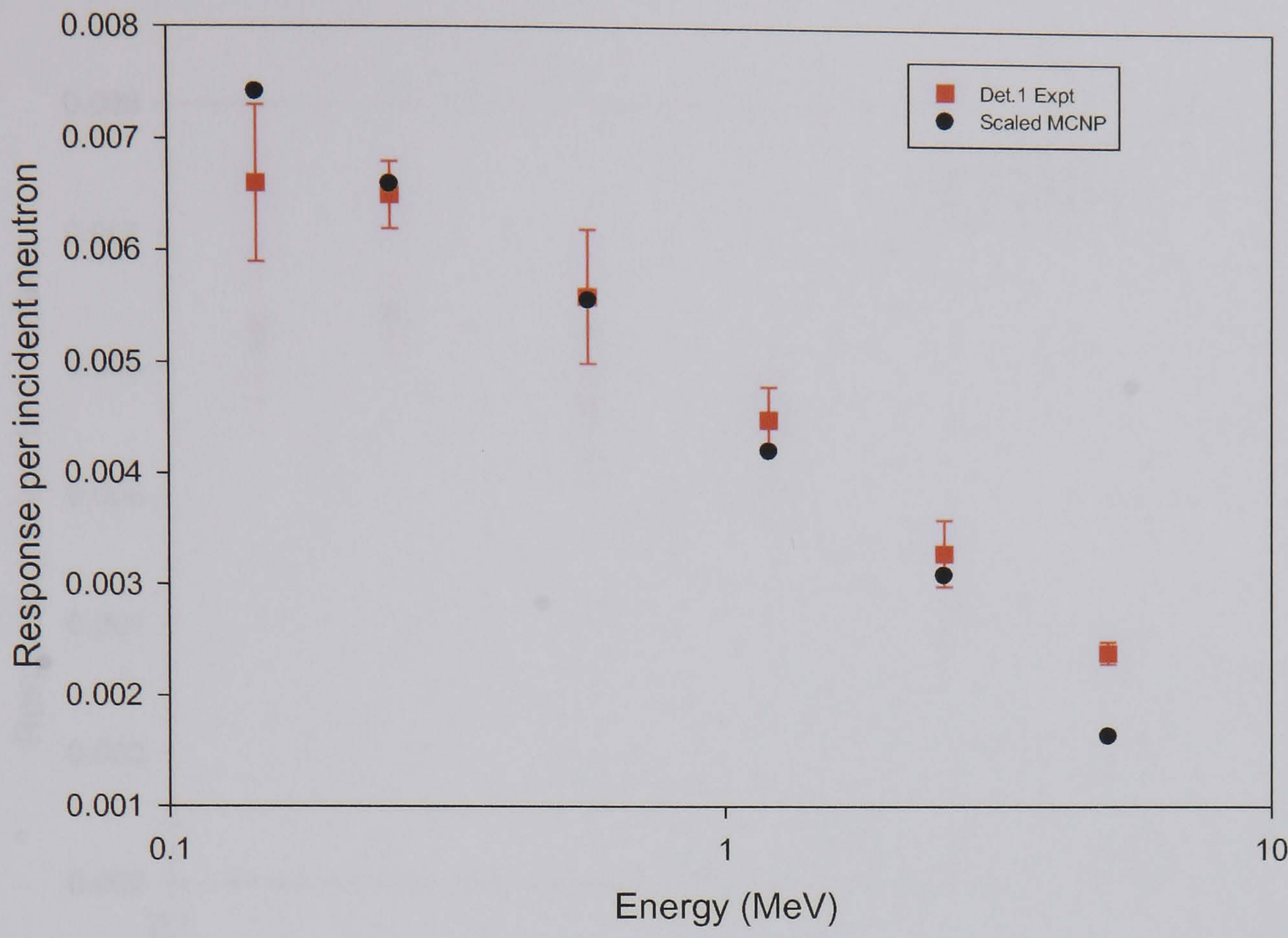

Figure 6.8 Scaled MCNP and experimental measured responses for Detector1

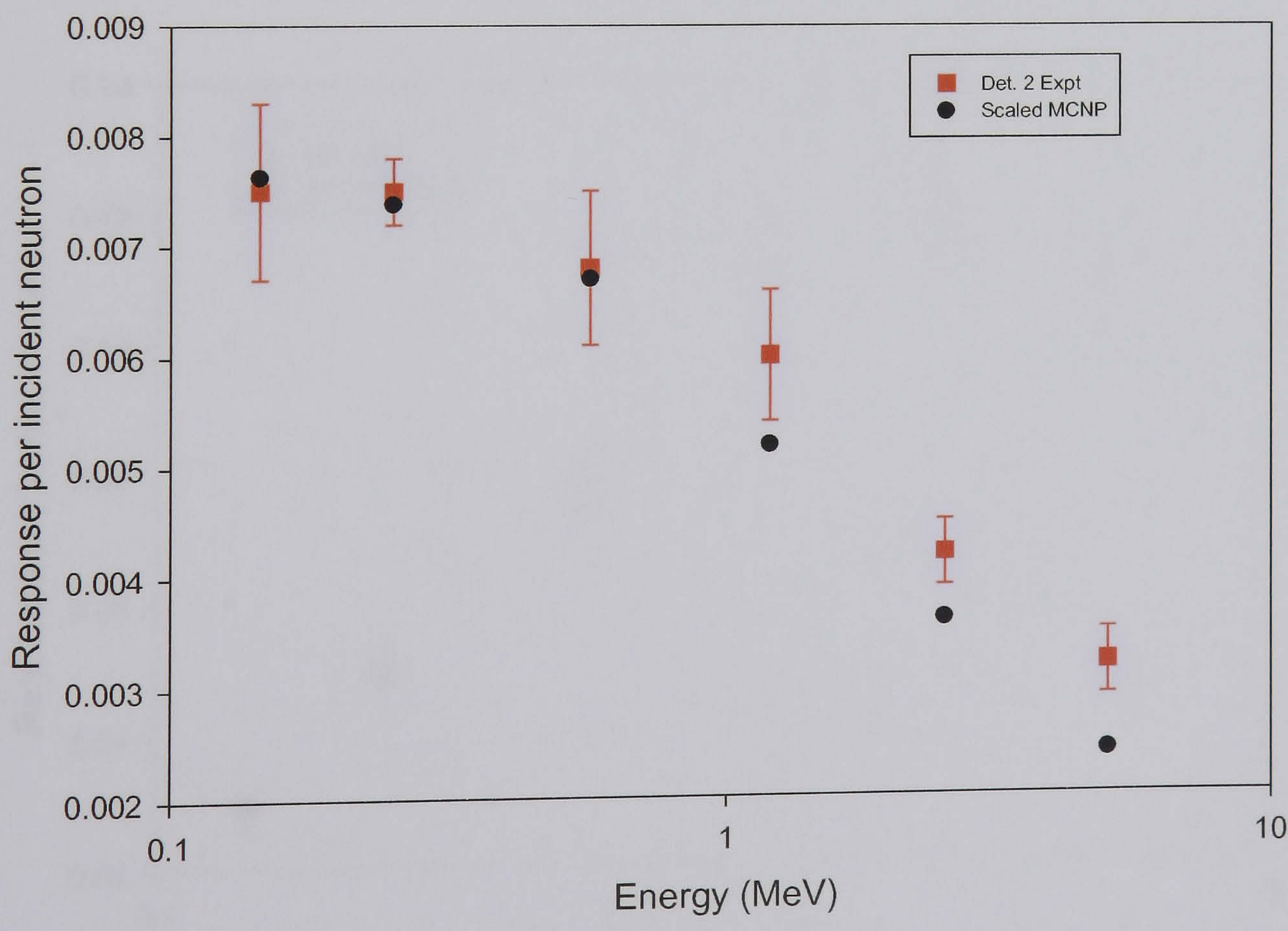

Figure 6.9 Scaled MCNP and experimental measured responses for Detector 2

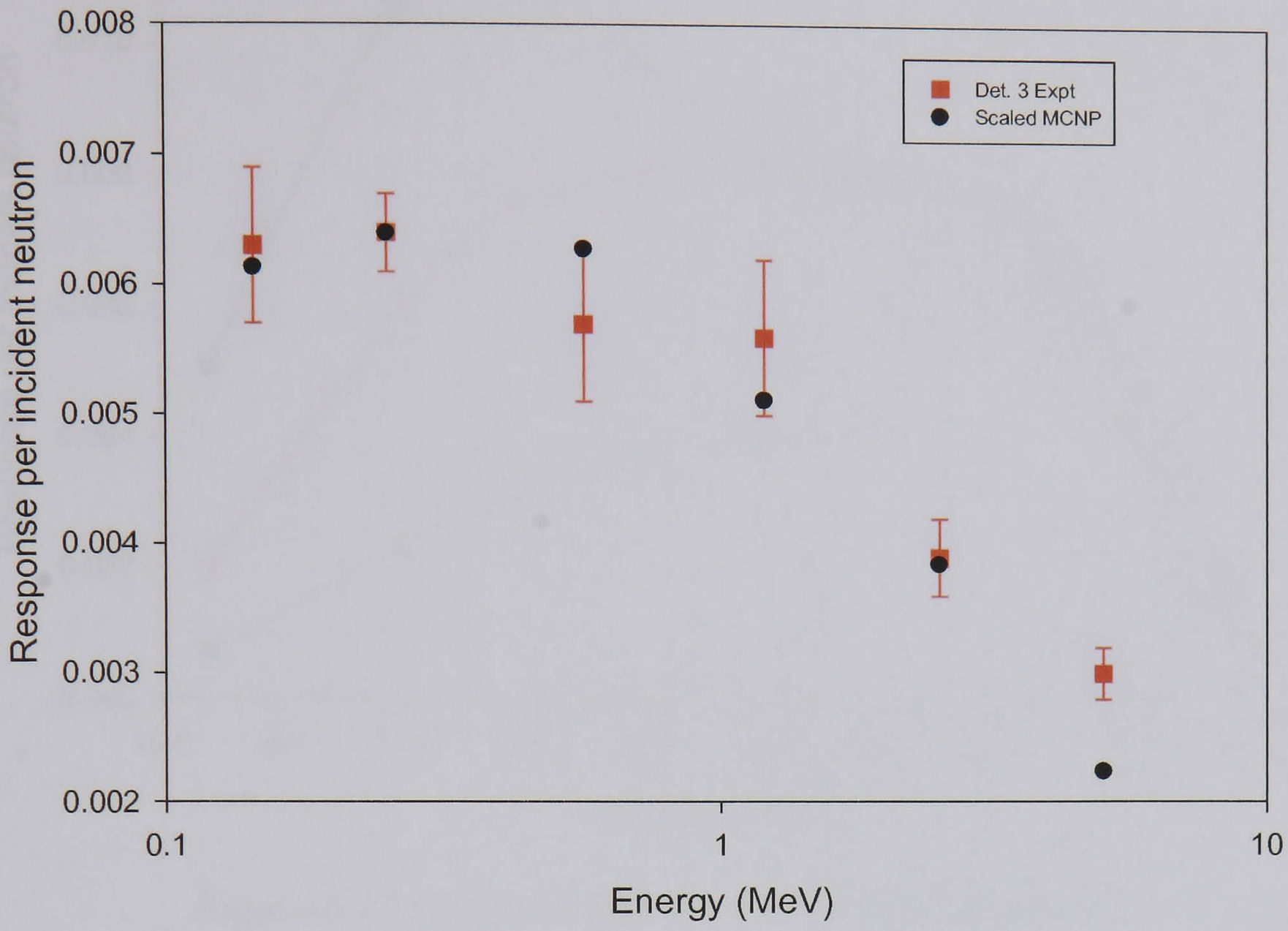

Figure 6.10 Scaled MCNP and experimental measured responses for Detector

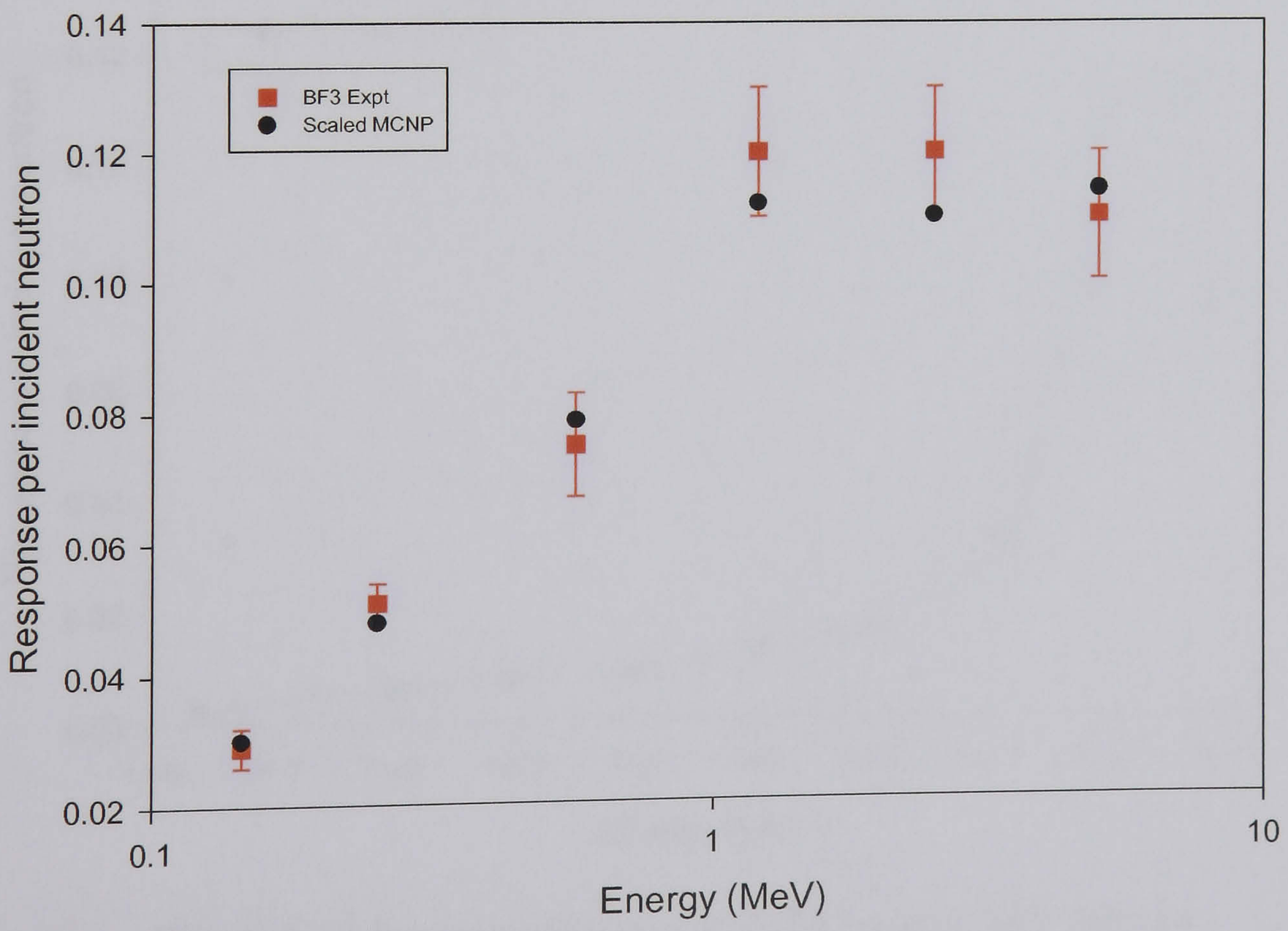

Figure 6.11 Scaled MCNP and experimental measured responses for BF_3

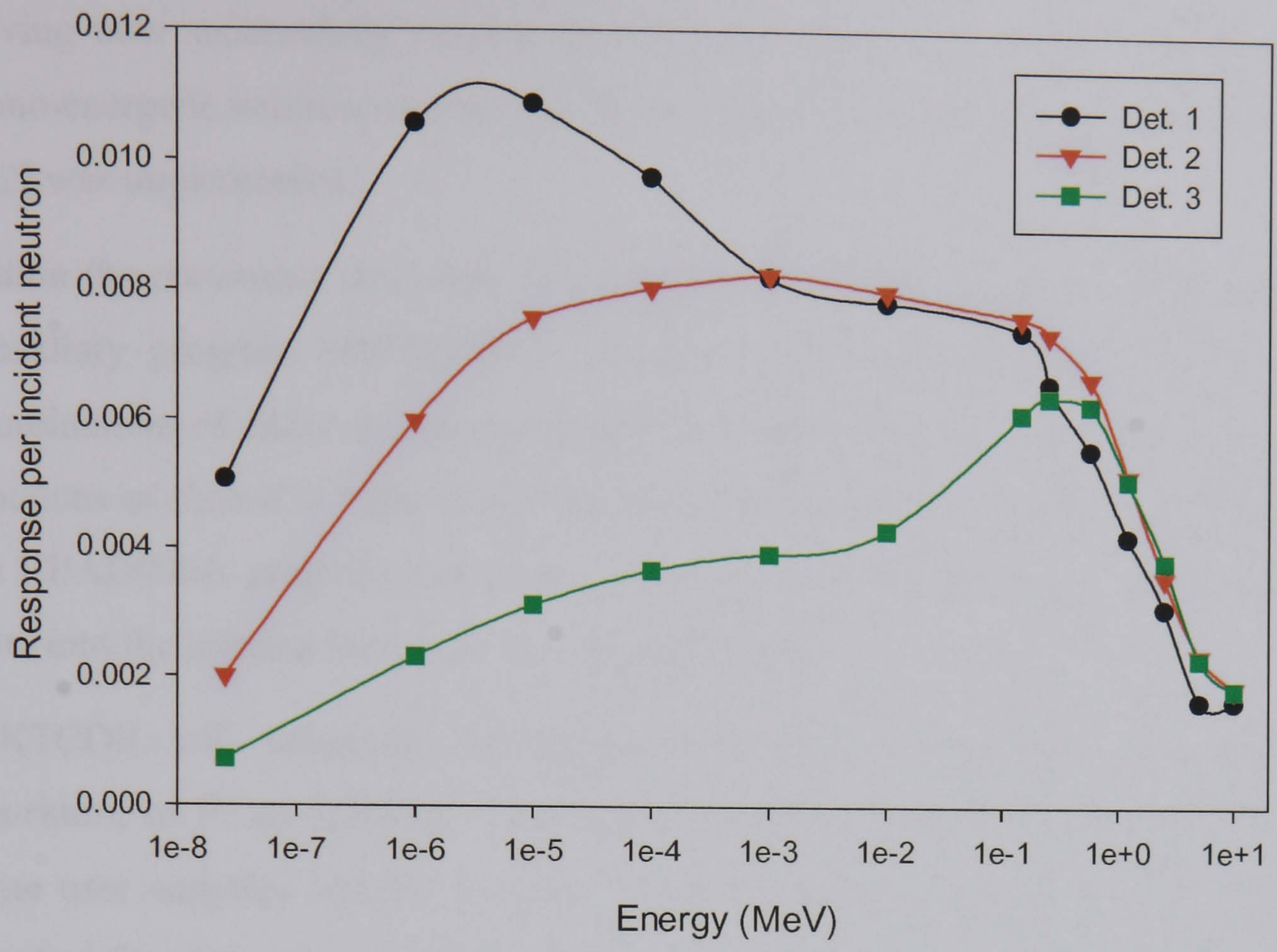

Figure 6.12 Response function of AAND diode detectors

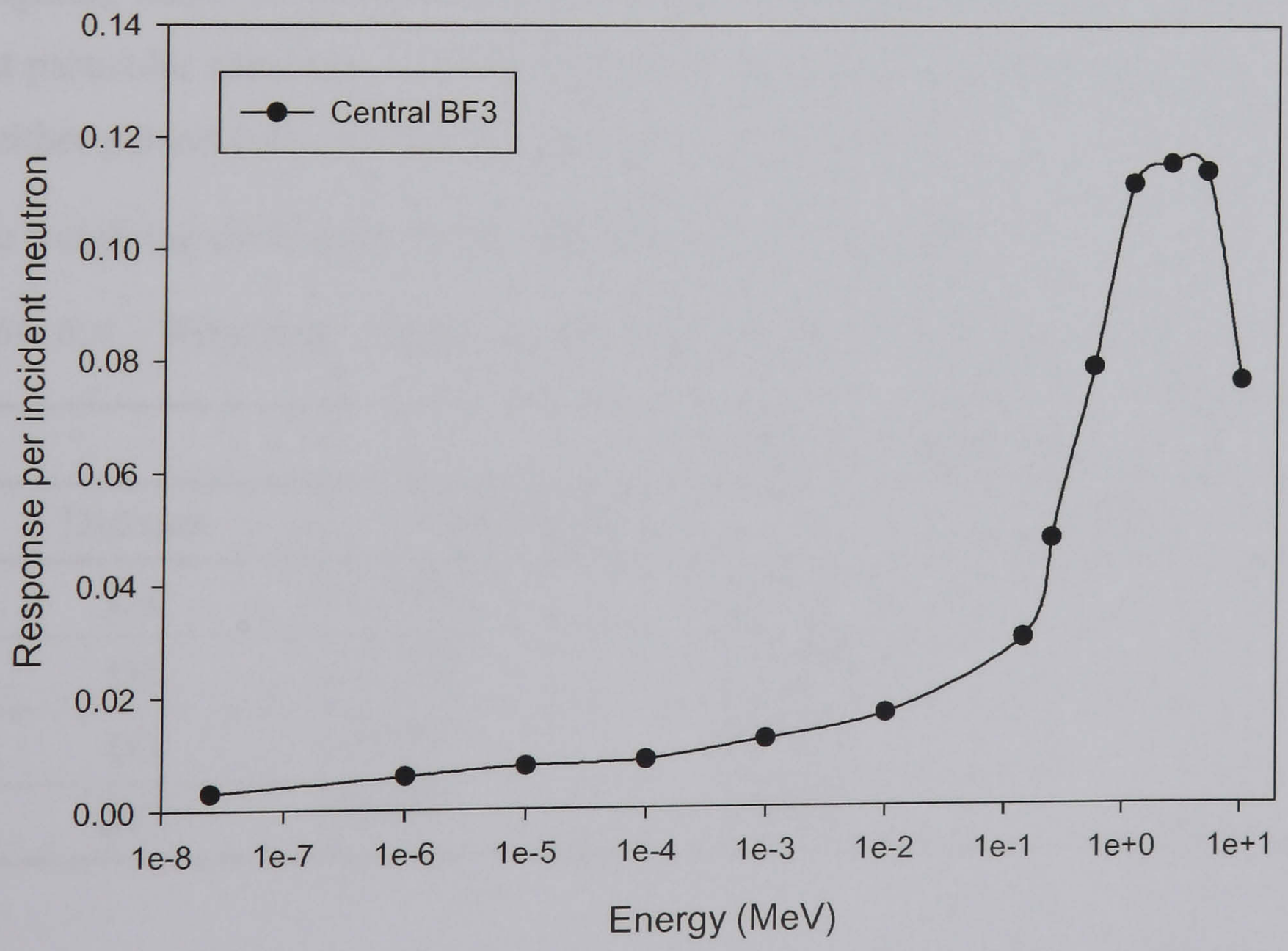

Figure 6.13 Response function of AAND central BF_3 detector

6.5 Linear Superposition Method

Having now successfully verified the modelled responses against both isotopic and mono-energetic neutron sources the linear superposition method as describe by Piesch [6.2] was implemented.

Within the previously described (see Chapter 3) computer package SPKTBIB [6.3] a subsidiary program SPKTCOR is supplied. This program allows both weighted combinations of either detector responses or neutron spectra to be made. The response functions as shown in Figures 6.12 and 6.13 were prepared for use in SPKTBIB using the READ000& program that converts a simple text file of energy and response data pairs into the internal format as used by SPKTBIB.

SPKTCOR will determine weighting coefficients, using a least squares fitting algorithm, to fit an arbitrary combination of up to eight user supplied functions to some user supplied 'target' function. In the particular case of the AAND the user supplied functions were the response functions (expressed in terms of per unit fluence rate) of the BF_3 detector and the three diodes. Two 'target' functions were used the ambient dose equivalent *H*(10)* and the radiation weighting factor *wR*. Although unusual for a dosemeter it was considered that an indication of the radiation-weighting factor of the neutron radiation field would provide a useful characteristic of that particular spectrum. This quality could be used to apply a local correction factor to either personal dosemeters or other survey instruments.

The weighting coefficients determined are given in Table 6.4.

Table 6.4 – Weighting coefficients for AAND fit to H(10)* and3 *wR*

	Weighting Coefficients	
Detector	*H*(10)* fit	*wR* fit
D1	1.316	0.510
D2	-3.755	-1.248
D3	2.612	1.726
BF3	0.827	0.012

To confirm the accuracy of the SPKTCOR fits the previously identified eight representative spectra, identified in Chapter 3, were folded with the AAND *H*(10)* and *wR* fits to determine the *H*(10)* and *wR* of each of these spectrum. These results

and the reference value determined by directly folding the ICRP74 fluence to *H*(10)* and the ICRP 60 *wR* relationship are shown in Table 6.5.

Table 6.5 Simulated response of AAND in realistic fields

Spectrum Description	Reference value		AAND	
	Mean wR	h*(10) (pSV cm^2)	Mean wR	h*(10) (pSV cm^2)
Czech PWR circulation pump room	7.45	40.2	7.2	39
Swiss BWR 16m level	7.53	36.7	7.7	38
Traws GCR BCD filter gallery	6.77	29.8	6.8	28
Swiss BWR reactor level stairwell	6.78	27.4	7.2	29
Caorso BWR inside reactor cavity	13.9	141	13.5	140
Czech PWR reactor hall	13.4	141	13.2	140
IAEA 318 PWR Loc. 81	8.34	61.6	8.7	59
Swiss BWR airlock into containment	10.8	80.7	10.2	81

As may be seen in Table 6.5 the simulated AAND *H*(10)* and *wR* values agree very well with the reference values, typically to better than ± 10%.

6.6 Demonstration of the AAND

At the Defence Radiological Standards Centre (DrStaC) a number of the ISO standard isotopic neutron sources are maintained in a relatively low scatter environment. The facility consists of a large irradiation room (5.5m × 9.1m × 4.4m) housing both ^{252}Cf and $^{241}Am/Be$ sources, a 30 cm diameter D_2O filled sphere, a shadow cone for scatter correction and a calibrated DePanger long counter.

The AAND was calibrated to indicate *H*(10)* and the *wR* by recording the count rate C_i from each detector when exposed to a ^{252}Cf calibration source and then applying the previously determined linear fit to determine the total AAND response C in terms of weighted counts, see Equation 6.1. The scatter corrected count rates were calculated by subtracting the count rate recorded with the scatter cone in position. The scatter cone absorbs all neutrons arriving directly from the source; only neutrons that have scattered in the room and then subsequently interact in the AAND will be

detected. Therefore, by subtracting this count rate from the un-shadowed result the contribution of scattered neutrons was eliminated.

$$C = a_{D1}C_{D1} + a_{D2}C_{D2} + a_{D3}C_{D3} + a_{BF3}C_{BF3} \qquad \textit{Equation 6.1}$$

where, C – is the weighted response of the AAND

a_i – is the weighting coefficeint of the ith detector

Ci – is the scatter corrected count rate from the ith detector

i – detectors D1, D2, D3 and BF3

To determine the dose rate the DePanger long counter was used to determine the neutron fluence rate at the AAND calibration position and then by applying the fluence to H*(10) conversion coefficients given in Table 3.4. the 'reference' dose rate D_R was calculated. The calibration of the AAND was then completed by calculating R according to Equation 6.2 in terms of count s^{-1} /μSv h^{-1}. These results are shown in Table 6.6.

$$R = \frac{C}{D_R} \qquad \textit{Equation 6.2}$$

Table 6.6 ^{252}Cf calibration of AAND for H(10)*

Detector	Scatter corrected count rate s^{-1} $C_i \pm 2\sigma$	Weighting factor a_i	Weighted count $C_i \times a_i \pm 2\sigma$
D1	0.27 ± 0.02	1.316	0.36 ± 0.03
D2	0.37 ± 0.03	-3.755	-1.39 ± 0.11
D3	0.39 ± 0.02	2.612	1.02 ± 0.05
BF3	1.17 ± 0.03	0.827	0.97 ± 0.02
Sum of weighted counts – C			0.96 ± 0.14 s^{-1}
Dose rate - D_R			214.8 ± 1.7 μSv h^{-1}
Calibration factor – R			$(4.47 \pm 0.65) \times 10^{-3}$ s^{-1}/μSv h^{-1}

Subsequently, the ^{252}Cf source was replaced by a ^{241}Am/Be and a D_2O moderated ^{252}Cf source. Again the count rates from each detector were recorded, scatter

correction using the shadow cone was only possible for the ^{241}Am/Be source as the 30 cm D_2O sphere was too large to be shadowed by the available shadow cones. The weighted sum of the count rates was calculated and then by using the previously determined calibration factor the total count rate was converted into a dose rate. See Table 6.7 and 6.8.

Table 6.7 Determination of D_2O ^{252}Cf H(10) dose rate using the AAND*

Detector	Scatter corrected count rate s^{-1} $C_i \pm 2\sigma$	Weighting factor a_i	Weighted count $C_i \times a_i \pm 2\sigma$
D1	0.23 ± 0.03	1.316	0.30 ± 0.04
D2	0.27 ± 0.02	-3.755	-1.01 ± 0.08
D3	0.24 ± 0.03	2.612	0.63 ± 0.08
BF3	0.45 ± 0.02	0.827	0.37 ± 0.02
Sum of weighted counts – C			0.29 ± 0.03 s^{-1}
Calibration factor – R			$(4.47 \pm 0.65)\times10^{-3}$ $s^{-1}/\mu Sv\ h^{-1}$
AAND Dose rate			64 ± 11 $\mu Sv\ h^{-1}$
Reference Dose rate from DePanger			58.2 ± 0.8 $\mu Sv\ h^{-1}$

Table 6.8 Determination of ^{241}Am/Be H(10) dose rate using the AAND*

Detector	Scatter corrected count rate s^{-1} $C_i \pm 2\sigma$	Weighting factor a_i	Weighted count $C_i \times a_i \pm 2\sigma$
D1	0.027 ± 0.004	1.316	0.036 ± 0.005
D2	0.041 ± 0.005	-3.755	-0.15 ± 0.02
D3	0.044 ± 0.006	2.612	0.11 ± 0.02
BF3	0.14 ± 0.02	0.827	0.12 ± 0.02
Sum of weighted counts – C			0.116 ± 0.03 s^{-1}
Calibration factor – R			$(4.47 \pm 0.65)\times10^{-3}$ $s^{-1}/\mu Sv\ h^{-1}$
AAND Dose rate			26 ± 6 $\mu Sv\ h^{-1}$

Reference Dose rate from DePanger	24.2 ± 0.4 μSv h^{-1}

A similar calibration process was applied for the fit to *wR*, however, instead of dividing the weighted response from the ^{252}Cf source by the dose rate the response was divided by the calculated mean *wR*. The mean *wR* was determined using SPKTBIB by folding the ICRP 60 *wR* relationship with the neutron energy spectra, as discussed in Chapter 3.

Shown in Table 6.9 are the results of the *wR* calibration using the ^{252}Cf source. The AAND determined *wR* for the D_2O moderated ^{252}Cf source is given in Table 6.10. Good agreement was seen between the AAND *wR* and the reference *wR* value for the D_2O ^{252}Cf spectrum.

Table 6.9 ^{252}Cf calibration of AAND for wR

Detector	Scatter corrected count rate s^{-1} $C_i \pm 2\sigma$	Weighting factor a_i	Weighted count $C_i \times a_i \pm 2\sigma$
D1	0.27 ±0.02	0.510	0.14 ± 0.02
D2	0.37 ±0.03	-1.248	-0.46 ± 0.04
D3	0.39 ±0.02	1.726	0.67 ± 0.03
BF3	1.17 ±0.03	0.012	0.0140 ± 0.0004
Sum of weighted counts – C			0.36 ± 0.08 s^{-1}
Calculated - wR			17.54
Calibration factor – R			$(2.1 \pm 0.5) \times 10^{-2}$ s^{-1}

Table 6.10 Determination of D_2O ^{252}Cf wR dose rate using the AAND

Detector	Scatter corrected count rate s^{-1} $C_i \pm 2\sigma$	Weighting factor a_i	Weighted count $C_i \times a_i \pm 2\sigma$
D1	0.23 ± 0.03	0.510	0.12 ± 0.02
D2	0.27 ± 0.02	-1.248	-0.34 ± 0.03
D3	0.24 ± 0.03	1.726	0.41 ± 0.05
BF3	0.45 ± 0.02	0.012	$(2.1 \pm 0.2)\times10^{-3}$
Sum of weighted counts – C			0.19 ± 0.04 s^{-1}
Calibration factor – R			$(2.1 \pm 0.5) \times10^{-2}$ s^{-1}
AAND wR			9.0 ± 1.4
Reference Dose wR			9.59

However, when this methodology was applied to the ^{241}Am/Be spectrum, see Table 6.11, a substantial disagreement was apparent.

Table 6.11 Determination of $^{241}Am/Be$ wR using the AAND

Detector	Scatter corrected count rate s-1 $C_i \pm 2\sigma$	Weighting factor a_i	Weighted count $C_i \times a_i \pm 2\sigma$
D1	0.027 ± 0.004	0.510	0.014 ± 0.003
D2	0.041 ± 0.005	-1.248	-0.051 ± 0.008
D3	0.044 ± 0.006	1.726	0.08 ± 0.01
BF3	0.14 ± 0.02	0.012	0.0017 ± 0.0002
Sum of weighted counts – C			0.05 ± 0.03 s^{-1}
Calibration factor – R			$(2.1 \pm 0.5)\times10^{-2}$ s^{-1}
AAND wR			2.4 ± 1.4
Reference Dose wR			13.99

On closer examination of the raw count rate data and the magnitude of the weighting coefficients, the uncertainty of the combined response was calculated to be approximately 60%. The ^{241}Am/Be source had a substantially lower activity and consequently dose rate, than the ^{252}Cf source. Therefore, the count rates from each detector had very large uncertainties. Unlike the fit to *H*(10)* where the central BF_3 is given a high weighting in the *wR* fit this detector receives a very low weight and so the *wR* response is dominated by the diode detectors. At high energies, E > 2 MeV all of the diode detector responses are very similar. It is considered likely that the low dose and 'hard' spectrum from the ^{241}Am/Be lead to near identical count rates from the three diode detectors and consequently a erroneous determination of *wR*. Regrettably, time limitations prevented a longer measurement to accumulate a large number of counts from each diode detector and so reduce the uncertainties.

6.7 Conclusions

The AAND has demonstrated that the addition of outer detectors to a traditional central detector in a moderating type neutron dosemeter and the use of a combination of all of the detectors responses can accurately determine *H*(10)*. Whilst calibrating and demonstrating the AAND at DRStaC the dose rate in the calibration positions was recorded using a standard Leake type Mk7NRM. For comparison with the AAND the dose rate as recorded using a Mk7NRM is reported in Table 6.12.

Table 6.12 Comparisons of AAND and Mk7NRM

Source	Measured dose rate μSv/h		
	AAND	Mk7NRM	DePanger
D_2O Cf	64	90	58.2
Am/Be	26	30	24.2
	Radiation weighting factor		
	AAND	Calculated from ISO spectrum	
D_2O Cf	9.0	9.59	
Am/Be	2.4	13.99	

The design aim of the AAND was that it should be optimised for use in 'soft' spectra where the well known over response of Mk7NRM is quite pronounced. The AAND reduced the over estimate of Mk7NRM of 1.55 for the D_2O ^{252}Cf to only 1.10.

Furthermore, the use of additional detectors allows spectral characteristics to be determined. In this work attention was focused on *wR*, despite the erroneous

indication for ^{241}Am/Be the successful determination for the D_2O ^{252}Cf was encouraging. Clearly for the AAND to be operated in 'hard' spectra at relatively low doses the diode detectors must have a higher sensitivity. However, in the intended operational environment spectra are typically very soft.

The choice of radiation weighting factor was somewhat arbitrary as a spectrum characteristic. It is suggested for further study that rather than determine *wR*, a more practical application would be to correlate the under or over response of smaller more portable survey instruments with a spectral characteristic derived from the AAND. Previously, the ratio between the count rate in two different diameter Bonner spheres has been correlated with the under and over responses of a Mk7NRM and so used to correct its response.

After the conclusion of this thesis, development of the AAND is to be continued. It is suggested that larger surface area photodiodes, devices up to 150 mm^2 are available, be obtained and that all radial channels are populated. Rather than just a single diode contributing to the D1 position response, the response will now be the sum of all four diodes. Together with an increased surface area available for application of LiF this is expected to yield an increase in sensitivity.

By populating all the radial channels the possibility of examining angular distribution is available. The experimental measurements indicate the diode detectors are directionally sensitive. In rotational fields, those usually encountered in 'real life', the response from each of the four D1 diodes would be equal. However, as may be seen from the variation in response between position 1 (towards source) and position 3 (away from source) in Table 6.2 if the AAND were exposed to a directional field for example AP then the ratio of the response between opposite D1 (or D2, D3) detectors may allow the angular distribution to be coarsely determined. It is suggested that in the subsequent development of the AAND that this is considered further.

6.8 References for Chapter 6

[6.1] Bartlett D.T., Tanner R.J., **Rad. Prot. Dosim.**, 74(3), 267, 1997.

[6.2] Piesch E., Burgkhardt B., Comper W., **Rad. Prot. Dosim.**, 10(1-4), 147,1985.

[6.3] Naismith O.F. and Siebert B.R.L., **NPL Report CIRA(EXT)005 - Manual for SPKTBIB: a PC-based Catalogue of Neutron Spectra**,. Teddington: National Physical Laboratory, 1996.

Chapter 7 – Conclusions

7.1 Summary of Findings

The development of the Active Area Neutron Dosemeter was conducted in four distinct stages. Firstly, discussed in Chapter 3, eight spectra that are representative of those encountered in the Naval Nuclear Propulsion Program were selected, see Table 3.2. The three metrics used for this selection were the mean energy, the mean radiation-weighting factor and the fluence to ambient dose equivalent conversion coefficient. This work demonstrated that the typical operational spectra differ significantly, compare Table 3.2 and 3.4, from the frequently used calibration source spectra generated by ^{241}Am/Be or ^{252}Cf.

For this selected group of spectra it was shown, see Figure 3.5, that neutrons with an energy of less than 500 keV typically account for over 50% of the H*(10) dose rate, in two particular cases this contribution can be as much as 80%. Consequently the identified deficiencies in the energy response of traditional neutron area survey instruments, discussed in Section 2.4, particularly the over-response to intermediate energy neutrons will cause these instruments to incorrectly indicate dose rate.

With reference to the current MOD preferred instrument, the Mark 7 NRM, it was demonstrated that, see Figures 3.8 and 3.9, the maximum over-estimation of dose rate could be as high as two fold in very soft neutron spectra. Such over-estimation, whilst conservative, is clearly not desirable and therefore a new neutron area survey instrument, the AAND, was proposed that would address these deficiencies. In the AAND design the traditional thermal neutron sensitive central detector is augmented by small thermal sensitive detectors positioned within the moderating body, referred to in this thesis as the 'outer' detectors.

Development of the AAND now moved to the second stage, the selection and development of the outer detectors. Previous work by a number of authors including Darambara [4.3, 4.7] had suggested that the phenomenon of single event upsets (SEU) in dynamic random access memories (dRAM) devices could be used for neutron detection. Therefore, an experimental study was conducted, discussed in Chapter 4, into this phenomenon.

Neutrons as un-charged particles cannot directly cause an SEU; instead they must be converted into a highly ionising particle such as an alpha particle. An experimental and theoretical study was conducted to optimise this conversion process. The two most practical are ^{10}B and ^{6}Li both of which have a high cross-section for the (n,α) reaction. It was known [4.3, 4.7] that there was a threshold energy below which alpha particles did not induce an SEU. Whilst the ^{10}B reaction has the higher cross-section the energy of the alpha particle produced is 1.47 MeV, only 0.07 MeV above the calculated threshold energy, see Section 4.1.1.

A model was developed of the neutron conversion layer to be applied to the surface of the dRAM referred to determine its optimum thickness, see Section 4.2. It was concluded that a layer of 4 μm was optimal; the maximum range of the alpha particles bound the thickness.

Previous work had examined 64 kBit devices. In this study 1 Mbit devices from three manufacturers were examined, see Section 4.4. Considerable advance in device architecture had occurred between the 64 kBit and the 1 Mbit devices. The sensitivity of the device, expressed as the number of SEU per unit fluence rate, was determined for all three devices and found to be typically 10^{-8} cm^2, details in Table 4.14. This sensitivity was much lower than that predicted by scaling from 64 kBit results. As anticipated the developments, notably small feature sizes and multi-layer construction, had all acted to reduce the SEU sensitivity. In normal operation SEUs are undesirable and therefore considerable effort has been expended by the semiconductor industry to reduce this effect. This work was presented at the 10^{th} MTAA meeting [7.1].

Having discounted dRAM devices, lithium fluoride coated silicon photodiodes were investigated, reported in Chapter 5. Commercial devices with a surface area of 41.3 mm^2 were coated with a 5 μm layer of ^{6}LiF (enriched to 95% by atom ^{6}Li). The neutron sensitivity, expressed in counts above the detection threshold per unit fluence rate, was found to be typically 10^{-4}, see Table 5.2. It was necessary to set a lower level energy discriminator threshold, set on a pulse height criterion, to remove the contribution from gamma ray interactions. Photodiodes have a thin sensitive layer, the depletion depth, approximately 70 μm deep and are therefore relatively insensitive to gamma rays.

Development of the AAND now advanced to the third stage, the design of the detector and moderator arrangement. The review of current instruments and their response to 'operational' spectra had indicated that; see Figure 3.8 and 3.9, the cylindrical NM2 performed well. The cylindrical shape was consequently adopted for the AAND.

A Monte Carlo model of the AAND was produced in MCNP, see Appendix A and Chapter 6, allowing the effect of varying the cadmium filter layer concentrically arranged around a central BF_3 detector to be studied. An ideal instrument would have a response whose energy dependence followed that of the ICRP 74 recommended fluence to dose conversion coefficients. Final dimensions selected were a polyethylene cylinder 24.5 cm long with a radius of 10.5 cm, a central BF_3 detector surrounded by a 1.7 cm polyethylene layer and a 1 mm thick cadmium shell. The modelled energy response is shown in Figure 6.2.

Attention now moved to the outer detectors. To model their position a thin cell of LiF was added to the MCNP model. By tallying the (n,α) reaction rate in the cell and by assuming that the photodiodes response would be proportional to this rate the energy dependent response of this detector could be investigated.

Piesch [6.2] had demonstrated that by combining the responses of multiple detectors located on and within the surface of a polyethylene sphere, neutron dose could be well determined. He had proposed using a weighted summation of the response of neutron sensitive TLDs, the weighting coefficients for each detector contribution having previously been determined by fitting the weighted summed responses to the desired fluence to H*(10) conversion coefficients.

This method with active detectors was adopted for the AAND. The MCNP model was used to investigate the positioning of the detectors within the moderator. Three detectors positioned 2.2 cm (D1), 3.4 cm (D2) and 4.6 cm (D3) below the moderator surface were selected. This positioning produced three distinct response curves, shown in Figure 6.3.

All necessary dimensions had now been determined and development of the AAND now entered the final experimental stage, discussed in Section 6.3 to 6.6. A prototype AAND was produced. For this initial prototype only 3 photodiodes and associated NIM counting electronics were available. In the final AAND it is intended that there

be four radial sets of three photodiode detectors arranged orthogonal to the long axis of the AAND. Therefore, in the prototype only a single 1 radial channel could be populated.

Prior to the necessary verification of the modelled detector energy responses against mono-energetic irradiations, a relatively simple study using an 241Am/Be source and various shielding combinations was conducted. The ratio between each of the individual photodiode detectors e.g. D1/D2 and D1/D3 count was determined for five different spectra, reported in Table 6.1. Two of these irradiations, bare ^{252}Cf and ^{241}Am/Be, were also simulated in MCNP. Good agreement was observed between these and experimental results. Although all relatively hard spectra due to the ^{241}Am/Be source available, the variation in detector ratios confirmed that they could 'distinguish' varying neutron spectra. This work was presented at NEUSPEC 2000 [7.2].

The successful proof of concept testing allowed progression to the final fourth stage of development. The verification of detector responses with mono-energetic standards and demonstration against isotopic standards.

The AAND was exposed to the six ISO standard mono-energetic standards available at the National Physical Laboratory. The response, expressed as counts per unit fluence rate, was determined in four irradiation geometries, this allowed the diodes to be aligned at 90° intervals relative to the neutron producing target, see Figure 6.7. These results are given in Table 6.2 and Figures 6.8 – 6.11. It is worth noting that in the final design the response for detector position D1 would be the summation of all four diodes located at position D1 in each of the four radial channels.

In order to compare these experimental measurements to the MCNP modelled responses it was necessary to introduce a normalisation factor. The MCNP model had tallied the (n,α) reaction rate in the LiF cell, the subsequent transport and detection of the resultant particles in the photodiode could not be modelled. The comparison between experimental and modelled results is given in Table 6.3. Good agreement was observed in for all detectors at all energies (24 measurements) with the exception of two cases D1 and D2 at 5 MeV. Later investigation suggested that this might have been attributable to a fault in the scalar/timer module. The good agreement between

experiment and model observed at all 22 other measurements gave sufficient confidence to discount these two cases and retain the modelled data.

The energy dependent response of each of the detectors were then used as input functions for the PC program SPKTCOR. SPKTCOR determines, using a least squares method, the weighting coefficients necessary to fit some input functions to a desired target function. Two target functions were selected the required ICRP 74 fluence to dose conversion coefficients, the ideal instrument response, and the ICRP recommended radiation weighting factors. The radiation-weighting factor was selected as a simple spectral characteristic that could be used to characterise a particular field. The determined weighting coefficients are reported in Table 6.4 and a computational demonstration of their accuracy is reported in Table 6.5.

Finally, having now verified the detector responses, the AAND was demonstrated using the standardised neutron sources at the Defence Radiological Standards Centre (DraStaC), reported in Section 6.6, where a standardised ^{241}Am/Be, ^{252}Cf and D_2O moderated ^{252}Cf are available. The AAND was calibrated to indicate H*(10) using a ^{252}Cf source and the DRaStaC standard DePanger long counter to determine the true dose rate, reported in Table 6.6

The indicated dose rate from the AAND in both ^{241}Am/Be and D_2O moderated ^{252}Cf spectra was determined and compared to the true dose rate from the long counter, reported in Tables 6.7 and 6.8. This process was repeated for the fit to the radiation-weighting factor and these results are reported in Tables 6.9 to 6.11.

Good agreement between the AAND indicated dose rate and the DePanger values, see Table 6.12, for both the 'hard' ^{241}Am/Be and the 'softer' D_20 moderated ^{252}Cf was seen. The determination of radiation-weighting factor was successful for the D_20 moderated ^{252}Cf spectrum. However, in the ^{241}Am/Be significant disagreement was seen. The very low count rate in the shallowest D1 detector and almost equal count rates in the two detectors D2 and D3 introduce significant uncertainty. The design of the AAND had been optimised with 'soft' operational spectra in mind. If operation in harder spectrum is anticipated re-positioning of the diode detectors is likely.

In conclusion, a likely over-estimation of dose has been identified in current instrumentation and a new device proposed to address this. By combining multiple

detector responses it has been demonstrated that an improved area survey instrument can be produced.

7.2 Further Work

Suggested further work, some of which is already underway at the Nuclear Department by the author, concerns both the production of a truly field portable prototype (Mark 2 AAND) and further developments to the AAND concept.

With respect to the production of a field prototype the following work is suggested.

1. *Fabrication of twelve coated photodiodes to populate all four radial channels.*

   Larger surface area photodiodes are commercially available (up to 150 mm^2) and it is recommended that these be adopted for the Mark 2 AAND, as this will offer an increase in neutron sensitivity due to the larger area LiF converter layer available.

2. *Improvements in construction of moderating body and photodiode detector housings.*

   The Mark 1 AAND moderator and detector housings were fabricated to allow easy removal and insertion of the photodiode detectors. To achieve the required ruggedisation for field applications it is recommend that stepped polyethylene plugs are used to close the photodiode detector channels to eliminate possible streaming of neutrons.

3. *Development of miniaturised counting electrons to replace NIM modules.*

   For the initial prototype conventional NIM rack electronic modules were utilised. To be practical to operate in a field environment these large and bulky modules must be replaced by custom designed amplifiers and counters.

4. *Re-verification of detector response functions.*

   The suggested improvements to both the moderator and diode housing could affect the detector response functions. Therefore, it is recommended that the both the MCNP and experimental study with mono-energetic neutrons is repeated when the Mark 2 AAND and associated custom electronics becomes available. It is further recommended that together with the six standard ISO energies considered in this work that an experimental measurement is also made in a thermal field.

5. *Demonstration of Mark 2 AAND in realistic fields.*

At the National Physical Laboratory a neutron spectrum that is representative of those encountered in typical workplaces is now available. It is recommended that as a final demonstration that the AAND is exposed to this field and both the displayed *H*(10)* and *wR* are compared to the reference values.

With respect to further developments to the AAND concept the following further work is suggested.

6. *Re-examination of alternative filters.*

In the Mark 1 AAND a cadmium filter was used. However, in light of increasing regulatory instructions that will effectively prohibit the use of cadmium it is suggested that alternative filters be investigated. A recommended starting point would be the use of a boron-load plastic.

7. Examination of angular response.

As discussed in Section 6.7 the variation of the photodiode detectors response relative to their alignment to the neutron-producing target was quite marked. In the Mark 2 AAND all radial channels are to be populated and it is therefore recommended that the potential to derive the angular distribution of the incident neutron spectrum be examined.

Subsequent to the completion of this thesis suggested items 1 to 3 have been successfully completed at the Nuclear Department.

7.3 Publications by the Author

[7.1] Brushwood J.M., Harvey S. Beeley P.A., Spyrou N.M., Further development of a novel neutron detector using the single event upset phenomenon in dynamic random access memories. **J. Radioanal. Nucl. Chem.**, 244(3), 637, 2000.

[7.2] Brushwood J.M., Beeley P.A., Spyrou N.M., Design of an improved neutron dose equivalent dosimeter. **Nucl. Instr. and Meths. in Phys. Res.**, A476, 304, 2002.

Appendix A – Sample MCNP input file for the AAND

```
message: datapath=c:\mcnp4c\xs

AAND Final model
c ------------------ Cell cards ---------------------------
c  BF3  detector  6EB60/30  20mm  dead  space  +  60mm  active
length
1          4     -1.2E-3    -6 -17 16
2          2     -2.634E-3  -6 -16 14
3          4     -1.2E-3    -6 -14 10
c Poly collar with cable runs
10         4     -1.2E-3    -3 6 -11 10
11         1     -0.93      -3 6 -12 11
c Cd back plate
20         3     -8.642     -4 6 -13 12
c Poly sleeve around active BF3 region
30         1     -0.93      -5 6 13 -14
31         1     -0.93      -5 6 14 -15
32         1     -0.93      -5 6 15 -16
33         1     -0.93      -5 6 16 -17
34         1     -0.93      -5 6 17 -18
35         1     -0.93      -6 17 -18
c Cd sleeve
40         3     -8.642     -4 5 13 -14
41         3     -8.642     -4 5 14 -15
42         3     -8.642     -4 5 15 -16
43         3     -8.642     -4 5 16 -17
44         3     -8.642     -4 5 17 -18
45         3     -8.642     -4 6 18 -19
46         3     -8.642     -6 18 -19
c Air gap for cables
50         4     -1.2E-3    -3 4 12 -14
51         4     -1.2E-3    -3 4 14 -15
52         4     -1.2E-3    -3 4 15 -16
53         4     -1.2E-3    -3 4 16 -17
54         4     -1.2E-3    -3 4 17 -19
c Outer poly 1st layer
60         1     -0.93      -2 3 10 -13
61         1     -0.93      -2 3 13 -15
62         1     -0.93      -2 3 15 -17 #103 #113 #123 #133
63         1     -0.93      -2 3 17 -19
64         1     -0.93      -2 4 19 -20
65         1     -0.93      -4 6 19 -20
66         1     -0.93      -6 19 -20
c Outer poly 2nd layer
70         1     -0.93      -1 2 10 -13
71         1     -0.93      -1 2 13 -15
```

```
72          1     -0.93       -1 2 15 -17 #101 #102 #111 #112
#121 #122 #131 #132
73          1     -0.93       -1 2 17 -19
74          1     -0.93       -1 2 19 -20
c PIN diode LiF tally cells
101         6     -2.635      -50 51 -91 90 -83 82
102         6     -2.635      -52 53 -91 90 -83 82
103         6     -2.635      -54 55 -91 90 -83 82
111         6     -2.635      -60 61 -91 90 -83 82
112         6     -2.635      -58 59 -91 90 -83 82
113         6     -2.635      -56 57 -91 90 -83 82
121         6     -2.635      -63 62 -91 90 -70 71
122         6     -2.635      -63 62 -91 90 -72 73
123         6     -2.635      -63 62 -91 90 -74 75
131         6     -2.635      -63 62 -91 90 -80 81
132         6     -2.635      -63 62 -91 90 -78 79
133         6     -2.635      -63 62 -91 90 -76 77
c Surronding void
200         0                 (-10:20:1) -100
c Universe
1000        0                 100


c ------------------ Surface Cards ------------------------
c Surfaces 1 - 20 AAND Construction
1           cy 10.5
2           cy 7
3           cy 3.8
4           cy 3.3
5           cy 3.2
6           cy 1.5
10          py 0
11          py 1.1
12          py 5.6
13          py 5.7
14          py 9
15          py 12
16          py 15
17          py 18
18          py 19.7
19          py 19.8
20          py 24.5
c Surfaces 50 - LiF tally cells
50          px 8.3
51          px 8.25
52          px 7.1
53          px 7.05
54          px 5.9
55          px 5.85
56          px -5.85
57          px -5.9
```

```
58          px -7.05
59          px -7.1
60          px -8.25
61          px -8.3
62          px -0.25
63          px 0.25
70          pz 8.3
71          pz 8.25
72          pz 7.1
73          pz 7.05
74          pz 5.9
75          pz 5.85
76          pz -5.85
77          pz -5.9
78          pz -7.05
79          pz -7.1
80          pz -8.25
81          pz -8.3
82          pz -0.25
83          pz 0.25
90          py 15.25
91          py 15.75
c Surfaces for void/source etc
100         sy 12.25 150

c ------------------ Data cards ---------------------------
c Importances
c
imp:n    16  2r                          $1-3
         16  r                           $4,5
         16                              $6
         16 5r                           $30-35
         8 6r                            $40-46
         4 4r                            $50-54
         4 6r                            $60-66
         2 4r                            $70-74
         4 4 8 4 4 8 4 4 8 4 4 8         $101-133
         1                               $200
         0                               $Universe
c Material Cards
c M1 Polyethylene M2 BF3 gas M3 Cadmium M4 Air M6 6LiF
c
m1          1001.60c    -0.14371
            6000.60c    -0.85629
mt1         poly.01t
m2          5010.60c    0.225
            5011.60c    0.025
            9019.60c    0.75
m3          48000.42c   1
m4          7014.60c    -0.78118
            8016.60c    -0.20953
```

```
         18000.42c  -0.00929
m5       5010.60c   1
m6       3006.60c   0.475
         3007.60c   0.025
         9019.60c   0.5
m7       3006.60c   1
c Source Cards
sdef     pos=0 15.5 100 erg=0.01 par=1
c
c Tally Cards
c F4 tally flux averaged over BF3 cell
c FM4 1.909E-5 atom barn.cm 10B
c
f4:n     2
fm4      1.909E-5 5 107
c F14-124 tally flux averaged over a cell LiF cells
c FM14 -124 6.015E-2 atom barn.cm 6Li
c
f14:n    101
fm14     6.015E-2 7 105
f24:n    102
fm24     6.015E-2 7 105
f34:n    103
fm34     6.015E-2 7 105
f44:n    111
fm44     6.015E-2 7 105
f54:n    112
fm54     6.015E-2 7 105
f64:n    113
fm64     6.015E-2 7 105
f74:n    121
fm74     6.015E-2 7 105
f84:n    122
fm84     6.015E-2 7 105
f94:n    123
fm94     6.015E-2 7 105
f104:n   131
fm104    6.015E-2 7 105
f114:n   132
fm114    6.015E-2 7 105
f124:n   133
fm124    6.015E-2 7 105
c Variance Reduction Cards
c
fc1:n    36j 1 11r 2j
c Control Cards
c
mode n
ctme 600
print
```